PRECISION ABSOLUTE FREQUENCY LASER SPECTROSCOPY OF ARGON II IN PARALLEL AND ANTIPARALLEL GEOMETRY USING A FREQUENCY COMB FOR CALIBRATION

A Dissertation

by

VLADIMIR LIOUBIMOV

Submitted to the Office of Graduate Studies of
Texas A&M University
in partial fulfillment of the requirements for the degree of

DOCTOR OF PHILOSOPHY

December 2008

Major Subject: Physics

PRECISION ABSOLUTE FREQUENCY LASER SPECTROSCOPY OF ARGON II IN PARALLEL AND ANTIPARALLEL GEOMETRY USING A FREQUENCY COMB FOR CALIBRATION

A Dissertation

by

VLADIMIR LIOUBIMOV

Submitted to the Office of Graduate Studies of
Texas A&M University
in partial fulfillment of the requirements for the degree of

DOCTOR OF PHILOSOPHY

Approved by:

Chair of Committee,	Hans A. Schuessler
Committee Members,	Teruki Kamon
	Dong Hee Son
	Lifan Wang
Head of Department,	Edward S. Fry

December 2008

Major Subject: Physics

ABSTRACT

Precision Absolute Frequency Laser Spectroscopy of
Argon II in Parallel and Antiparallel Geometry
Using a Frequency Comb for Calibration. (December 2008)
Vladimir Lioubimov, B.S., Moscow State Institute of Engineering and Physics;
M.S., Texas A&M University
Chair of Advisory Committee: Dr. Hans A. Schuessler

A collinear fast ion beam laser apparatus was constructed and tested. It will be used on-line to the SLOW RI radioactive beam facility in RIKEN (Japan) and as in the present experiment for precision absolute frequency measurements of astrophysically important reference lines. In the current work we conducted absolute measurements of spectral lines of Ar^+ ions using parallel and antiparallel geometries. To provide a reference for the laser wavelength iodine saturation spectroscopy was used. The precision of this reference was enhanced by simultaneously observing the beat node between the spectroscopy laser and the corresponding mode of a femtosecond laser frequency comb.

When performing collinear and anticollinear measurements simultaneously for the laser induced fluorescence, the exact relativistic formula for the transition frequency $\nu_0 = \sqrt{\nu_{coll} \cdot \nu_{anticoll}}$ can be applied. In this geometry ion source instabilities due to pressure and anode voltage fluctuation are minimized.

The procedure of fluorescence lineshapes fitting is discussed and the errors in the measurements are estimated. The result is $\nu_0 = 485,573,619.7 \pm 0.3$MHz corresponding to $\frac{\Delta\nu}{\nu} = 6 \times 10^{-10}$ and is an improvement of two orders of magnitude over the NIST published value.

To my parents and Anazawa Reiko, my wife, and to my daughter *Анастасия.*

ACKNOWLEDGMENTS

I would like to thank my advisor and committee chair, Dr. Hans A. Schuessler, for his enduring guidance through all stages of the research. Also Dr. Wada-san played a key role in making the collinear fast beam apparatus work. Without the active help of both of them the results of this dissertation would not have been obtained. All members of our experimental group at the Atomic Physics Laboratory at RIKEN (Japan): Dr. Takamine-san, Dr. Ishida-san, Dr. Nakamura-san, Dr. Okada-san, Dr. P. Schury, M. Ogawa-san made significant contributions to my work. Dr. Iimura-san from Japan Atomic Energy Research Institute (JAERI) was always available for discussions and suggestions concerning the development of this project. Also, Dr. Kolomenski at Texas A&M University was readily available for comments and help.

The Department of Physics at Texas A&M University has my thanks for the financial assistantship they provided over the past few years. I also acknowledge the Welch Foundation under the grant A-1546 for additional financial support of this project. I'm very thankful for R. M. M. Schuessler-Laux Fellowship for also providing financial support for my research. I'm especially thankful to the RIKEN Institution (Japan) for giving me opportunity to work for two years at the RIKEN facility and providing financial support.

I would also like to express my appreciation to all wonderful people with whom I was working in the Texas A&M Stored Ion Laboratory over the years. Jens Lassen, Vladimir Ryjkov, XianZhen Zhao, Dr. Xianghua Li, Serguei Jerebtsov, Feng Zhu, Milan Poudel, Ricardo Nava, Siying Peng.

Our research collaboration at TRIUMF, Vancouver, B.C. (Canada): F. Buchinger, J. E. Crawford, J. K. P. Lee, M. Pearson helped me to start with first ArII laser in-

duced fluorescence (LIF) test experiment. The laser beam was provided by Phil Levy in that experiment. I'm very thankful to all of them. Dr. H. Wollnik from II. Physicalisches Institut, Justus-Liebig-Universität (Germany) brought highlights to my understanding of the ion optics design for our ion focusing system at RIKEN.

The members of my Ph.D. committee, Prof. Teruki Kamon, Prof. Dong Hee Son, Prof. Lifan Wang have my thanks for all their time and help.

TABLE OF CONTENTS

CHAPTER Page

I INTRODUCTION 1

II COLLINEAR FAST BEAM TECHNIQUE 5

A. Relation between collinear and anticollinear measurements 5
B. Velocity bunching 8
C. Line broadening 12
1. Natural linewidth 12
2. Doppler broadening 12
3. Saturation broadening 16
4. Transit time broadening 16

III COLLINEAR FAST BEAM LASER SPECTROSCOPY APPARATUS 20

A. Ion source 20
1. Voltage supply of the ion source 23
B. Ion extraction and transport 25
1. Einzel lens 26
2. Ion optics 27
C. Acceleration voltage measurements and stability 31
1. High voltage measurements with power supply readout and voltage divider 31
D. Mass separation of ions 35
1. Dipole magnet 35
2. Mass separation of ions produced by the Danfysik 911A ion source 36
E. Fluorescence detection 38
1. Photomultiplier 38
2. PMT voltage divider 44
3. Condensor lens 44
4. Optical filters 46
5. The large solid angle elliptical mirror setup 50
F. Laser system 57
G. Frequency comb 58

CHAPTER Page

1. Optical frequency measurement 62
2. Almost simultaneous measurements of parallel and antiparallel laser excited radiation 63
H. Optical signal recording 68

IV EXPERIMENTAL DATA FOR AR II 72

A. Ar II level scheme 72
B. Sensitivity estimate 76
C. Data acquisition 79
D. Laser frequency scanning 79
1. Iodine calibration 79
a. Iodine absorption lines 79
b. Doppler-free absorption spectroscopy 80
2. Laser frequency measurements with frequency comb . 81
3. Line shape analysis and fitting procedure 88
a. Gauss model 88
b. Lorentz model 89
c. Voigt model 89
d. LogNormal model 89
e. Asymmetric functions: asymmetric Gauss, asymmetric Lorentz and Gaussian with exponential tails 100
4. Voltage drift, pressure drift and the necessity for simultaneous measurements in collinear and anticollinear geometry 103
5. Main results and discussion on the systematic error . 116

CHAPTER Page

V SUMMARY 121

REFERENCES 122

APPENDIX A 127

APPENDIX B 129

APPENDIX C 132

APPENDIX D 138

VITA 140

LIST OF TABLES

TABLE		Page
I	Summary of the line broadening contributions and comparison with the experiment.	19
II	Ion source operation parameters.	25
III	Calibration of the acceleration voltage parameters fitted by linear function Y=A+B*X in different voltage range.	33
IV	Laser background parameters.	56
V	RIKEN, TRIUMF, Texas A&M data parameters comparison.	56
VI	Efficiency calculation for elliptical mirror and condenser lens.	57
VII	The natural isotopic composition of Ar.	73
VIII	Ar II excitation lines.	74
IX	Ar II decay lines.	75
X	Comparison between eight fitting models.	105
XI	Change in anode voltage of the ion source operation parameters.	110
XII	Ar II $^2G_{7/2}$-$^2F^o_{5/2}$ transition frequency.	116
XIII	Condesor lens system parameters.	133
XIV	Determination of the different acceleration voltages used. The acceleration is the sum of high voltage applied to the ion source and the postacceleration voltage.	139

LIST OF FIGURES

FIGURE		Page
1	Schematic representation of the velocity spread reduction.	9
2	Transition probability of the excited state $^{40}Ar^{+}$ line 617.3986nm. .	17
3	Block diagram of the experimental setup.	21
4	Schematic drawing of the hollow-cathode Danfysik 911A ion-source.	22
5	Filament geometric properties and layout.	24
6	Voltage power supply scheme of ion source.	24
7	Einzel lens realized by symmetric arrangement of three plates with different potentials.	28
8	Einzel lens arrangements for the current experiment.	29
9	Ion beam trajectories through the quadrupole quartet, dipole magnet and quadrupole triplet.	31
10	Digital voltmeter output compared with voltage divider reading, 10 V range.	33
11	Digital voltmeter output compared with voltage divider reading, 1 V range.	34
12	Mass scan in linear (top) and logarithmic (bottom) scales.	38
13	Functional principle of a conventional photomultiplier tube. The schematical arrangement of the Burle 8850 is presented.	40
14	A photocathode spectral response curve of the Burle 8850 photo-multiplier.	42

FIGURE Page

15 A photocathode spectral response curve of the Hamamatsu R2256 photomultiplier. 43

16 Condenser lens system. 45

17 Blue filters. 46

18 Sharp cut filters. 47

19 Transmission curve of the B390 filter. 47

20 Transmission curve of the B440 filter. 48

21 Transmission curve of the Y44 filter. 49

22 Interference filter SPF-500 CVI Laser Co. 50

23 Solid angle subtended of by imagining optics. 51

24 Condenser lens, Edmund Optics 51 mm diameter. 53

25 The large solid angle elliptical mirror setup. 54

26 Vancouver's resonance signal with elliptical mirror setup. 55

27 Laser system for spectroscopy measurements. 59

28 Frequency comb. 60

29 The principle of the optical frequency synthesizer. The beat note between the frequency doubled mode and the mode at 2n yields the offset frequency. 64

30 Frequency comb locked to GPS signal. 64

31 Locking the frequency comb. 65

32 Gating scheme for the almost simultaneous measurements of parallel and antiparallel laser excited radiation. 66

33 Gating scheme for laser 1. 67

FIGURE Page

34 Gating scheme for laser 2. 68

35 Simultaneous measurements two beat frequencies by two different detectors. 69

36 Steady-state photon counting. 70

37 Ar II laser induced fluorescence (LIF) scheme. 74

38 Laser induced fluorescence (LIF) detection limit. 78

39 Simultaneous data recording for collinear (voltage channel A, fluorescence channel D) and anticollinear (voltage channel B, fluorescence channel C) measurements. 82

40 Calibration procedure to determine the n-th comb mode near the resonance from the iodine spectra. 83

41 An example of the beat fitting function model. 84

42 Origin C code for fitting function for beat frequency. 85

43 Fluorescence signal for collinear measurements with respect to the beat frequency. 86

44 Fitting beat frequency data in linear function model. 87

45 Gauss model. 90

46 Gauss model fit. 91

47 Gauss amplitude model. 92

48 Gauss amplitude model fit. 93

49 Lorentz model. 94

50 Lorentz model fit. 95

51 Voigt model. 96

52 Voigt model fit. 97

FIGURE Page

53 LogNormal model. 98

54 LogNormal model fit. 99

55 Asymmetric Gaussian model. 101

56 Asymmetric Gaussian model fit. 102

57 Gaussian with exponential tails model. 103

58 Gaussian with exponential tails model fit. 104

59 Asymmetric Lorentzian model. 105

60 Asymmetric Lorentzian model fit. 106

61 Fitting model comparison. 107

62 Acceleration voltage fluctuation during one single resonance scan. . . 108

63 Acceleration voltage fluctuation trend during longer times. 108

64 Circuit diagram of the feedback loop to compensate the acceleration voltage fluctuations. 109

65 Changes in anode voltage cause a change in the position of the resonance peak. 110

66 Operating the anode voltage in constant voltage mode. Collinear geometry scan. 111

67 Operating anode voltage in constant voltage mode. Anticollinear geometry scan. 112

68 Pressure drift in the ion source.100% pressure corresponds to the pressure at the beginning of the experiment. 113

69 Pressure drift in the ion source and the corresponding change in the peak of the resonance in collinear (blue) and anticollinear (red) geometries. 114

FIGURE Page

70 The frequency of the collinear resonance as a function of the pressure in the ion source. 115

71 The transition frequency of Ar II $^2G_{7/2}$-$^2F^o_{5/2}$, Voigt fit. 117

72 The transition frequency of Ar II $^2G_{7/2}$-$^2F^o_{5/2}$, Lorentz fit. 119

73 *Labview* code for acceleration voltage PID set. 127

74 *Labview* code for sPID. 128

75 Object and image of a thick lens. 134

76 Definition of the principal axes of the a lens. 134

CHAPTER I

INTRODUCTION

Collinear fast ion beam laser spectroscopy has developed into a powerful method to obtain nuclear data from optical measurements starting with the pioneering work of Kaufmann [1] in 1976. The advantages of the collinear fast beam technique is that it is Doppler-free, and that it introduces an artificial isotope shift, that can be used to advantage, to separate spectra from different isotopes, which overlap at zero acceleration voltage. The near reduction of the Doppler width in the collinear fast beam method is achieved by narrowing the velocity spread of the accelerated ions by velocity bunching. The artificial isotope shift has its root in the different velocities of the various isotopes after acceleration.

My research goal was to construct and test an apparatus to perform absolute frequency measurements of spectral lines with ultra high precision. Therefore exact calibration in the frequency/wavelength domain is a prerequisite. Such calibration is now possible by using the novel wavelength calibration system based on the femtosecond laser frequency comb (Nobel Prize 2006 to Professor T. Hänsch). We applied this technique to ArII, since as a test case an ArII beam was readily available in our laboratory. In addition and more important there has also been ongoing and increasing interest for absolute wavelength measurements with high precision in astrophysics. Some spectral lines of astrophysical interest have been compiled [2, 3, 4, 5, 6]. These lines are being used as a calibration markers in quasar atomic spectra. With the advent of large and extremely large telescope and superstable instruments, high-precision spectroscopy is becoming a reality. Several

---

The journal model is Physical Review Letters.

research interests have emerged during the last decade, such as the detection of planets around other stars, the measurements of possible variations in physical constants, the determination of element isotope ratios and the proposed direct measurements of the expansion of the Universe. All those experiments require very high precision in the measurements of spectral line frequencies and wavelengths. For example, a precision of the radial velocity of 1 cm/sec corresponds, on the focal plane of a spectrograph, to a shift of a few tenths of a nanometer, which compares to a typical molecular size [7]. Such a precision was recently obtained with a laser frequency comb [8].

Accelerated ion beams have also been used for test the relativistic time dilation for atomic ions (clocks) at different large velocities [9]. Precision high voltage determination by means of resonant collinear laser specproscopy was suggested by Poulsen [10] and tested by Knaak and Götte [11].

The second motivation for the present work is the near future application for my apparatus on-line to the RIKEN (Japan) nuclear facility, to observe suitably chosen spectral lines from short lived isotopes to obtain nuclear charge radii via isotope shift (IS) measurements, and so derive nuclear moments from the hyperfine structure splitting (HFS) of the spectra [12]. These nuclear physics experiments will be performed at the new slow RI-beam facility (SLOWRI) at RIKEN, Japan. The goal of laser spectroscopy in nuclear physics is the extraction of information on the properties of nuclear ground states such as nuclear spin I, the magnetic moment μ_I, the nuclear quadrupole moment Q_s, and the changes in the mean-square nuclear charge radius $\delta\langle r^2\rangle^{A,A'}$ between isotopes with mass number A and A'. The importance of those properties is attributed to the fact, that they can be deduced independently from a nuclear model and thus are an excellent test for nuclear theories and models. Optical spectroscopy methods with collinear fast beam

spectroscopy have been summarized in E.W. Otten's work [13] in 1989 and updated in publication of H.J. Kluge [14] in 2003. Laser techniques have been significantly improved over last 20 years, especially as far as wavelength coverage and detection efficiency are concerned. New techniques were developed such as neutral atom traps, laser ion sources, optical spectroscopy in an ion source itself [15], laser spectroscopy in a storage ring, accumulation, cooling and bunching of radioactive beams in ion traps [16]. Other spectroscopic methods were diversified and improved in sensibility and selectivity and in this work also in precision, such methods are collinear fast beam laser, and resonance ionization spectroscopy. A particular application of resonance ionization, namely step-wise excitation field-ionization was described in detail by Jens Lassen [17] and Xinghua Li [18] and was conducted in our laboratory at Texas A&M.

In the present thesis the $^{40}Ar^{+}$, $^{2}G_{7/2}$- $^{2}F_{5/2}$ transition [19] was used for an ultra-high precision measurements on collinear and anticollinear accelerated ion beams. Application of a frequency comb for the precise comparison of the frequency of the laser with the markers of the comb for collinear and anticollinear geometry was the novel crucial step to achieve ultra high precision. The experimental setup for the beam apparatus consists of a hollow cathode ion source producing Ar^{+} ions, and ion optics to collimate and manipulate the ion beam. A dipole magnet is employed for ion mass separation. The laser system consisted of two dye lasers pumped by solid state lasers. A fiber femtosecond laser with a repetition rate of 250MHz (Menlo System) produced the frequency comb. Both the repetition rate and the carrier offset frequency were locked to GPS (global positioning system). A short fluorescence region was implemented between the metal cage for post accelerating/decelerating the ions to bring them into resonance by Doppler tuning. For observing the fluorescent light at resonance either a spherical mirror and condenser lenses system or a large solid

angle elliptical mirror setup were employed. A set of optical filters helped to reduce the laser stray light. A photomultiplier tube detected the fluorescence signal.

A line shape analysis and a curve fitting procedure of the obtained data were conducted and an error analysis is provided.

CHAPTER II

COLLINEAR FAST BEAM TECHNIQUE

The aim of spectroscopy is to study experimentally the energy-level structure of atomic and molecular systems. The method of the atomic laser spectroscopy investigates the response of the atoms to tunable narrow band radiation. The resolving power of the method is limited only by homogeneous and inhomogeneous line broadenings. In atomic or ion beams the Doppler broadening can be significantly reduced.

A. Relation between collinear and anticollinear measurements

The absolute unshifted atomic line frequency can be obtained by observation of the positive and negative Doppler shifted signal in collinear and anticolinear geometry respectively. The relation between these measured frequencies will be discussed in the following.

In plain wave approximation [20] the electromagnetic field $\Phi(\vec{r},t)$ can be described as a function of coordinate the $\vec{r}$ and time t:

$$\Phi(\vec{r},t) = Ae^{-i(\omega t - \vec{k}\cdot\vec{r})}. \tag{2.1}$$

Here A is an amplitude of plane wave, ω is the frequency, the wave vector $\vec{k}$ has a magnitude of $|\vec{k}| = \omega/c = 2\pi/\lambda$ and its direction is along the propagation of the wave. Considering the phase argument of the plain wave, it can be shown to be invariant under the Lorentz transformations [21]. The phase can be described as a 4-vector $k^{\mu} = (\vec{\omega}/c, \vec{k})$:

$$-\vec{k}\cdot\vec{r} + \omega t = \frac{\omega}{c}(c\,t) - \vec{k}\cdot\vec{r} = \frac{\omega}{c}x^0 - \vec{k}\cdot\vec{r}. \tag{2.2}$$

For this 4-vector one can apply the Lorentz transformation rule from special relativity. For an any vector $\vec{a}$ with coordinate components $a^0,\ a^1,\ a^2,\ a^3$ these components will transform as

$$a^0 = \frac{a^{0\prime} + \frac{v}{c}a^{1\prime}}{\sqrt{1 - v^2/c^2}},\ a^1 = \frac{a^{1\prime} + \frac{v}{c}a^{0\prime}}{\sqrt{1 - v^2/c^2}},\ a^2 = a^{2\prime},\ a^3 = a^{3\prime}. \tag{2.3}$$

For simplicity introduce the notation:

$$\beta = \frac{v}{c}, \tag{2.4}$$

then

$$a^0 = \frac{a^{0\prime} + \beta a^{1\prime}}{\sqrt{1 - \beta^2}},\ a^1 = \frac{a^{1\prime} + \beta a^{0\prime}}{\sqrt{1 - \beta^2}},\ a^2 = a^{2\prime},\ a^3 = a^{3\prime}. \tag{2.5}$$

For the inverse transformation one needs to change v to $-v$

$$a^{0\prime} = \frac{a^0 - \beta a^1}{\sqrt{1 - \beta^2}},\ a^{1\prime} = \frac{a^1 - \beta a^0}{\sqrt{1 - \beta^2}},\ a^{2\prime} = a^2,\ a^{3\prime} = a^3. \tag{2.6}$$

Thus for

$$k^{0\prime} = \frac{k^0 - \beta k^1}{\sqrt{1 - \beta^2}}, \tag{2.7}$$

where primed coordinates are related with the moving frame , and non-primed coordinates refer to the rest frame. The X and X' coordinates coincide, and Z' and Y' are parallel to Z and Y. Considering that $k^0 = \omega/c$, and $k^1 = k_x = (\omega/c)\cos\theta$, where θ is angle between axis X and direction of propagation of the wave, $\beta = v/c$ where v- velocity of the moving frame K' relative to fixed frame K, one can find:

$$\omega' = \frac{\omega(1 - \frac{v}{c}\cos\theta)}{\sqrt{1 - \frac{v^2}{c^2}}}. \tag{2.8}$$

For $\theta = 0$ we obtain the longitudinal Doppler effect:

$$\omega' = \frac{\omega(1 - \frac{v}{c})}{\sqrt{1 - \frac{v^2}{c^2}}} = \omega\frac{\sqrt{1 - \frac{v}{c}}}{\sqrt{1 + \frac{v}{c}}}, \tag{2.9}$$

for $\theta = \pi/2$ we observe the transversal Doppler effect:

$$\omega' = \frac{\omega}{\sqrt{1-\frac{v^2}{c^2}}}. \tag{2.10}$$

In the next step we consider how the ion *sees* the electromagnetic wave from the laser for collinear and anticollinear geometry. In the moving frame (*primed*), the ion is at rest and we denote its frequency transition as ω_0. Then

$$\omega_0 = \omega' = \omega^+ \frac{\sqrt{1-\frac{v}{c}}}{\sqrt{1+\frac{v}{c}}}, \tag{2.11}$$

and

$$\omega_0 = \omega' = \frac{\omega^-(1+\frac{v}{c})}{\sqrt{1-\frac{v^2}{c^2}}} = \omega^- \frac{\sqrt{1+\frac{v}{c}}}{\sqrt{1-\frac{v}{c}}}, \tag{2.12}$$

where the plus sign indicates $\cos\theta = +1$ (ion beam collinear (parallel) with laser light propagation, laser frequency $=\omega^+$), while the minus sign was taken for $\cos\theta = -1$ (ion beam anticollinear (antiparallel) with laser light propagation, laser frequency$=\omega^-$). Expressing ω^+ and ω^- as:

$$\omega^+ = \omega_0 \frac{\sqrt{1-\beta}}{\sqrt{1+\beta}}, \tag{2.13}$$

and

$$\omega^- = \omega_0 \frac{\sqrt{1+\beta}}{\sqrt{1-\beta}}, \tag{2.14}$$

it follows:

$$\omega^+\omega^- = \omega_0 \frac{\sqrt{1-\beta}}{\sqrt{1+\beta}} \cdot \omega_0 \frac{\sqrt{1+\beta}}{\sqrt{1-\beta}} = \omega_0^2 \tag{2.15}$$

or

$$\boxed{\omega_0 = \sqrt{\omega^+\omega^-}.} \tag{2.16}$$

This basic formula is an exact relativistic formula for obtaining the absolute frequency of an atomic transition ω_0 from the simultaneously measured collinear ω^+ and anticollinear ω^- laser frequencies. This advantage of simultaneous collinear

and anticollinear measurements was originally shown in the work by Borghs and Silverans [22].

B. Velocity bunching

The effect named *velocity bunching* was introduced by Kaufmann in 1976 [1] and is due to a *kinematic compression,* which occurs during the ion acceleration. Since the electrostatic forces are conservative, the sum of potential energy and kinetic energy remains constant. Thus the potential energy of electrostatic field converts directly into the kinetic energy of the individual ions, keeping the energy distribution of the ions untouched. The kinetic energy of an ion is:

$$E_k = \frac{1}{2}mv^2, \tag{2.17}$$

where m is the mass of the ion and v is the velocity of the ion. By differentiating it follows:

$$\mathrm{d}E_k = mv\,\mathrm{d}v, \tag{2.18}$$

and since $\mathrm{d}E_k = \mathrm{const}$,

$$mv\,\mathrm{d}v = \mathrm{const} \tag{2.19}$$

or

$$\mathrm{d}v = \frac{1}{mv}\,\mathrm{d}E_k \sim \frac{1}{v}, \tag{2.20}$$

from which follows, that the velocity spread $\mathrm{d}v$ that gives rise to the Doppler broadening is inversely proportional to the ion velocity v, meaning an increase in ion velocity will result in the decrease of the velocity spread. A simple explanation of the bunching effect is that ions having a large initial velocity spend less time in the accelerating field and thus gain less velocity than the initially slow ions. The schematic example of velocity spread reduction is shown in Fig. 1. For given

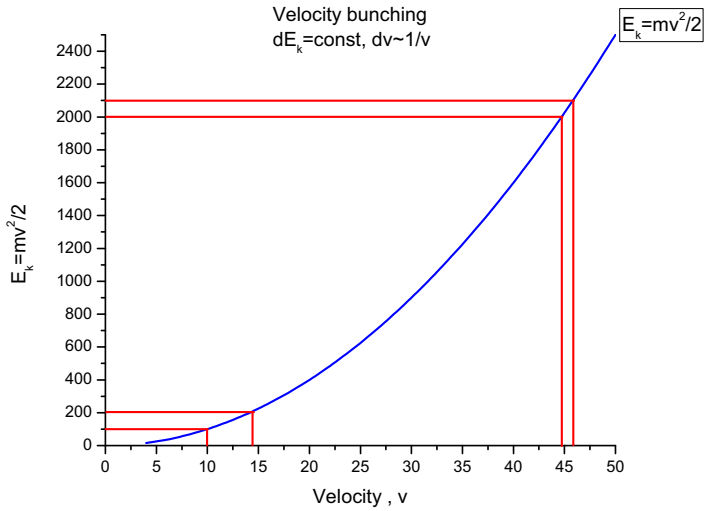

FIG. 1. Schematic representation of the velocity spread reduction.

dE_k=100, velocity spread noticeably reduced from about 5 to about 1.

The velocity distribution function $f(\vec{v})$ describes the number of ions n in a given velocity interval:

$$\mathrm{d}n = f(\vec{v})\mathrm{d}\vec{v} = f(v_x, v_y, v_z)\mathrm{d}v_x\mathrm{d}v_y\mathrm{d}v_z. \tag{2.21}$$

For the plasma in the ion source, the ion velocity distribution function is assumed to be near Maxwellian [23]:

$$f(v_x, v_y, v_z) = n\left(\frac{m}{2\pi kT}\right)^{\frac{3}{2}} e^{-\frac{m(v_x^2+v_y^2+v_z^2)}{2kT}}. \tag{2.22}$$

The 3-dimensional Maxwellian velocity distribution function is a product of three independent 1-dimensional velocity distribution functions, each having form:

$$f(v_x) = n\left(\frac{m}{2\pi kT}\right)^{\frac{1}{2}} e^{-\frac{mv_x^2}{2kT}}. \tag{2.23}$$

From the ion velocity distribution function Eq. 2.22 the distribution function for the

energy $f(E)$ and the speed $F(v)$ can be obtained:

$$F(v) = 4\pi v^2 f(v) = 4\pi v^2 n \left(\frac{m}{2\pi kT}\right)^{\frac{3}{2}} e^{-\frac{mv^2}{2kT}}, \tag{2.24}$$

and

$$f(E) = F(v)\frac{\mathrm{d}v}{\mathrm{d}E} = n\left(\frac{4}{\pi}\right)^{\frac{1}{2}} E^{\frac{1}{2}} e^{-\frac{E}{kT}}, \tag{2.25}$$

from which the mean energy then follows as:

$$\bar{E} = \frac{3}{2}kT. \tag{2.26}$$

In an isotropic plasma the kinetic energy is divided equally between the three degrees of freedom:

$$\bar{E}_x = \bar{E}_y = \bar{E}_z = \frac{1}{2}kT. \tag{2.27}$$

The most probable ion speed v_0, for which distribution function F(v) is at the maximum [24] is given as:

$$\boxed{v_0 = \sqrt{\frac{2kT}{m}}.} \tag{2.28}$$

Next, consider two ions of identical mass m, having velocity components in the z-direction of $v_{01} = 0$ for one and the most probable $v_{02} = \sqrt{2kT/m}$ for the other. The difference between them, or velocity spread, is:

$$\Delta v_0 = v_{02} - v_{01} = \sqrt{2kT/m} - 0 = \sqrt{2kT/m}. \tag{2.29}$$

If both ions are accelerated in the z-direction through a potential difference ΔU, the final velocities will be $v_{a1} = \sqrt{2e\Delta U/m}$ and $v_{a2} = \sqrt{2kT/m + 2e\Delta U/m}$ with the

velocity difference:

$$\Delta v_a = v_{a2} - v_{a1} = \sqrt{\frac{2kT}{m} + \frac{2e\Delta U}{m}} - \sqrt{\frac{2e\Delta U}{m}} = \tag{2.30}$$

$$= \sqrt{\frac{2e\Delta U}{m}} \sqrt{\left(1 + \frac{m}{2e\Delta U}\frac{2kT}{m}\right)} - \sqrt{2e\Delta U/m} \approx \tag{2.31}$$

$$\approx \sqrt{\frac{2e\Delta U}{m}} + \sqrt{\frac{2e\Delta U}{m}} \cdot \frac{1}{2}\frac{kT}{e\Delta U} - \sqrt{\frac{2e\Delta U}{m}} = \tag{2.32}$$

$$= \sqrt{\frac{2e\Delta U}{m}} \cdot \frac{1}{2}\frac{kT}{e\Delta U} = \frac{1}{2}\sqrt{\frac{2kT}{m}} \cdot \sqrt{\frac{kT}{e\Delta U}}. \tag{2.33}$$

The reduction factor R is thus the reduction of the velocity spread due to acceleration:

$$R = \frac{\Delta v_a}{\Delta v_0} = \frac{1}{2}\sqrt{\frac{2kT}{m}} \cdot \sqrt{\frac{kT}{e\Delta U}} \cdot \sqrt{\frac{m}{2kT}} = \frac{1}{2}\sqrt{\frac{kT}{e\Delta U}}, \tag{2.34}$$

$$\boxed{R = \frac{1}{2}\sqrt{\frac{kT}{e\Delta U}}.} \tag{2.35}$$

Thus the residual Doppler linewidth due to a thermal energy spread of ions extracted from ion source $\Delta\omega_D$ is reduced by a factor proportional to the square root of the ratio of kT to the acceleration voltage ΔU:

$$\Delta\nu_{D\_CFBS} = \frac{1}{2}\sqrt{\frac{kT}{e\Delta U}} \cdot \Delta\nu_D. \tag{2.36}$$

Considering $\Delta U = U_{acc} = 20\text{kV}$, T=1700K,

$$R = \frac{1}{2}\sqrt{\frac{1.38 * 10^{-23} \times 1700}{1.6 * 10^{-19} \times 20000}} = 1.35 \times 10^{-3}. \tag{2.37}$$

In general the acceleration voltage is choosen such that the reduction factor is large enough to reduce the signal linewidth to the natural linewidth. Applied to the present case, it follows:

$$\Delta\nu_{D\_CFBS} = 2.3\text{GHz} \times 1.35 \times 10^{-3} = 3.1\text{MHz} \quad \text{for T} = 1700\text{K}. \tag{2.38}$$

C. Line broadening

1. Natural linewidth

If an ion is excited by absorption of a photon of laser light, it can release its excitation energy in the form of spontaneous emission. This process is called *fluorescence.* The probability per second for fluorescence per ion is given by the Einstein coefficient A_{ki}, where i denotes the initial energy state of ion before transition, and k indicates the final one, after the transition has occurred. In the description of the excited electron by the classical model of a damped harmonic oscillator a Lorentzian line profile as the Fourier transform of a damped oscillation can be deduced [25]. The natural linewidth of a transition from energy level i to energy level k can be obtained also from the Heisenberg's uncertainty relation: if energy state has a lifetime τ, it's energy can be determined within the uncertainty $\Delta E = \hbar/\tau = \hbar\Delta\omega_{natural}$:

$$\Delta\omega_{natutal} = A_{ik}, \tag{2.39}$$

$$\boxed{\Delta\nu_{natutal} = \frac{A_{ik}}{2\pi}.} \tag{2.40}$$

For the $^2\mathrm{G}_{9/2}$ - $^2\mathrm{F}^o_{7/2}$ transition, NIST data [26] gives $A_{ki} = 2 \times 10^7 \mathrm{sec}^{-1}$ or

$$\Delta\nu_{natutal} = \frac{A_{ik}}{2\pi} = \frac{2 \times 10^7}{2\pi} = 3.18 \text{ MHz}. \tag{2.41}$$

2. Doppler broadening

If an ion is moving, the frequency of radiation of the emitted photon, in the laboratory frame, is different from the one of a resting atom. The laws of conversation of energy and momentum tell us:

$$E_2 + \frac{mv_2^2}{2} = E_1 + \frac{mv_1^2}{2} + \hbar\omega, \tag{2.42}$$

$$m\vec{v}_2 = m\vec{v}_1 + \hbar\vec{k}, \tag{2.43}$$

where E_2 - energy of the excited level of the ion; E_1 - energy of the lower state of the ion; m - mass of the ion; $\vec{v}_2$ - velocity of the ion after emission photon, $\vec{v}_1$ - velocity of the ion before emission photon; $\hbar\omega$ and $\hbar\vec{k}$- energy and momentum of emitted photon. Let ω_0 be the frequency of the emitted photon if the ion was at rest, then:

$$\hbar\omega_0 = E_2 - E_1. \tag{2.44}$$

Taking the square of the Eq. (2.43) and excluding from Eq. (2.42)-(2.43) E_1, E_2, v_1, one obtains the equation:

$$\hbar(\omega_0 - \omega) = \frac{\hbar^2 k^2}{2m} - \hbar\vec{v}_2 \cdot \vec{k}. \tag{2.45}$$

Next, we introduce the axis z along the wave vector k of the emitted photon and taking into account that $k = \omega/c$ we re-write equation (2.45) as:

$$\omega_0 - \omega = \frac{\hbar\omega^2}{2mc^2} - \frac{\omega v_{2z}}{c}. \tag{2.46}$$

At room temperature $v_{2z}/c \approx 10^{-5}$, while for $\omega \approx 10^{15}$ and $k\omega^2/(2mc^2) \approx 10^{-9}$, thus the first term in can be neglected compared with the second term:

$$\omega = \frac{\omega_0}{1 - v_{2z}/c} \approx \omega_0(1 + \frac{v_{2z}}{c}). \tag{2.47}$$

The number of ions with velocities between v_{2z} and $v_{2z} + dv_{2z}$ according to the Maxwell distribution is proportional to:

$$dv_{2z}\ e^{-\frac{mv_2^2}{2kT}}, \tag{2.48}$$

where k is Boltzman constant. From Eq. (2.47) we have:

$$v_{2z} = \frac{(\omega - \omega_0)c}{\omega_0}, \tag{2.49}$$

$$dv_{2z} = \frac{c}{\omega_0} d\omega. \tag{2.50}$$

Then from Eq. (2.48), we get energy distribution in a frequency domain:

$$w(\omega)d\omega \approx e^{-\frac{Mc^2(\omega-\omega_0)^2}{2\omega_0^2 kT}} d\omega. \tag{2.51}$$

This is a Gaussian distribution of the emission line with a maximum at the frequency $\omega = \omega_0$. The width of the Gaussian profile $\Delta\omega$ in the frequency range corresponds to half of the maximum intensity. One can find those frequencies ω_1 and ω_2 as the root of the equation:

$$\frac{1}{2} = e^{-\frac{mc^2(\omega-\omega_0)^2}{2\omega_0^2 kT}}, \tag{2.52}$$

from that it follows:

$$\Delta\omega_D = 2\omega_0 \sqrt{\frac{2kTln2}{mc^2}}. \tag{2.53}$$

In a more practical form using frequency units, where M is the mass of the ion in atomic mass units, and T is temperature inside the ion source in Kelvin:

$$\boxed{\Delta\nu_D = 7.16 \times 10^{-7} \nu_0 \sqrt{\frac{T}{M}} \text{ [Hz].}} \tag{2.54}$$

For a temperature $T = 1700$K, inside of our operating ion source [27], and $\lambda_0 = 611.66$nm, one can obtain:

$$\Delta\nu_D = 7.16 \times 10^{-7} \frac{3 \times 10^8}{611.66 \times 10^{-9}} \sqrt{\frac{1700}{40}} = 2.3 \text{ GHz.} \tag{2.55}$$

The corresponding velocity distribution in the direction perpendicular to the beam axis is truncated by collimating the beam, in this case the Doppler width reduces from the value $\Delta\nu_D$ by the factor of $\sin\theta$, where θ is angular divergence of the beam:

$$\boxed{\Delta\nu_{D\perp} = \Delta\nu_D \sin\theta.} \tag{2.56}$$

In our case, $\theta = 10 \times 10^{-3}$ rad, $\sin\theta \approx 0.01$, it follows:

$$\Delta\nu_{D\perp} = 2.3\text{GHz} \times 0.01 = 23\text{MHz} \quad \text{for T} = 1700\text{K}. \tag{2.57}$$

The ion in the beam *sees* the frequency of the laser light with a shifted component due to Doppler effect. If the atom moves with the laser beam in the same direction, then for the atom to absorb the laser light, the resonance frequency should be shifted by:

$$\nu_D = -\nu_0 \frac{v}{c}. \tag{2.58}$$

The sign minus indicates that in the rest frame of ion the laser source is moving away from the ion. Next, consider the contribution of the non-parallel component of the velocity of the ion to the laser radiation. The frequency shift $\Delta\nu$ is due to the fact that the component parallel to the laser beam is changing due to the divergence of the beam. The change in velocity due to divergence of the beam is:

$$\Delta v_z = v_z - v_z \cos\theta = v_z(1 - \cos\theta). \tag{2.59}$$

Then the frequency shift due to divergence of the beam:

$$\Delta\nu_{D\parallel} = -\nu_0 \frac{\Delta v_z}{c}, \tag{2.60}$$

$$\boxed{\Delta\nu_{D\parallel} = \nu_0 \frac{v_z(1 - \cos\theta)}{c},} \tag{2.61}$$

with $\nu_0 \approx 4.9 \times 10^{14}$Hz, $v_z \approx 3.1 \times 10^5$ m/s, divergence $\theta = 10$mrad, and $c \approx 3 \times 10^8$m/s, one obtains:

$$\Delta\nu_{D\parallel} = 4.9 \times 10^{14} \times \frac{3.1 \times 10^5 \times (1 - \cos(0.010))}{3 \times 10^8} = 25\text{MHz}. \tag{2.62}$$

3. Saturation broadening

By definition the saturation parameter S_0 is:

$$S_0 = \frac{excitation\ rate}{relaxation\ rate}. \tag{2.63}$$

Since the excitation rate is $B_{21} \cdot \rho$, and the relaxation rate A_{21}, where $I = \rho \cdot c$, I intensity of the laser beam, c speed of light, A_{21}, B_{21} Einstein's coefficients, it follows:

$$S_0 = \frac{B_{21} \cdot \rho}{A_{21}} = \frac{I \cdot B_{21}}{cA_{21}}. \tag{2.64}$$

The relation of the Einstein coefficients is given by formula [28]:

$$\frac{A_{21}}{B_{21}} = \frac{8\pi h\nu_0^3}{c^3}, \tag{2.65}$$

and thus:

$$S_0 = \frac{I}{c}\frac{c^3}{8\pi h\nu_0^3} = \frac{Ic^2}{8\pi h\nu_0^3}. \tag{2.66}$$

It can be seen that the saturation broadening causes a Lorentzian profile with the increased halfwidth [29]:

$$\gamma_s = \gamma\sqrt{1 + S_0}, \tag{2.67}$$

where $\gamma = \frac{A_{21}}{2\pi}$ is natural linewidth. In our case with $\gamma = 3.1$MHz, the laser intensity I=0.43mW. With these parameters one obtains for the saturation parameter $S_0 = 20.28$ and for saturation broadening $\gamma_s = 14.3$MHz.

4. Transit time broadening

Since the interaction time with the laser in fluorescence chamber is limited by the time of flight of the ions through the fluorescence region, one needs to also evaluate transit time broadening. An ion *sees* the radiation with effective duration an l/v, where l is a length of the interaction region, determined by solving rate equations [30],

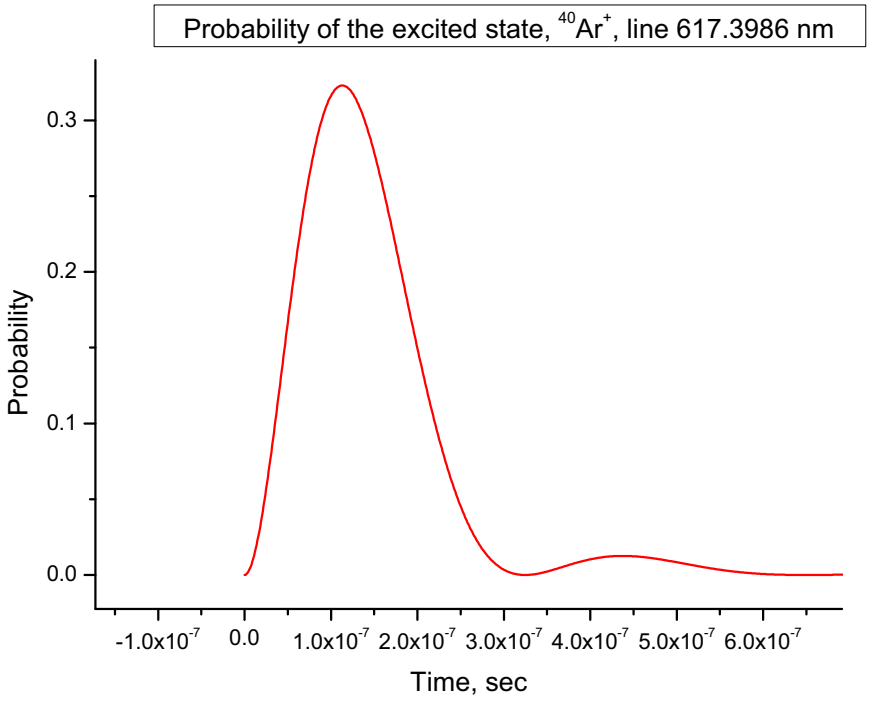

FIG. 2. Transition probability of the excited state $^{40}Ar^{+}$ line 617.3986nm.

and v is the velocity of ion. The example of the solution of the rate equations for one of our test lines (617.3986nm) of $^{40}Ar^{+}$ is presented in Fig. 2.

The radiation spectrum is broadened according to the uncertainty condition:

$$\Delta\nu\Delta t \approx 1. \tag{2.68}$$

Therefore

$$\Delta\nu_{transit} \approx \frac{v}{l}. \tag{2.69}$$

For $v = 3.1 \times 10^5$ m/s and $l = 0.04$ m we have:

$$\Delta\nu_{transit} \approx 7.8\text{MHz}. \tag{2.70}$$

A more detailed treatment [31], however yields:

$$\Delta\nu_{transit} = \frac{0.89}{\Delta t}, \tag{2.71}$$

where $\Delta t = \frac{l}{v} = 1.3 \cdot 10^{-7}$s gives:

$$\Delta\nu_{transit} = 6.8\text{MHz}. \tag{2.72}$$

The later value can be obtained as following. Consider an undamped oscillator $x = x_0 \cos\omega_0 t$, which oscillates with constant amplitude during the time interval T and which then suddenly stops oscillating. It's frequency spectrum is obtained from the Fourier transformation according to:

$$A(\omega) = \frac{1}{\sqrt{2\pi}} \int_0^T x_0 \cos(\omega_0 t) e^{-i\omega t} dt. \tag{2.73}$$

The spectral intensity profile $I(\omega) = A^* A$ is, for $(\omega - \omega_0) << \omega_0$. equal to:

$$I(\omega) = C \frac{\sin^2[(\omega - \omega_0)T/2]}{(\omega - \omega_0)^2}. \tag{2.74}$$

This function has a full half width $\Delta\nu_{transit} = \frac{0.89}{T}$ of its central maximum.

TABLE I. Summary of the line broadening contributions and comparison with the experiment.

Broadening mechanism	**Linewidth, [MHz]**
Natural	3.18
Doppler after velocity bunching	3.1
Beam divergence Doppler $\perp$	23
Beam divergence Doppler $\parallel$	25
Saturation	14.3
Transit time	6.8
	Total
	75.38 MHz
Experimental data	
102 MHz	

CHAPTER III

COLLINEAR FAST BEAM LASER SPECTROSCOPY APPARATUS

The block diagram of the experimental setup is shown in Fig. 3. The apparatus consists of three major parts: the vacuum system containing the ion source, ion optics and dipole magnet for mass separation, and the laser and optical detection system. The functioning of the ion source, the ion optics, the dipole magnet, the photomultiplier, the data acquisition system, the laser scanning voltages and the high voltage power supply for acceleration of the ions are controlled by a computer with software written in *Labview*. Examples of *Labview* programs to control the acceleration voltage feedback loop are given in Appendix A.

A. Ion source

In the present experiments a hollow cathode ion source similar to the Sidenius type [32] was used (Fig. 4).

The ionization efficiency measured by Sidenius [33] was reported as high as 40% for Ar. This type of ion source utilizes a discharge to ignite ionization. The operational parts of ion source are:

- the oven system with gas transport tube
- the discharge chamber
- the filament

The main advantage of a Sidenius type ion source is, that it has small geometrical dimensions, such that a minimal volume can be achieved. Such a construction reduces the hold-up time in the ion source, as well as makes it possible to heat the source

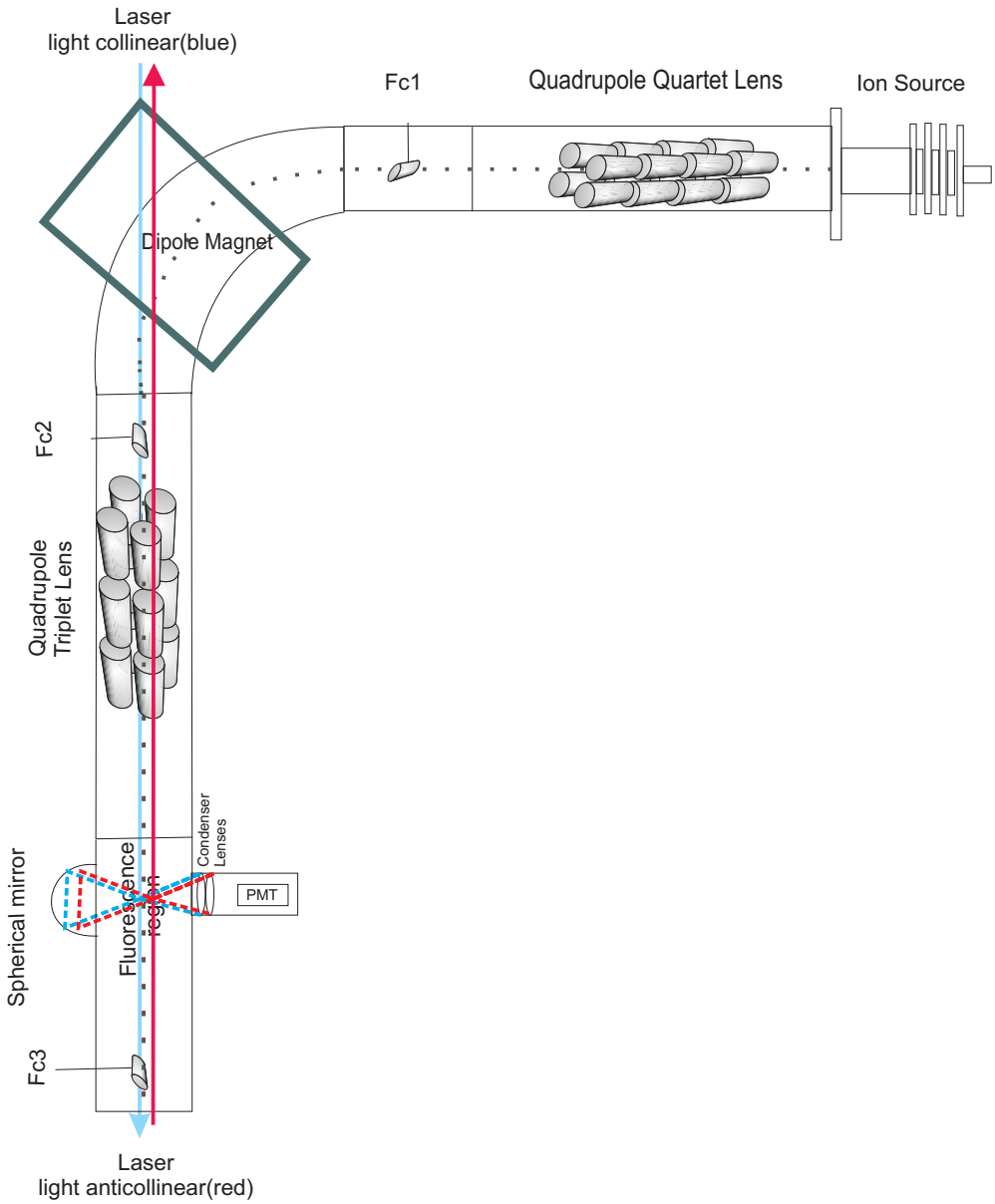

FIG. 3. Block diagram of the experimental setup.

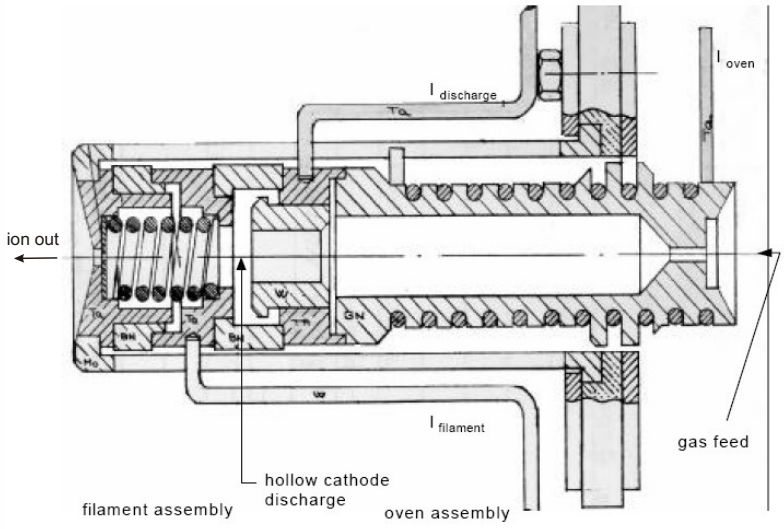

FIG. 4. Schematic drawing of the hollow-cathode Danfysik 911A ion-source.

to a high temperature with low power input. The geometry results in high current density and stable beam formation, yielding in this way optimum resolving power. The plasma arc forms around the outlet penetrated by the electric extraction field. The materials used in ion source are:

- Molybdenum is the cheapest refractory metal and may be used up to 2000^0 C. It is relatively easy to machine and has a low affinity for reactive gases.
- Tantalum is particulary easy to machine, and it can be used up to 2600^0 C.
- Tungsten is the most frequently used filament material, since it can be operated at temperatures above 3000^0 C. However it is so refractory that machining is extremely difficult. It also embrittles due to crystallization.
- Boron nitride is an isolating material, that can be precisely machined, is not particularly brittle, and can be used over a wide temperature range. The

disadvantage of boron nitride is that it picks up moisture, and when it is subsequently outgassed rapidly at high temperatures in vacuum, the surface decomposes. It is recommended that components made of boron nitride always be stored in completely dry places, and if necessary, pre-heated at atmospheric pressure and then carefully outgassed under vacuum.

The Danfysik 911A ion source is a discontinued product, a spare filament for repair has to be home built in local machine shop. The procedure of making filament was the following. The drill rod was used as a base, around which the copper wire with the certain step (see Fig. 5 for filament geometry and layout) was wound, and then, the tungsten rod was bent between the copper wire. After the desired length of the filament was achieved, the copper wire was removed, the tungsten wire was cut, and the end of the filament was ground to the flat surfaces. The latter step was crucial to provide good electrical and mechanical contact between filament and ion source cathode caps.

1. Voltage supply of the ion source

The ion source is connected to the positive high voltage, so that the positive ions are accelerated towards the beam line output which is at common ground. Since the ion source power supplies are operating at a high potential, they need to be isolated from the common ground through an isolation transformer. The schematic diagram of ion source power connections is presented in Fig. 6.

The typical ion source operation parameters are presented in Table II. Detailed procedure on operating the Danfysik 911A ion source is described in manufacturer's manual [34].

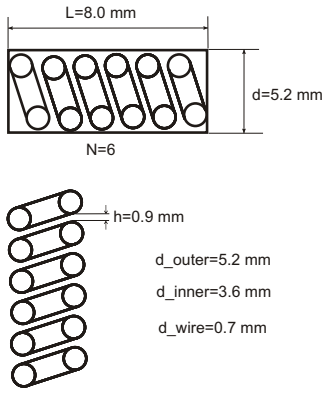

FIG. 5. Filament geometric properties and layout.

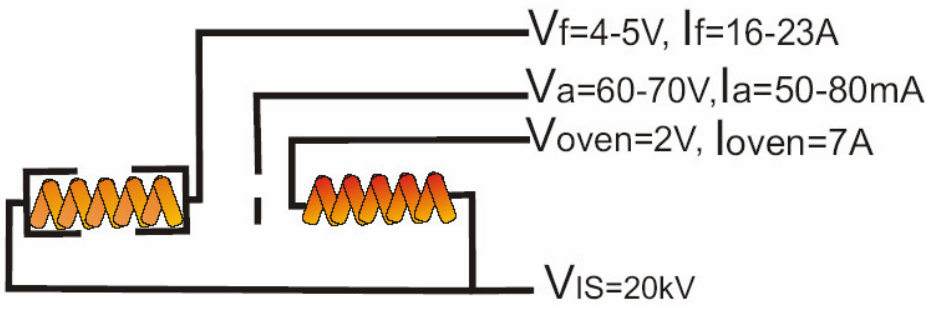

FIG. 6. Voltage power supply scheme of ion source.

TABLE II. Ion source operation parameters.

Vacuum	**Filament**		**Anode**		**Beam**
Ion source	I	R	I	V	I
$mbar$	A	$m\Omega$	mA	V	μA
2×10^{-5}	16-23	160-240	50-80	60-70	1.0-1.2

B. Ion extraction and transport

The ions are extracted from the plasma of a gas discharge, and the accelerated beam passes through a hole in the extraction electrode into the Einzel lens. The emitting plasma surface area has a concave shape, called meniscus, which depends on the plasma density and the strength of the accelerating electric field at the plasma surface. The concave shape of the meniscus and the aperture in the ion source electrode produce a transverse electric field component, that results in a converging beam. The extraction and focusing are strongly influenced by the geometry of the electrode system and the plasma parameters inside the ion source, as well as the beam space charge, which can disturb the electrostatic field of the extracting lens in the case, when the extraction current density exceeds a few mA/cm^2. Such a large space charge will result in increasing the divergence of the ion beam. The simplest model of ion extraction is based on the Poisson equation for two flat electrodes with a bias voltage V between them. Solving the Poisson equation yields the Langmuir-Child formula of the ion current I as a function of applied voltage V [35, 36]:

$$I = \left(\frac{4\varepsilon}{9}\right)\left(\frac{2e}{m}\right)^{1/2}\frac{s}{d^2}V^{3/2}, \tag{3.1}$$

where ε is the dielectric constant, d is the distance between electrodes, s is the surface area that emits ions of mass m. The formula can be re-written in the form:

$$I = PV^{3/2}, \tag{3.2}$$

where P is the perveance coefficient. Approximating the extraction geometry of the 911A ion source in this parallel plate model with

$$s = \pi \times (R_{outer}^2 - r_{inner}^2) = \pi \times (5^2 - 3.6^2) mm^2, \tag{3.3}$$

and d=2mm yields a perveance:

$$P = \frac{4 \times 8.85 \times 10^{-12}}{9} \sqrt{\frac{2 \times 1.6 \times 10^{-19}}{40 \times 1.66 \times 10^{-27}}} \frac{\pi \times (5^2 - 3.6^2) \times 10^{-6}}{2^2 \times 10^{-6}} = \tag{3.4}$$

$$= 8.2 \times 10^{-8} [\frac{\mathrm{A}}{\mathrm{Volt}^{3/2}}]. \tag{3.5}$$

According to the Eq. 3.1 the extracted ion beam current in this simple model equals:

$$I = 8.2 \times 10^{-8} \times 70^{3/2} = 48 \mu\mathrm{A}, \tag{3.6}$$

which compares with the 1.2μA detected for the real ion source on the Faraday cup (FC1) after the extraction and after focusing by the ion optics. Recent computer simulations [37] of ion extraction for Ar^+ from the hollow cathode ion source describe the potential distribution and charge density distribution near the extraction hole as well as Ar^+ ion beam shape extracted from the plasma chamber at 20kV of the acceleration voltage.

1. Einzel lens

To obtain the focusing effect on the ions trajectories the radial component of electrostatic field of the electrodes system should be proportional to the distance

from the axis [38]. Consider simple three electrodes arrangement, forming one lens (*Einzellinse* in German means *one lens*) with two outer plates and one inner plate shown on Fig. 7. The equipotential surfaces($\phi = const$, where ϕ is electrostatic potential) represented as dashed lines on the Fig.7 are axially symmetric around the z axis. Since the electric field $\vec{E}$=- gradϕ is perpendicular to these surfaces, the force $\vec{F} = -e\vec{E}$ acting on the electrons is always perpendicular to the equipotential surfaces. Therefore as the equipotential surfaces show curved structure, the acting force has a longitudinal, and as well as a radial components. The longitudinal component accelerates/deccelerates ions as they are passing through the lens depending on the polarity of the applied voltages between A_1, A_2 or A_2 and A_3, while the radial component bent them towards the axis. The symmetrical arrangement of three apertures with potential $\phi_1 = \phi_3 = 0$ and $\phi_2 \neq 0$ represents a combination of collimating and diverging lenses. With a negative voltages applied to A_2 ($\phi_2 < 0$) the positive ions entering from the left are accelerated between A_1 and A_2, but decelerated between A_2 and A_3. The diverging effect then dominates and the whole system acts as a diverging lens, while for $\phi_2 > 0$ a collecting lens is realized. For our experiment we apply 13 kv positive voltage to A_2, this way the Einzel lens was acting as convergent one. The actual Einzel lens used in our experiment was built from three cylinders rather than three plates described above in a simple model, and is shown in Fig. 8. The numerical calculations for triple cylinder Einzel lens system, including spherical aberrations, is available in reference [39].

2. Ion optics

After creating ions in the ion source and extracting them with extraction electrode and forming ion beam with Einzel lens, the ions need to be delivered to the fluorescent chamber without large expanding of the cross section of the ion beam.

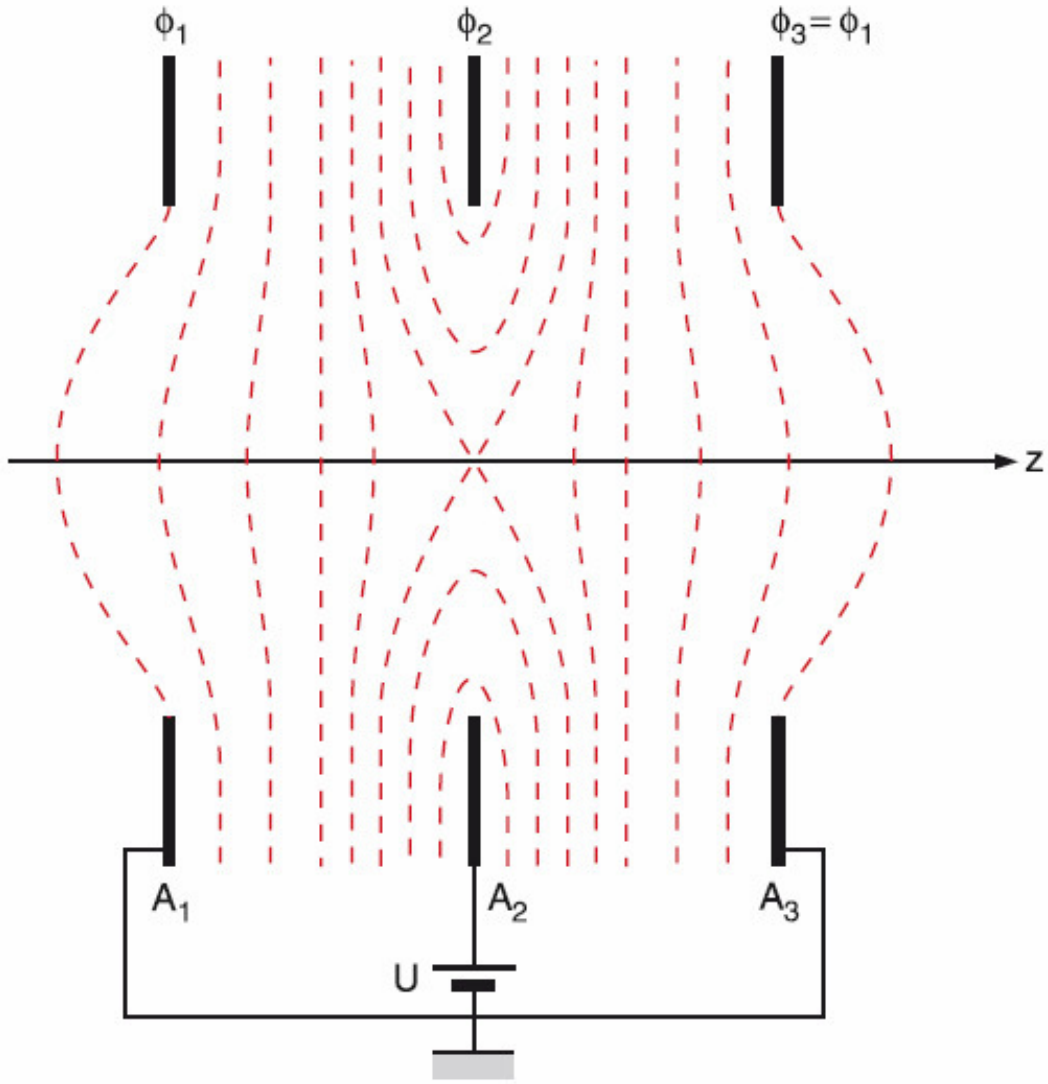

FIG. 7. Einzel lens realized by symmetric arrangement of three plates with different potentials.

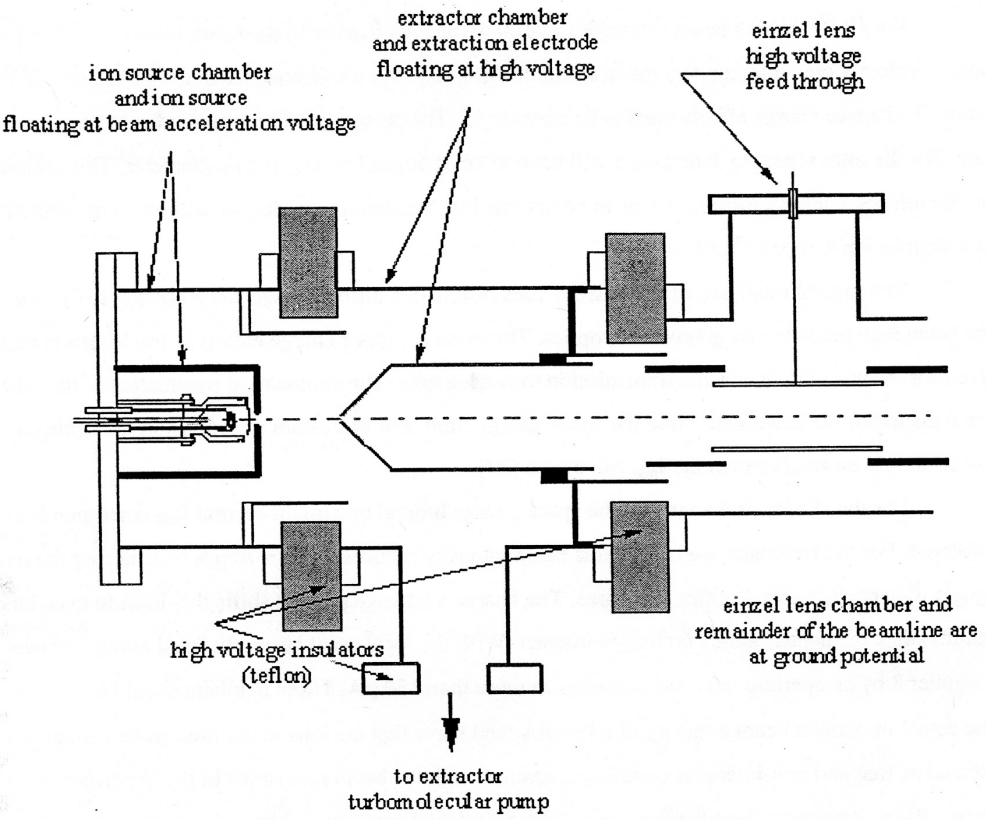

FIG. 8. Einzel lens arrangements for the current experiment.

For that purpose ion optics is employed. An efficient focusing system would require a strong radial field. However in the standard axially symmetrical electric lens, such as Einzel lens, electric field has only a small radial component. (It can be seen in Fig. 7 that electrostatic field, $\vec{E}$, which is perpendicular to equipotential surfaces doesn't have strong radial component.) Therefore the focusing forces of such lens system are weak. Combination of convergent lens and divergent lens allows preserve axial symmetry and obtain strong focusing [40]. A lens is defined as an element in which a charged particle experiences a deflection towards or away from the optical axis, and the angle of bending is proportional to the distance of this particle from the axis. Searching for a lens, one could look for a system in which the x and y components of the electrostatic field strength $\vec{E}$ increase linearly with the distance from the optical axis. One such system is a quadrupole lens. It consists of a four hyperbolically shaped electrodes. Quadrupole lenses are focusing in one plane and defocusing in the perpendicular one. Thus, several such lenses must normally be combined. In the present setup we employed a quartet quadrupole before the magnet and a triplet quadrupole after the magnet. Since hyperbolic electrodes are difficult to fabricate, we approximated the hyperbolas by circular rods. The ion beam trajectories of our system is shown on Fig. 9. Part A represents the vertical yz-plane, and part B illustrates the horizontal xz-plane. The calculation was done by using General Ion Optics System (GIOS) software designed by Dr. Wollnik [41]. Rigorous quantitative description on various quadrupole system, including quadrupole triplet and quadrupole quadruplet is given in reference [42].

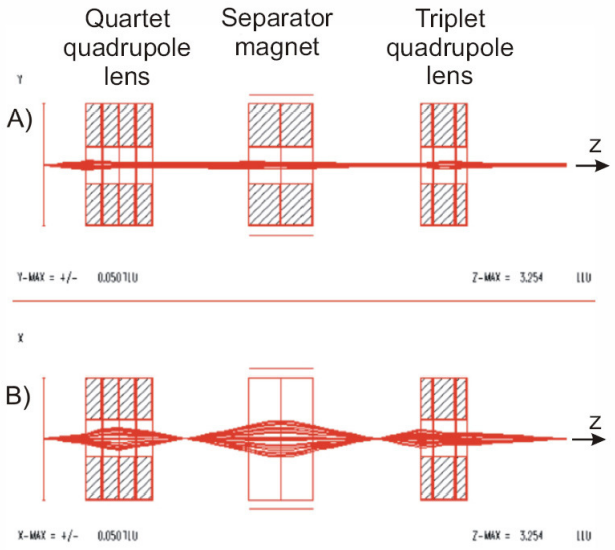

FIG. 9. Ion beam trajectories through the quadrupole quartet, dipole magnet and quadrupole triplet.

C. Acceleration voltage measurements and stability

For precision spectroscopy when measuring the center position of an optical line with least uncertainty, the acceleration voltage must be very stable, since the uncertainty in acceleration voltage will result in an uncertainty of the Doppler shifted center in collinear/anticollinear accelerated ion beams, and hence of the exact transition line position of the ions as well.

1. High voltage measurements with power supply readout and voltage divider

To measure the high voltage from the ion source accelerating voltage, commercial resistive divider chains was employed. It has two outputs, one terminal 1/1,000 (1MΩ) and another terminal 1/10,000 (100kΩ). For our measurements we used 1/10,000 terminal. The output of voltage divider chain was measured with a Keithley digital

multimeter model 2000. According to the specification an accuracy in the range 1V is about 1×10^{-5} V. For a detailed accuracy calculation for a particular voltage reading and environmental temperature the user's manual Keithley digital multimeter model 2000 [43] gives:

$$\begin{aligned} \text{Accuracy} &= \pm(ppm\ of\ reading + ppm\ of\ range) = \\ &= \pm(30ppm \times 1.00509V + 7ppm \times 1V) = 30 \times 10^{-6} + 7 \times 10^{-6} = \\ &= \pm 37\mu V, \end{aligned} \tag{3.7}$$

where ppm=parts per million, e.g., 10ppm=0.001%. The corresponding accuracy in frequency transition domain for the collinear laser spectroscopy is around 500Hz.

$$\text{Accuracy} = \pm 37 \cdot 10^{-6} \times 13.5 \cdot 10^{6} \approx 0.5\text{kHz}. \tag{3.8}$$

The DVM readings from the voltage divider terminal 1/10,000 for two different voltage ranges, 1V and 10V, were compared with readings from high voltage power supply meter. The curves are presented in Fig. 10 and Fig. 11. The fitting parameters are summurized in Table III. A linear function Y=A+B*X fitted by linear regression (least-squares method) gives the following formula for evaluating uncertainties [44]:

$$(\Delta A)^2 = (\delta Y)^2 \cdot \frac{\sum x_i^2}{n \cdot \sum x_i^2 - (\sum x_i)^2}, \tag{3.9}$$

and

$$(\Delta B)^2 = (\delta Y)^2 \cdot \frac{n}{n \cdot \sum x_i^2 - (\sum x_i)^2}, \tag{3.10}$$

where n is the number of the pairs of the sample points (x_i, y_i). These curves were only used for setting the operating parameters, and not for obtaining exact voltage readings, as the absolute voltage is unknown due to the the nature of the ion source operation as a plasma discharge.

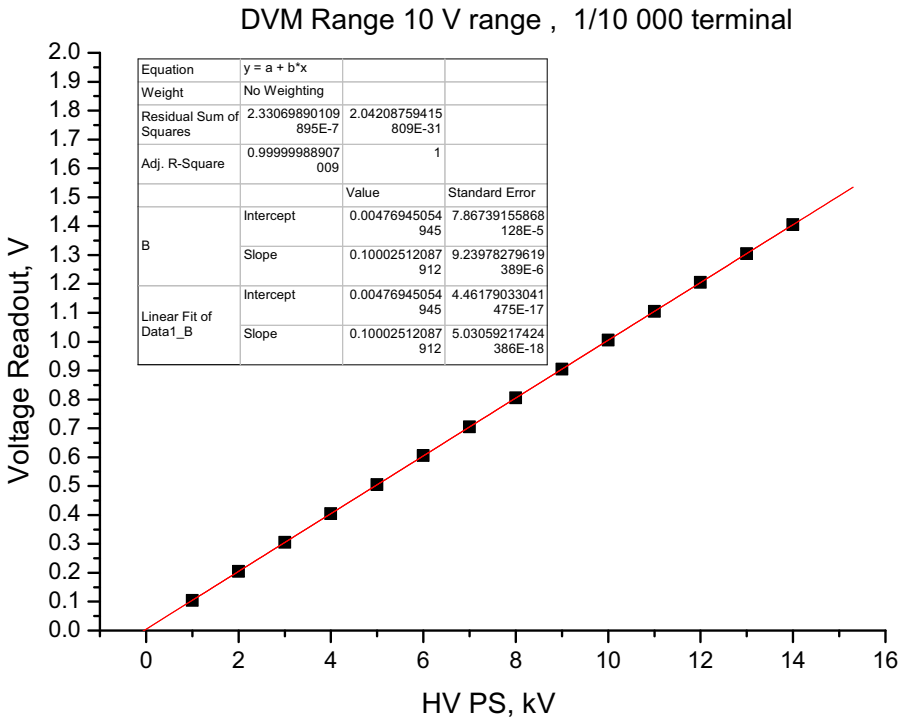

FIG. 10. Digital voltmeter output compared with voltage divider reading, 10 V range.

TABLE III. Calibration of the acceleration voltage parameters fitted by linear function Y=A+B*X in different voltage range.

Voltage range	**Parameter**	**Value**	**Error**
1V	A	0.00471	7.70375E-5
	B	0.10004	1.02188E-5
10V	A	0.00477	7.86739E-5
	B	0.10003	9.23978E-6

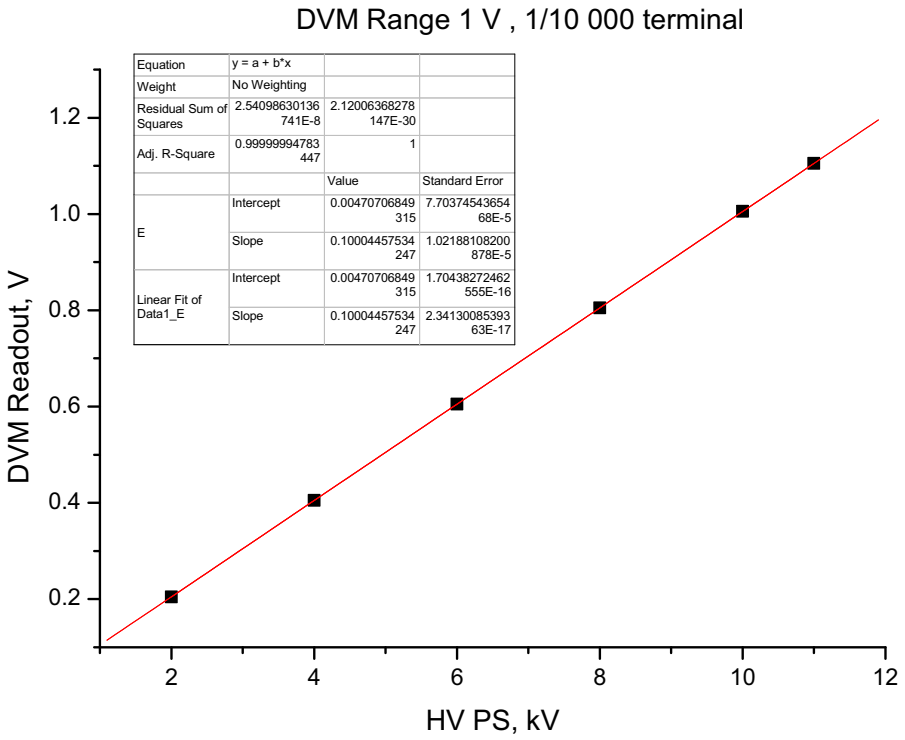

FIG. 11. Digital voltmeter output compared with voltage divider reading, 1 V range.

D. Mass separation of ions

The ions emerging from the ion source were mass separated to yield an isotropically selected ion current. For this a magnetic sector field was used. Particles of mass m, charge Ze, kinetic energy K (or velocity v) are deflected according to their magnetic rigidities χ_B [45]:

$$\chi_B = \frac{mv}{Ze}. \tag{3.11}$$

Thus a particle mass separation system can be implemented, which employs a constant magnetic field that separates particles according to their rigidities. Scanning the magnetic field in such a system, the particles with a range of rigidities are passing the exit slit and are recorded by a Faraday cup, thus providing a mass scan of the charged particles.

1. Dipole magnet

The most common magnetic sector field magnet employs parallel pole faces to create a constant flux density $B_y = B_0 \neq 0,\ B_x = B_z = 0$. In such field all charged particles move along trajectories for which the projection on the plane of the symmetry (y=0) are circles. Such a field exhibits focusing properties in the direction of x (horizontal plane), but not in the direction of y (vertical plane). The purpose of the magnet is to separate from each other ions of different momenta. The fundamental equation [46] describing the motion of a particle with mass m, charge q, and velocity v in a uniform magnetic field of strength B is:

$$\frac{mv^2}{\rho} = qBv. \tag{3.12}$$

The left side is the centripetal force required to make the orbit a circle of radius ρ, while the right side is the centripetal force that is generated by magnetic field acting on the charge q, moving with velocity v. The particles are deflected through

the angle θ given by $\theta = \ell\ /\rho$, where ℓ is the length of the magnet. (The angular displacement θ in radians in motion on the circle by definition is the relation of length of circumference (ℓ) to the radius R). Since ρ is proportional to mv the deflection through a given magnet becomes less as the momentum increase.

2. Mass separation of ions produced by the Danfysik 911A ion source

In order to get a mass separated beam of ions, we need to specify the magnetic field applied to the mass separator. The magnetic field is determined from the second law of Newton, when magnetic filed $\vec{B}$ is acting on a moving charge particle with charge q, velocity v and the rest mass m_0 according to the Lorentz force [47]:

$$\frac{d\vec{p}}{dt} = \frac{d(\gamma m_0 \vec{v})}{dt} = q\vec{v} \times \vec{B}, \tag{3.13}$$

where

$$\vec{p} = \gamma m_0 \vec{v} \tag{3.14}$$

is the momentum of the particle, and $\gamma = (1 - v^2/c^2)^{-1/2}$ is relativistic factor. For general consideration relativistic formulae [48] are taken into account. The energy E of a relativistic particle is described by:

$$E^2 = c^2 p^2 + m_0^2 c^4, \tag{3.15}$$

$$E = \gamma m_0 c^2 = \frac{m_0 c^2}{\sqrt{1 - \frac{v^2}{c^2}}}. \tag{3.16}$$

The kinetic energy T (the portion of the energy associated with the motion) is given by:

$$T = E - m_0 c^2 = m_0 c^2 (\gamma - 1) = m_0 c^2 \left(\frac{1}{\sqrt{1 - \beta^2}} - 1 \right), \tag{3.17}$$

where $\beta = v/c$. From Eq. 3.14 and Eq. 3.16 it follows:

$$\vec{v} = \frac{\vec{p}}{\gamma m_0} = \frac{c^2 \vec{p}}{E}. \tag{3.18}$$

The accelerating potential U applied to the charged particle q transforms potential energy qU into kinetic energy T. The relation between velocity of the particle and potential is obtained from Eq. 3.17 by solving for v:

$$T = qU = m_0 c^2 \left(\frac{1}{\sqrt{1-\beta^2}} - 1 \right), \tag{3.19}$$

and

$$\boxed{v = c\sqrt{1 - \left(\frac{1}{1 + \frac{qU}{m_0 c^2}} \right)^2}}. \tag{3.20}$$

On the other hand from Eq. 3.13 we have relation, connecting radius of the orbit R of the particle with velocity v in magnetic field B:

$$R = \frac{\gamma m_0 v}{qB} = \frac{p}{qB}. \tag{3.21}$$

Combining Eq. 3.20 with Eq. 3.21 and solving for m_0, we obtain:

$$m_0 = \frac{qU}{2c^2} - \frac{R^2 B^2 q}{2U}. \tag{3.22}$$

For our dipole magnet the geometric parameter R=0.25m. The first term in our case is ten orders of magnitude smaller then the second, so we can neglect the first term. With curvature R=0.25m, we obtain proportionality factor:

$$m_0[\text{atomic units (a.u.)}] = \frac{0.25^2 \times 1.6021892 \times 10^{-19}}{2 \times 1.66053886 \times 10^{-27} \times 10^3} = 3015.19 \times \frac{B^2[\text{Tesla}]}{U[\text{kV}]} \tag{3.23}$$

where m_0 mass of the ion as a function of magnetic field B and acceleration voltage U. In our mass calibrating measurements of magnetic field during the mass scan at

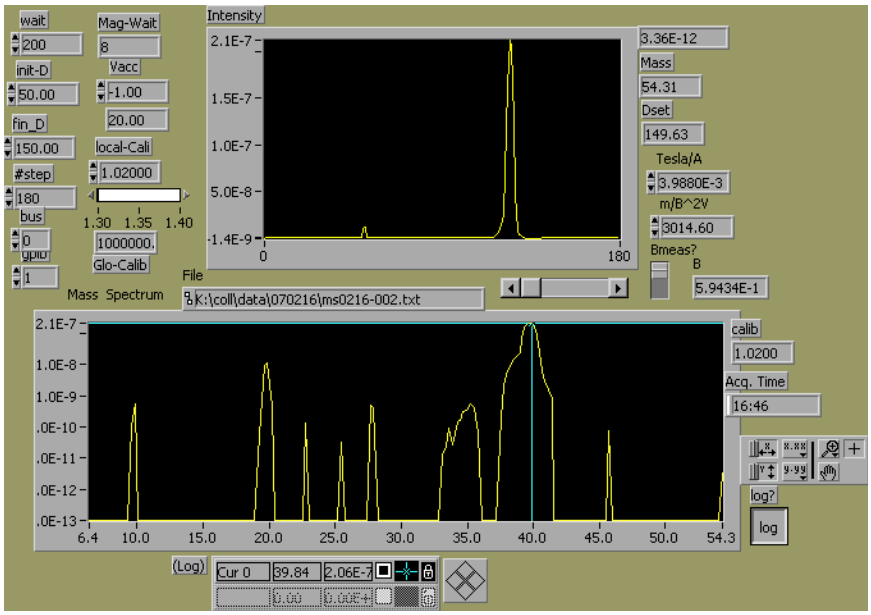

FIG. 12. Mass scan in linear (top) and logarithmic (bottom) scales.

accelerated voltage U_{acc} = 12kV, the peaks corresponding masses of *sodium* (Na) 23a.u. and *potassium* (K) isotopes 39a.u. and 41a.u. were plotted as linear function of mass of the ion m_0 versus square of magnetic field B^2. The slope of such curve, obtained with linear regression method described on page 32, yields a calibrating factor 1.02 to correct the theoretical value for mass m_0 obtained from Eq. 3.23. An example of a mass scan is shown on Fig. 12.

E. Fluorescence detection

1. Photomultiplier

A photomultiplier is a sensitive detector for low-level light intensities. A conventional photomultiplier tube (PMT) is a vacuum device, that contains a photocathode, a number of amplifying stages called dynodes, and an anode that produces the output

signal (Fig. 13).

Photoelectrons are emitted under illumination of the photocathode, which has for our case a semi-transparent *potassium-cesium-antimony* (Bialkali) surface. Then the photoelectrons are accelerated and focused by the operating voltage applied from cathode to the first dynode, which has an extremely high gain *gallium-phosphide* surface. Photo electrons liberated by electron impact from the cathode produce secondary electrons, which are accelerated to the second dynode having a *copper-beryllium surface.* In each step each electron generates $q > 1$ secondary electrons, one photoelectron produces at the N^{th} dynode an electron avalanche of q^n electrons, which are projected on the anode. In our case for the Burle 8850, $N = 12$. The overall gain, G, is extremely sensitive to the voltage, V, because the gain at each dynode is roughly proportinal to the voltage for that step:

$$G \approx (\frac{V}{n})^n, \tag{3.24}$$

where n is the number of dynodes. Then for a small change in voltage $\mathrm{d}V$, the change in gain is given by:

$$\frac{dG}{G} = \frac{ndV}{V}, \tag{3.25}$$

so that 1% change in voltage leads to a 10% change in gain. This requires a HV-power supply of typically 10^{-4} stability. Along the dynode chain the potential increase by equal steps, so that multiplication is repeated at each dynode. The output pulse of charges arriving at the anode produces a voltage pulse across the load resistor. The secondary emission at the dynodes is very fast. The secondary electrons resulting from a delta-function light pulse at the entrance window of the tube arrive at the anode within 3.1×10^{-8} sec. The resulting current pulse at the anode has a correspondingly short duration. Due to the high gain and the short output pulse

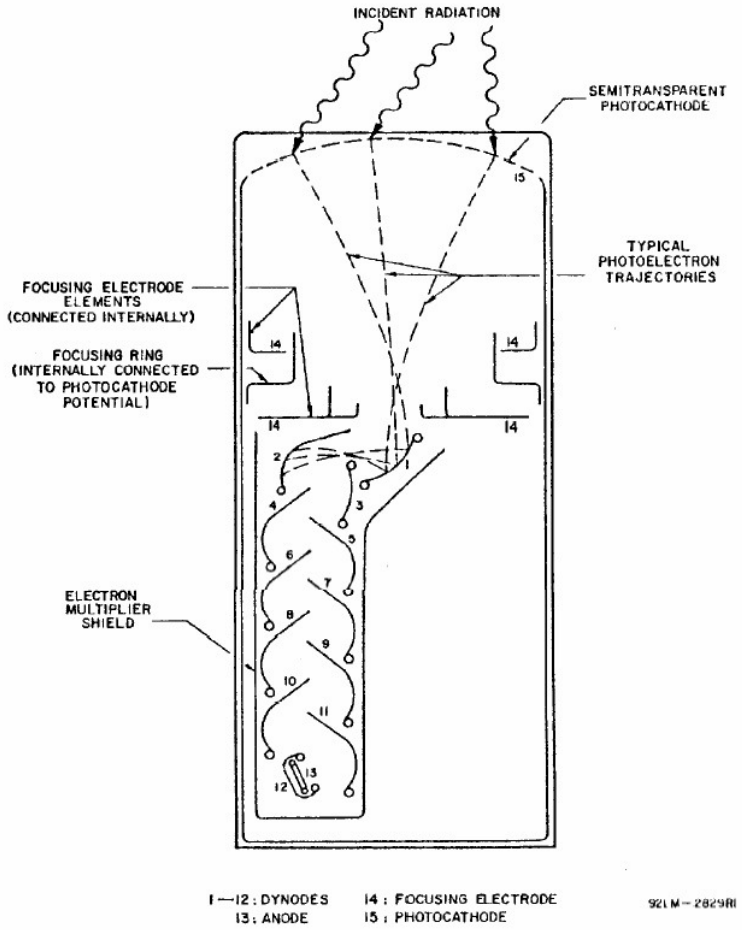

FIG. 13. Functional principle of a conventional photomultiplier tube. The schematical arrangement of the Burle 8850 is presented.

width, a PMT produces easily detectable current pulses for individual photons of a light signal. It should be noted that the gain mechanism in a PMT tube operates as a random process. The number of secondary electrons produced is different for each primary electron. The relative width of the distribution can be expected to be at least of the size of the standard deviation of a Poissonian distribution, $\sqrt{n}$, of the secondary emission coefficient n at the first dynode.

The spectral response of PMT depends on material used for the photocathode. The spectral responce of the Burle 8850, a 51-mm diameter 12-stage, end window Quantacon PMT is shown in Fig. 14. It ideally matches the spectral responce for the required detection scheme, as it has 20% quantum efficiency (QE) at the fluorescence detection range ($\approx$ 460-470nm) and is insensitive (less 1% QE) at the laser excitation wavelength ($\approx$ 611-617nm). The quantum efficiency (QE) is the probability of emission of a photoelectron per incident photon.

Photomultipliers have a wide dynamic range, over which the anode current remains linearly proportional to the intensity of the radiation incident on the photocathode. The dark count rate of the detector sets the limit to the sensitivity. The dark count rate is the highest for cathodes with high sensitivity at long wavelengths. For that reason the Burle 8850 PMT was chosen for our experiments as its sensitivity is limited to 650nm and the typical anode dark current is about 0.6nA. The anode dark current depends on the absolute temperature and follows from the Richardson-Dushman formula [49]:

$$I = DT^2 e^{-\frac{W}{k_B T}}, \tag{3.26}$$

where W is the work funcion of the photocathode , and D is 1.2×10^6 A/(m^{2}K^2).

Cooling the photomultiplier is therefore very effective in reducing background as dark count rate decrease by a factor of 3 to 10 for a 10^0C decrease in temperature. It

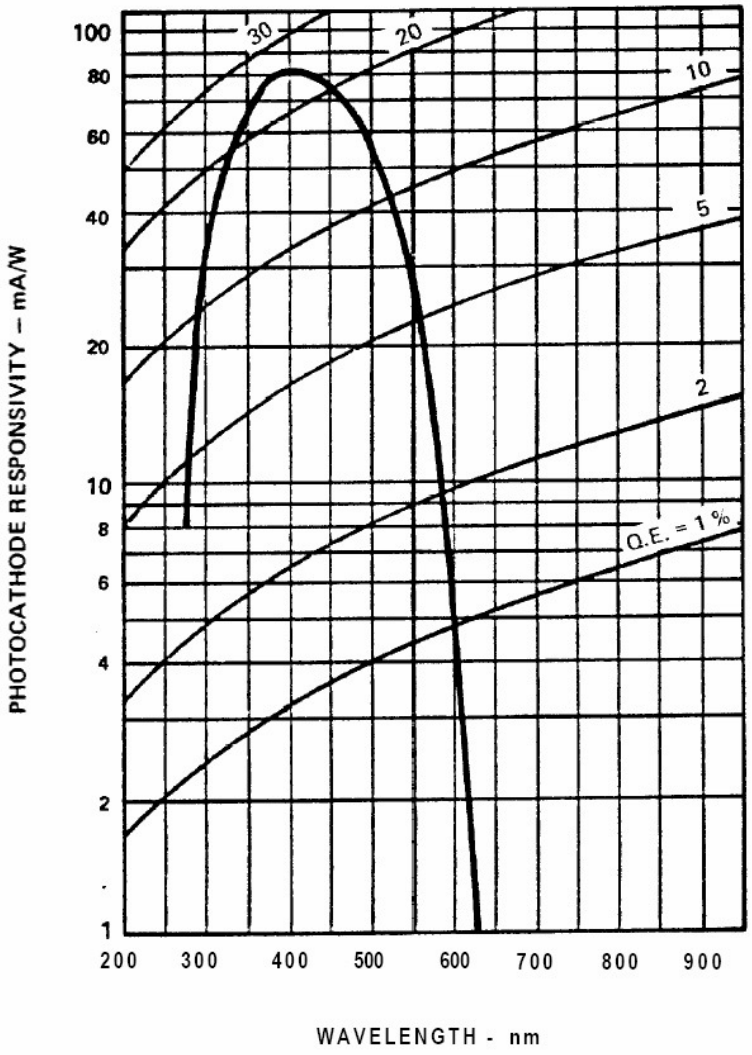

FIG. 14. A photocathode spectral response curve of the Burle 8850 photomultiplier.

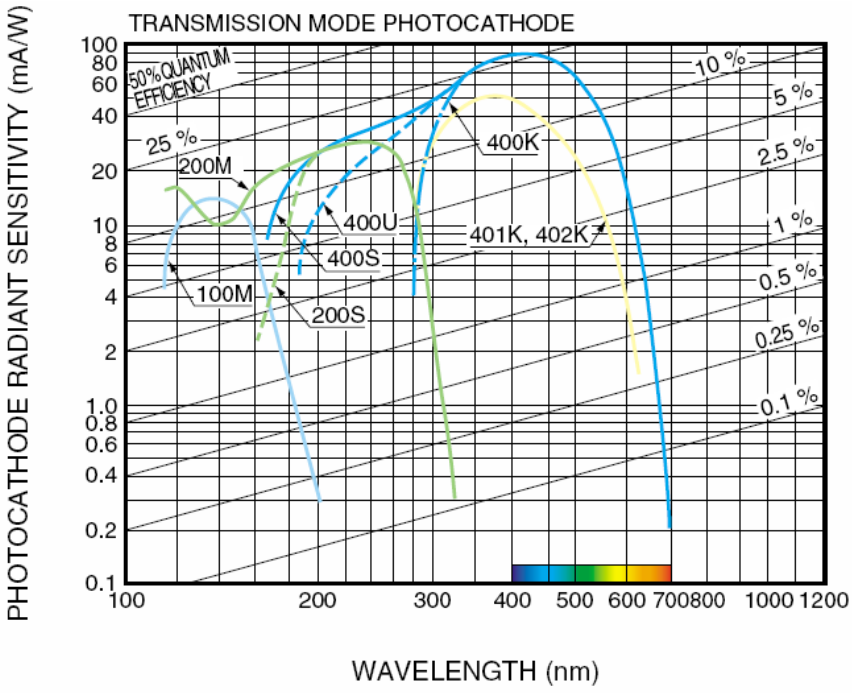

FIG. 15. A photocathode spectral response curve of the Hamamatsu R2256 photomultiplier.

was not necessary to cool the Burle 8850 PMT in the RIKEN experiment. However the PM used at RIKEN in large solid angle elliptical mirror test experiment was cooled to about -20^{0}C. It was Hamamatsu R2256, operating at -2500V with filters Hoya B390, B440, Y44. The sensitivity curve of Hamamatsu R2256 is shown on Fig 15. The corresponding curve is labeled as 400K. It has a very wide spectral response from about 300nm to 850nm. We cooled our photomultiplier for RIKEN measurements with large solid angle elliptical mirror setup as it has wide spectral response into red part of spectra and thus needs to be cooled. The dark current was reduced from 6nA at room temperature to 10pA at about -20^{0}C, which was well suited for photon counting.

It should be pointed out that the dark current increases by a large factor, if

the photocathode is exposed to daylight, even in the absence of applied voltage, and it requires hours to return to its unexposed value. If the cathode of an operating PMT is exposed to daylight or another strong source of light the dark count rate can be permanently increased by several orders of magnitude. Leaving the operating voltage on for an extended time in the dark can sometimes regain the initial low dark current.

2. PMT voltage divider

The usual way of operating a PMT is with the cathode at negative high voltage and the anode at ground. The Burle 8850 PMT was connected to the hight voltage power supply through the voltage divider network assembly AJ2335. The assembly is packed in metal housing with an SHV connector for the high voltage and BNC connectors for the anode signal.

3. Condensor lens

To be able detect the fluorescent light by the photomultiplier we need to form the real image of the fluorescence region onto photocathode surface of the PM. The condesor lens system is optimal for such purpose. To reduce the spherical aberrations the condesor is split into two elements [50]. The convex-flat lens has the least spherical aberrations [51], and the system of two lenses oriented as shown in Fig. 16 was optimal for error lens with the flat sides of the condesor lenses facing the light source and image. For our system the spherical surfaces of two identical lenses are touching each other and optical strength of such system is doubled. To determine the optical parameters of the condesor system the matrix method was employed [52]. The C++ code for calculation the main optical parameters [53] of the condensor lens system are presented in Appendix C.

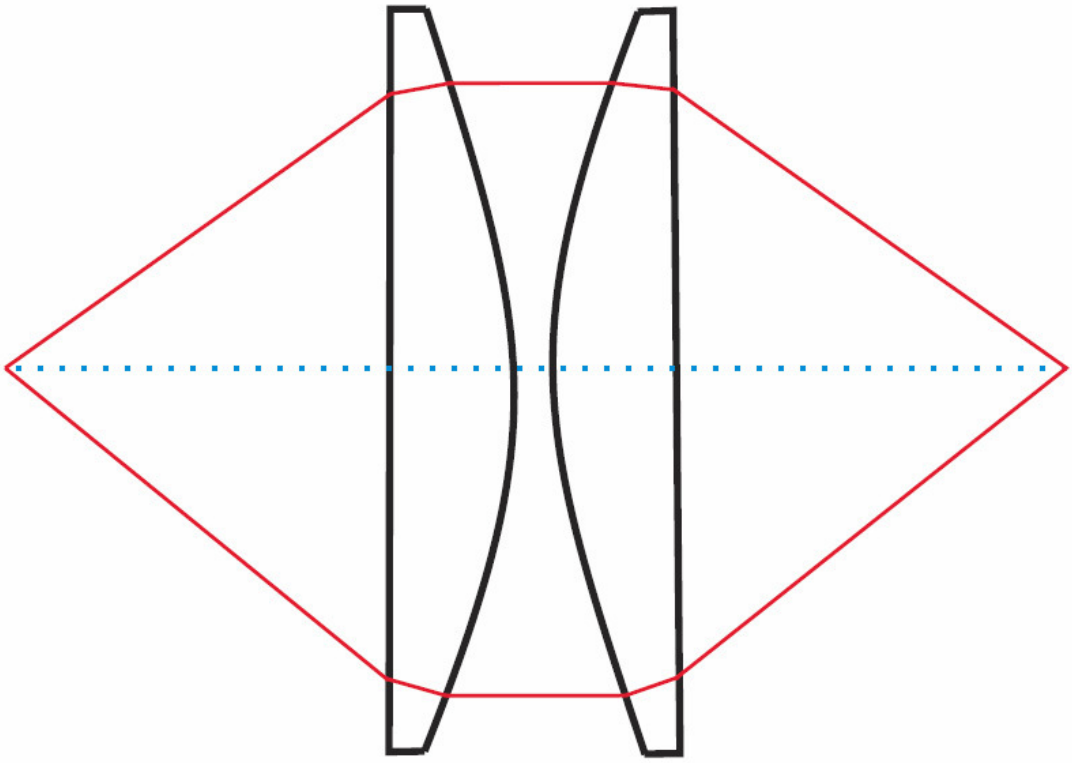

FIG. 16. Condenser lens system.

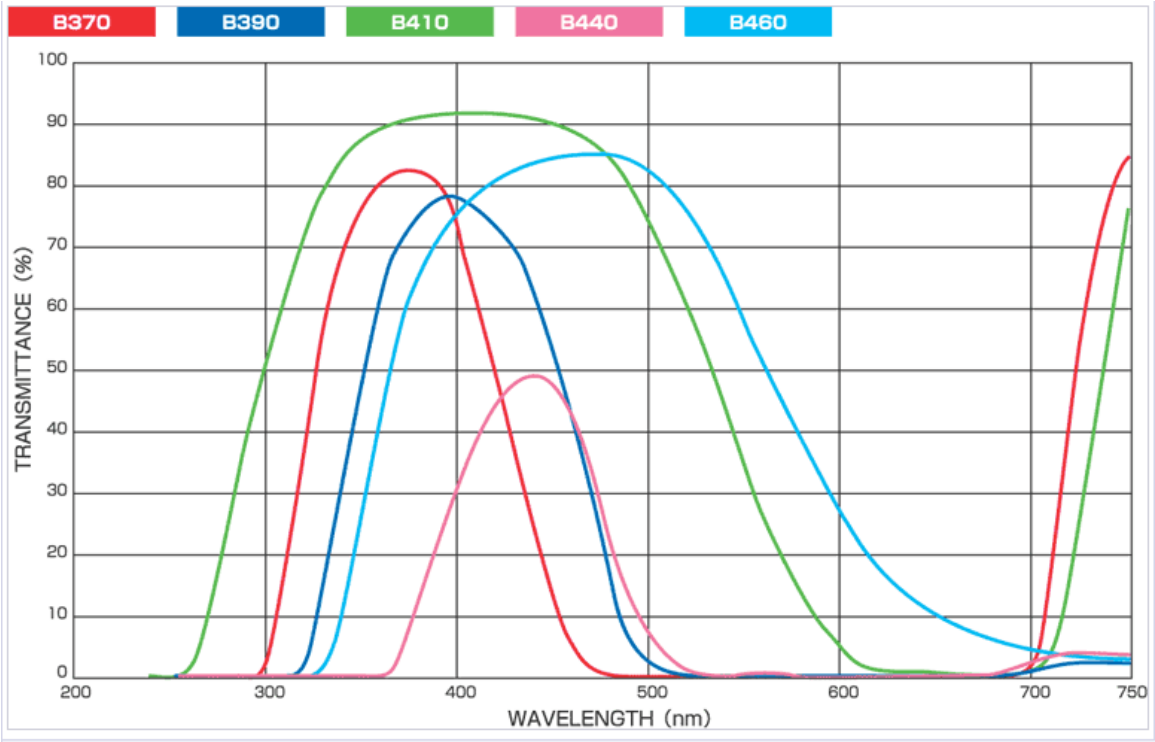

FIG. 17. Blue filters.

4. Optical filters

Filters are used to select a special emission wavelength and if different to suppress the excitation light in fluorescence experiments, as well as to adjust the intensity of a light signal. Filters can be based on absorption in colored glass or on reflection and interference in a stack of dielectric and metal layers. The transmission of the filters used in our system is depicted in Fig. 17, 18 and detailed information of those filters presented in Fig. 19, 20, 21. We employ the filters B390, B440 to suppress excitation line at 611nm and Y44 to suppress ion beam collision fluorescence in UV. The combined small reduction effect in the detection window of interest is about $\eta = 0.1795$, while the suppression at the excited laser wavelength of 611nm is

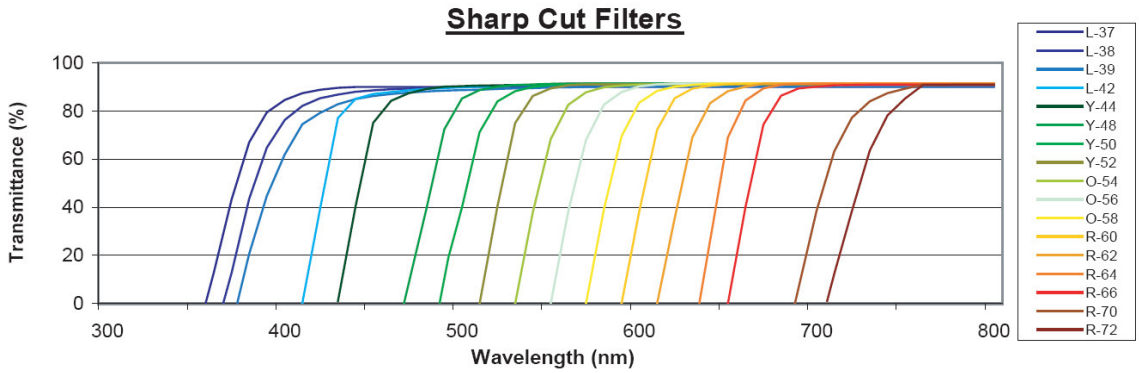

FIG. 18. Sharp cut filters.

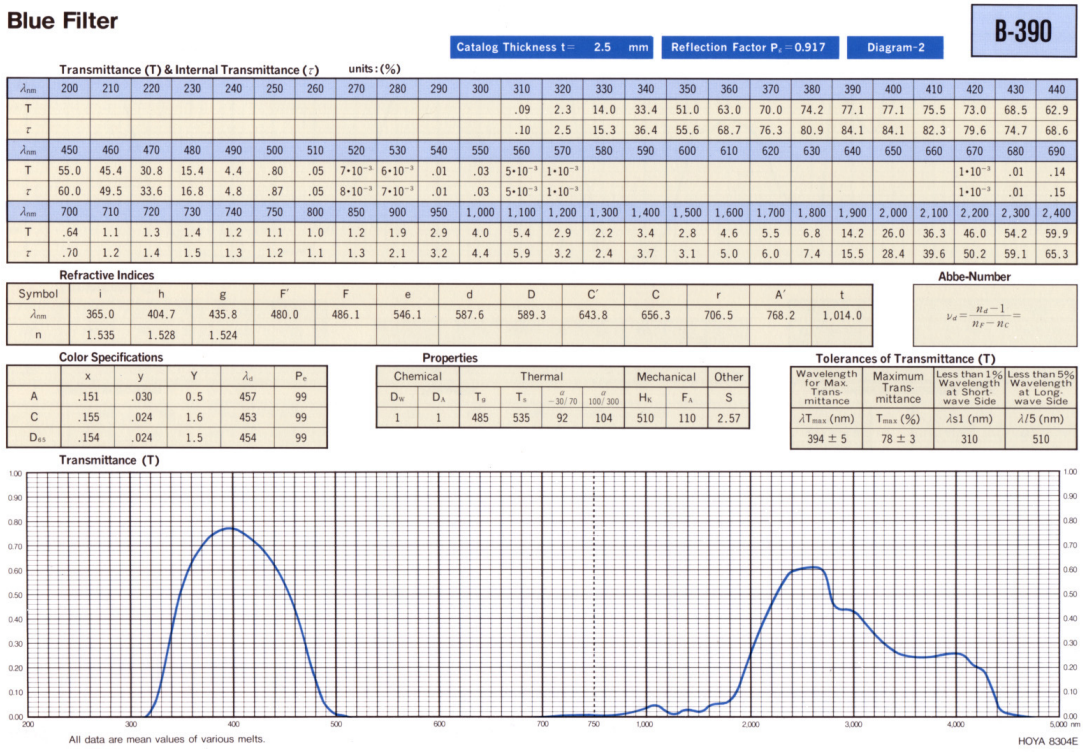

FIG. 19. Transmission curve of the B390 filter.

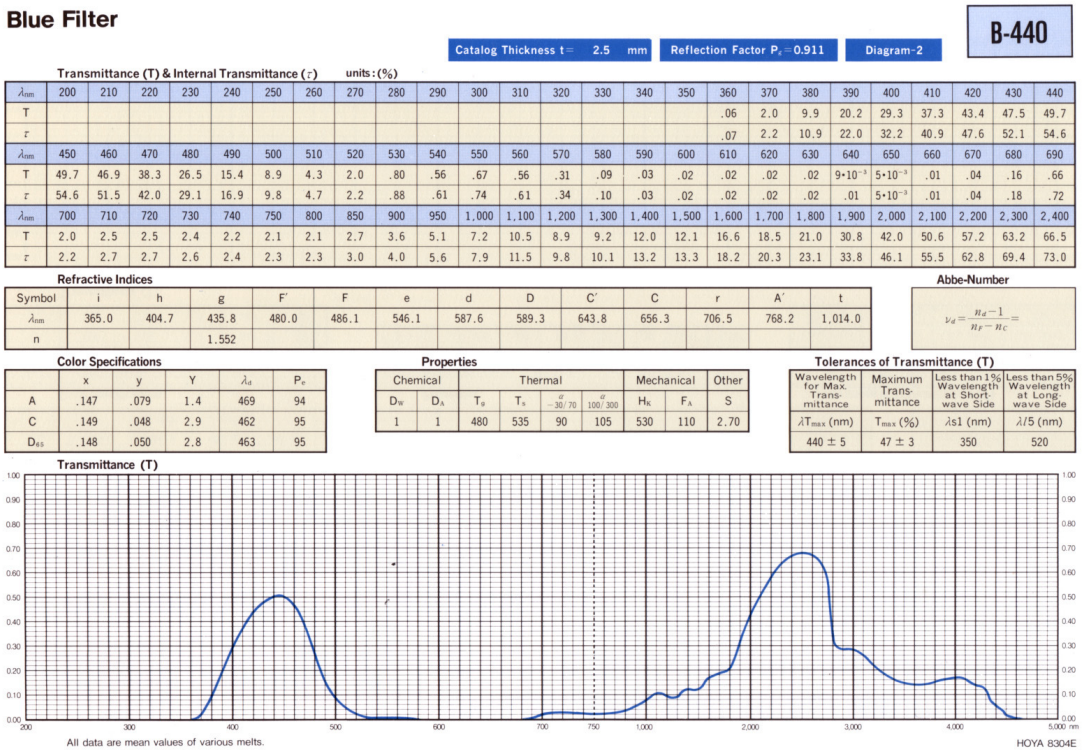

Blue Filter

B-440

Catalog Thickness t= 2.5 mm | Reflection Factor P_s=0.911 | Diagram-2

Transmittance (T) & Internal Transmittance (τ) units: (%)

λnm	200	210	220	230	240	250	260	270	280	290	300	310	320	330	340	350	360	370	380	390	400	410	420	430	440
T																	.06	2.0	9.9	20.2	29.3	37.3	43.4	47.5	49.7
τ																	.07	2.2	10.9	22.0	32.2	40.9	47.6	52.1	54.6
λnm	450	460	470	480	490	500	510	520	530	540	550	560	570	580	590	600	610	620	630	640	650	660	670	680	690
T	49.7	46.9	38.3	26.5	15.4	8.9	4.3	2.0	.80	.56	.67	.56	.31	.09	.03	.02	.02	.02	.02	$9\cdot10^{-3}$	$5\cdot10^{-3}$	.01	.04	.16	.66
τ	54.6	51.5	42.0	29.1	16.9	9.8	4.7	2.2	.88	.61	.74	.61	.34	.10	.03	.02	.02	.02	.02	.01	$5\cdot10^{-3}$	.01	.04	.18	.72
λnm	700	710	720	730	740	750	800	850	900	950	1,000	1,100	1,200	1,300	1,400	1,500	1,600	1,700	1,800	1,900	2,000	2,100	2,200	2,300	2,400
T	2.0	2.5	2.5	2.4	2.2	2.1	2.1	2.7	3.6	5.1	7.2	10.5	8.9	9.2	12.0	12.1	16.6	18.5	21.0	30.8	42.0	50.6	57.2	63.2	66.5
τ	2.2	2.7	2.7	2.6	2.4	2.3	2.3	3.0	4.0	5.6	7.9	11.5	9.8	10.1	13.2	13.3	18.2	20.3	23.1	33.8	46.1	55.5	62.8	69.4	73.0

Refractive Indices

Symbol	i	h	g	F′	F	e	d	D	C′	C	r	A′	t
λnm	365.0	404.7	435.8	480.0	486.1	546.1	587.6	589.3	643.8	656.3	706.5	768.2	1,014.0
n			1.552										

Abbe-Number

$$\nu_d = \frac{n_d - 1}{n_F - n_C} =$$

Color Specifications

	x	y	Y	λ_d	P_e
A	.147	.079	1.4	469	94
C	.149	.048	2.9	462	95
D_{65}	.148	.050	2.8	463	95

Properties

Chemical		Thermal				Mechanical		Other
D_W	D_λ	T_g	T_s	$\alpha_{-30/70}$	$\alpha_{100/300}$	H_K	F_A	S
1	1	480	535	90	105	530	110	2.70

Tolerances of Transmittance (T)

Wavelength for Max. Transmittance	Maximum Transmittance	Less than 1% Wavelength at Short-wave Side	Less than 5% Wavelength at Long-wave Side
λT_{max} (nm)	T_{max} (%)	$\lambda s1$ (nm)	$\lambda l5$ (nm)
440 ± 5	47 ± 3	350	520

Transmittance (T)

All data are mean values of various melts.

HOYA 8304E

FIG. 20. Transmission curve of the B440 filter.

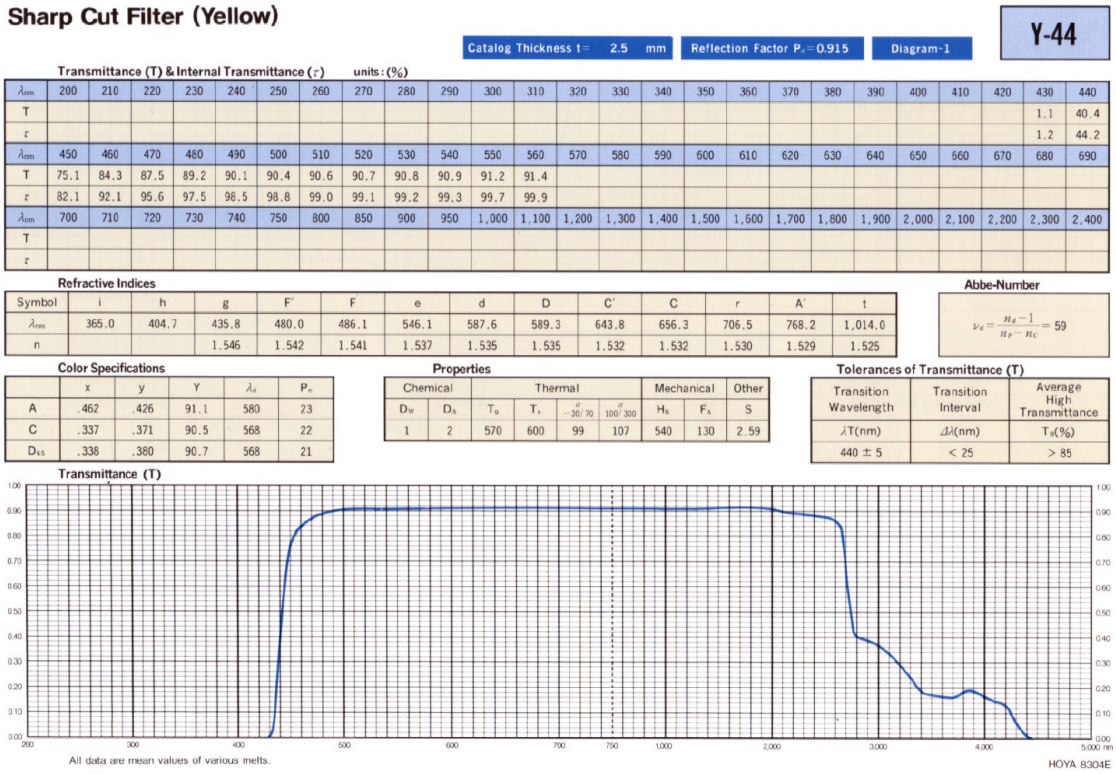

Sharp Cut Filter (Yellow)

Y-44

Catalog Thickness t= 2.5 mm | Reflection Factor P_r=0.915 | Diagram-1

Transmittance (T) & Internal Transmittance (τ) units: (%)

λ_{nm}	200	210	220	230	240	250	260	270	280	290	300	310	320	330	340	350	360	370	380	390	400	410	420	430	440
T																								1.1	40.4
τ																								1.2	44.2
λ_{nm}	450	460	470	480	490	500	510	520	530	540	550	560	570	580	590	600	610	620	630	640	650	660	670	680	690
T	75.1	84.3	87.5	89.2	90.1	90.4	90.6	90.7	90.8	90.9	91.2	91.4													
τ	82.1	92.1	95.6	97.5	98.5	98.8	99.0	99.1	99.2	99.3	99.7	99.9													
λ_{nm}	700	710	720	730	740	750	800	850	900	950	1,000	1,100	1,200	1,300	1,400	1,500	1,600	1,700	1,800	1,900	2,000	2,100	2,200	2,300	2,400
T																									
τ																									

Refractive Indices

Symbol	i	h	g	F′	F	e	d	D	C′	C	r	A′	t
λ_{nm}	365.0	404.7	435.8	480.0	486.1	546.1	587.6	589.3	643.8	656.3	706.5	768.2	1,014.0
n			1.546	1.542	1.541	1.537	1.535	1.535	1.532	1.532	1.530	1.529	1.525

Abbe-Number

$$\nu_d = \frac{n_d - 1}{n_F - n_C} = 59$$

Color Specifications

	x	y	Y	λ_d	P_e
A	.462	.426	91.1	580	23
C	.337	.371	90.5	568	22
D_{65}	.338	.380	90.7	568	21

Properties

Chemical		Thermal				Mechanical		Other
D_w	D_λ	T_g	T_s	$\alpha^{\circ}_{-30/70}$	$\alpha^{\circ}_{100/300}$	H_k	F_λ	S
1	2	570	600	99	107	540	130	2.59

Tolerances of Transmittance (T)

Transition Wavelength	Transition Interval	Average High Transmittance
λT(nm)	$\Delta\lambda$(nm)	T_H(%)
440 ± 5	< 25	> 85

Transmittance (T)

All data are mean values of various melts.

HOYA 8304E

FIG. 21. Transmission curve of the Y44 filter.

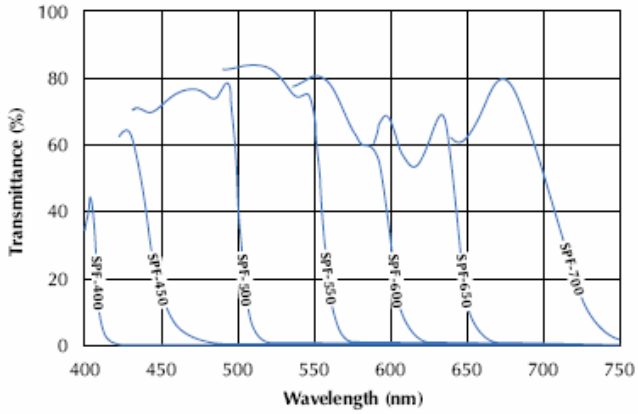

FIG. 22. Interference filter SPF-500 CVI Laser Co.

$\eta = 1.8 \times 10^{-9}$.

Interference filters are made by depositing a series of dielectric and metallic layers on a glass substrate. The basic principle behind interference filters is that the individual reflections should interfere constructively/destructively to enhance/cancel their reflection amplitudes. In the Vancouver experiment we used interference filter SPF-500 CVI Laser Co. Its transmission curve is presented in Fig. 22.

5. The large solid angle elliptical mirror setup

If the detection efficiency is to be increased, the largest potential lies in improving in the optical system by employing a large solid angle. Not much can be gained by improving the detector, since we are already using optimized PM's. The collecting solid angle (Fig. 23) depends on the angle subtended by the imagining optics:

$$\Omega = \int d\Omega = 2\pi \int_0^{\theta} \sin\theta' d\theta' = 2\pi \left(1 - \cos\theta\right). \tag{3.27}$$

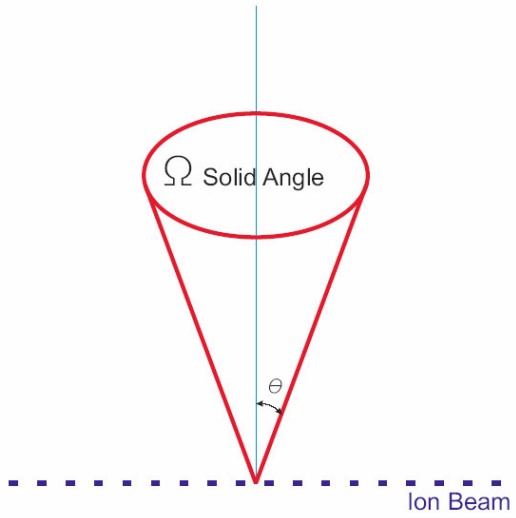

FIG. 23. Solid angle subtended of by imagining optics.

For our elliptical mirror $\theta = 143°$. Therefore:

$$\Omega_{\text{elliptical mirror}} = 2\pi\left[1 - \cos(143°)\right] = 11.3\text{srad}. \tag{3.28}$$

For our arrangement, we need to subtract the solid angles which correspond to the side holes in the mirror: one with $\theta_1 = 18.6°$ (solid angle $\Omega_1 = 0.33$srad and two with $\theta_2 = 15.7°$ (solid angle $\Omega_2 = 0.24$srad each). Then the total collecting solid angle of the mirror is:

$$\Omega_{\text{elliptical mirror}} = 11.3 - 0.33 - 2 \times 0.24 = 10.5\text{srad}. \tag{3.29}$$

For comparison, we list the corresponding data for the condensor setup. The schematic layout of condensor lens setup is presented in Fig. 24. For the condensor lens the collecting aperture diameter is 50.8mm and the distance to the ion beam, where fluorescence occurs is 57.5mm. According to the formula 3.27 and Fig. 23 that

forms a solid angle 0.535srad, which corresponds only 4.3% of the total solid angle of 4π. Taking into account that we used an additional spherical mirror to collect light propagating on the other side of the ion beam, we have an multiplication factor 2. Then the total solid angle is $\Omega_{\text{condensor lens}} = 1.07$srad. The total improvement in efficiency η one could expect for elliptical mirror is:

$$\eta = \frac{10.5}{1.07} \approx 9.8. \tag{3.30}$$

The elliptical mirror optical detection system was designed and tested. The schematic drawing of elliptical mirror is presented in Fig. 25. The first test was performed at TRIUMF, Vancouver, Canada, using the same ArII lines, namely, the transition between the metastable $^2G_{9/2}$ state (154181.4942 cm^{-1}) and the excited $^2F^o_{7/2}$ state (170530.4041 cm^{-1}) with the wavelength $\lambda = 611.6616$nm. The fluorescence observed as the signal (Fig. 26) is mainly between $^2F^o_{7/2}$ and $^2D_{5/2}$ (148842.4674 cm^{-1}) states. See Fig. 37 for detailed ArII energy level scheme. The photomultiplier had dark count rate 200 counts/s at 1800 V. The laser power was 230 mW at the laser output, but due to various optical elements was about 60 mW at the beamline input, the transmitted beam was $\approx$ 5mW, so a large portion of the light was lost on apertures and produced unwanted scattered light. There is also the ion beam fluorescence from the energetic ion beam, when it impacts on the residual gas atoms. This is called *Huhnermann Leuchten.* It was efficiently blocked by Hoya Y44 filter. The total count rate of background was 500 cps with the ion beam on, and laser off. There was a lot of directly scattered light from the laser, which increased the count rate to 10^5 cps with the ion beam on, and laser on. To further reduce this laser light and part of the beam fluorescence, an SPF-500 interference filter was used from CVI Laser Co. It has $\approx$ 80 % transmission below 500 nm and about 10^{-4}

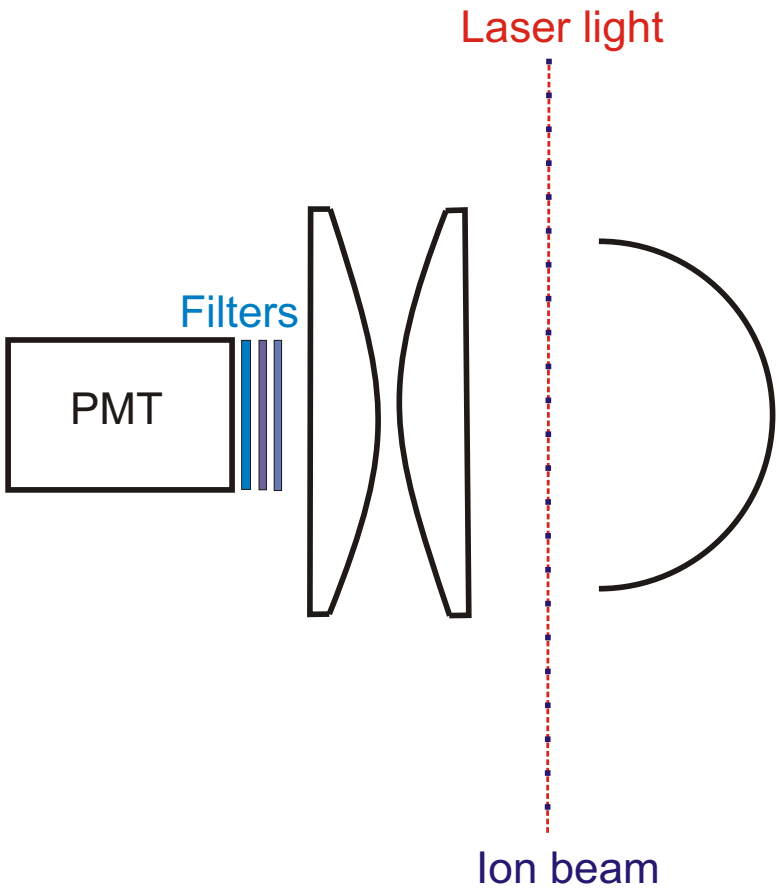

FIG. 24. Condenser lens, Edmund Optics 51 mm diameter.

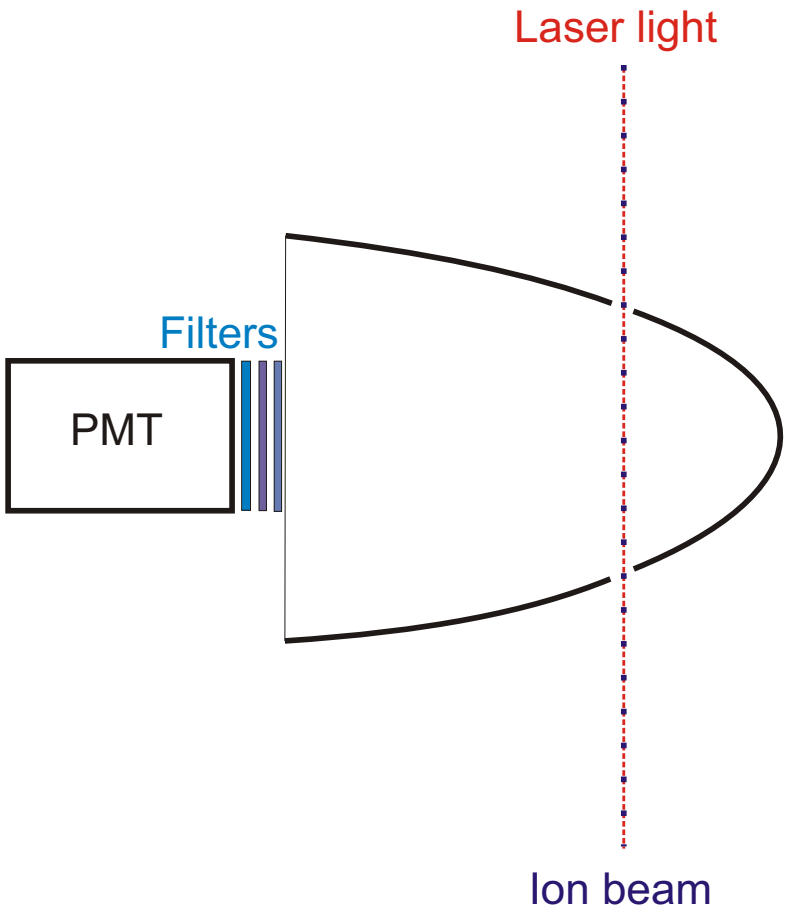

FIG. 25. The large solid angle elliptical mirror setup.

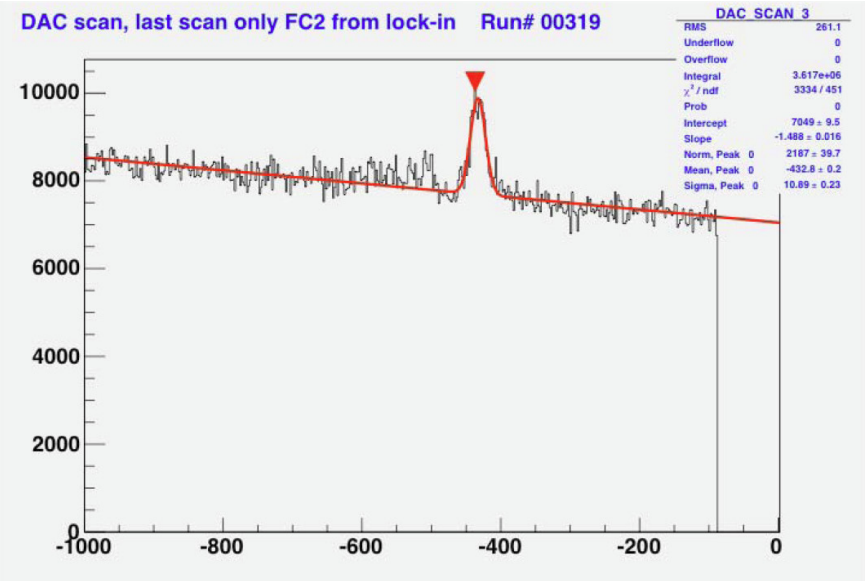

FIG. 26. Vancouver's resonance signal with elliptical mirror setup.

at the laser wavelength $\lambda = 611.6616$nm. With this filter the background count rate was reduced to 2800 cps with laser on, ion beam off, 3300 cps with the ion beam on, laser on. The values of PMT background count rates are combined in Table IV. Since the beam time at TRIUMF was limited to 12 hours not much readjustment of the laser beam could be made, once a signal observed. The resulting conclusion on the large solid angle elliptical mirror setup tested in Vancouver and in RIKEN is summarized in Tab. V and Tab. VI. The elliptical mirror proved to be efficient one by the factor of 3 more than it was predicted, but with large uncertainty in the ion beam current measurements. It is explained by the fact that the iop optics design was not optimized for elliptical mirror setup, as well as the ion beam current was measured with 4-plate detector after condensor lens setup, while Faraday cup was used after eliptical mirror setup. The set of filters used with the condesor setup was B390 and SPF-500, while with elliptical mirror setup we installed B390, SPF-500,

TABLE IV. Laser background parameters.

PMT	**Laser on Beam on**	**Laser on Beam off**	**Laser off Beam on**	**Laser off Beam off**
Voltage, V	*count rate, cps*	*count rate, cps*	*count rate, cps*	*count rate, cps*
1800	10^5	10^5	500	200
Interference filter added: SPF-500 CVI Laser Co				
1800	3300	2800	500	200
1900	7000	4200	600	300

TABLE V. RIKEN, TRIUMF, Texas A&M data parameters comparison.

Experim.	**Linewidth, MHz**	**S/N ratio**	**Beam current, nA**
TRIUMF, elliptical mirror	270	1:4	18
RIKEN, elliptical mirror	115.08 ±2.94	1:4.3	8
Texas A&M, condenser lens	96.44 ±0.166	1:17	890

TABLE VI. Efficiency calculation for elliptical mirror and condenser lens.

	Texas A&M setup	**Elliptical mirror, RIKEN**
QE of PMT at 461,468nm	0.2	0.2
Ion current	890 nA	8 nA
Filters	1	0.454×0.843=0.383
Solid angle	1.07 srad	10.5 srad
Signal, cps	143030	9936
Efficiency, cps/nA	$\frac{0.2\times1.07\times143030}{4\pi\times890}$ =2.74	$\frac{0.2\times10.57\times9936\times0.383}{4\pi\times8}$ =79.5
Relative efficiency	1	$\frac{79.5}{2.74} = 29$
(calculated 9.8, factor 3 due to the ion current measurements)		

and Y44. For simplicity of comparison between those two systems, we normalized transmission of condensor lens setup as 1. Thus only extra filters put into elliptical mirror have to be counted.

F. Laser system

For spectroscopy applications a cw dye laser was used (Coherent 899-21) both at ISAC and at RIKEN. The most important attribute of the dye laser is its tunability, which gives access to any wavelength in the visible and near visible spectrum. The spectral range of the KR-620 dye employed is 610∼670 nm. The typical output intensity of the laser radiation with a bandwidth of about 1MHz at 611nm was 700mW. The measured intensity of the laser beam at the end of the collinear fast beam apparatus was about 1mW. The RIKEN dye laser system is described in detail in Dr. Takamine's doctoral thesis [54]. The pumping laser for the dye laser was

high power diode laser at 532nm (Verdi^{TM} V10) with a typical output power 8W. A schematic diagram of the laser system for spectroscopy measurements is shown in Fig. 27. To monitor the ring dye laser wavelength a commercial wavemeter was used (Advantest Q8326). It utilizes a He-Ne laser for the reference wavelength and employs a Michelson interferometer to obtain an accuracy 5 ppm (parts per million) for the wavelength range $\approx$ 600 nm. For production reference markers the ring dye laser was monitored with a Fabry-Perot interferometer with a free spectral range of 252.69(38)MHz using a silicon photodetector. To obtain an absolute reference Doppler free and Doppler limited iodine spectroscopy were applied. Tabulated reference values of iodine spectra are available in reference [55]. The iodine spectroscopy apparatus was incorporated in our laser system and is shown in Fig. 27. The laser light was split into pump and probe beams as well as a reference beam. The laser beam intensities were adjusted by rotating $\lambda/2$ plates. Typically the power of the pump beam was $\approx$ 10mW. The pump laser beam and the reference laser beam were modulated with choppers at a frequency $\approx$ 1.5kHz and a duty cycle of 50%. The reference signal was TTL (0/+5V) level signal generated from the reference laser beam by a silicon photodetector and connected to the dual phase lock-in amplifier (Edmund Optics model 420). The probe laser signals were also connected to the lock-in amplifier and the Doppler-free spectra was observed as output signals of the lock-in amplifier. The sensitivity of the lock-in amplifier was 300μV and time constant was 30ms.

G. Frequency comb

For precise measurements of the laser wavelength the optical frequency synthesizer FC1500 (Menlo Systems GmbH) was used. The FC1500 is based on a femtosecond fiber laser frequency comb. This frequency comb is well suited for precision spec-

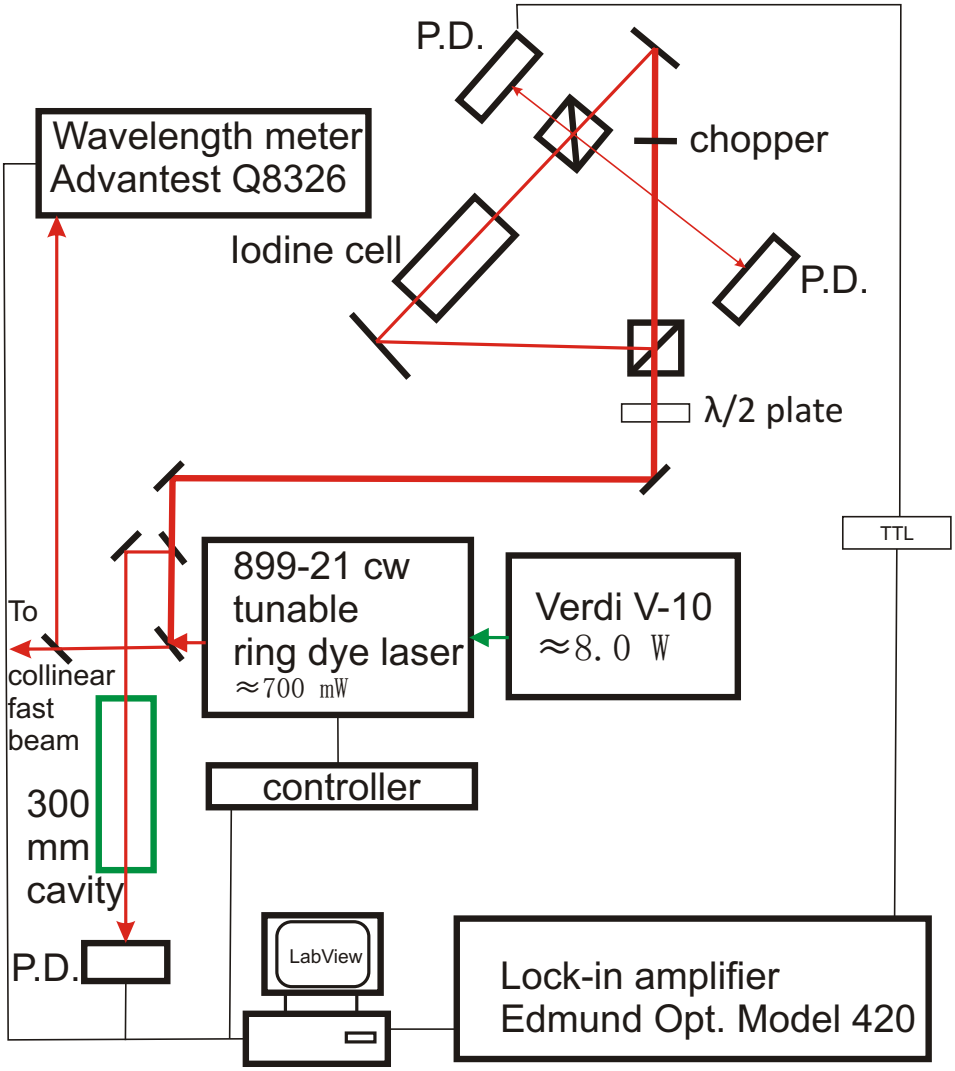

FIG. 27. Laser system for spectroscopy measurements.

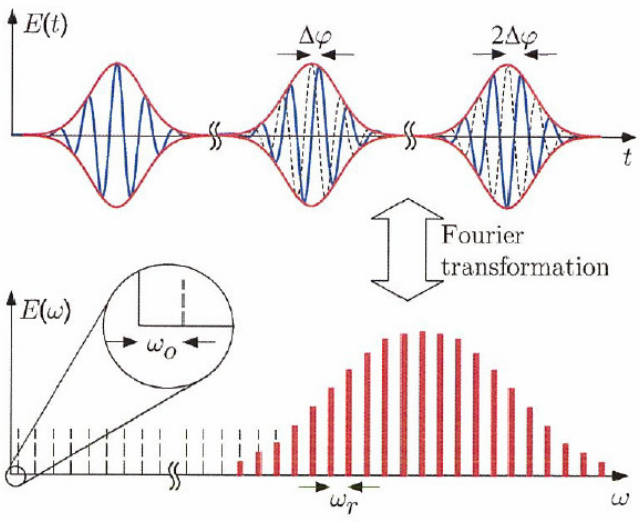

FIG. 28. Frequency comb.

troscopy, since the repetition frequency of 250MHz (also the mode spacing) allows wide tunability of up the spectroscopy laser over a range of $\omega_{rep}/2 \approx 125$MHz. Lower panel of Fig. 28 shows the mode structure of a femtosecond frequency comb, where the laser pulse is circulating in a laser cavity with length L with a carrier frequency ω_c. The output of such laser is a sequence of pulses as shown in upper panel of Fig. 28. The pulses are spaced at intervals t_{rep}, the photon round trip in the cavity, and the FWHM of each pulse is called t_p. The carrier waves within the pulse envelopes travel at phase velocity, ω/k, while the pulses themselves travel at the group velocity $d\omega/dk$. The phase of the carrier wave at the peak of a pulse is called the carrier-envelope offest φ_{ceo}. The change in this offset per round trip in the laser cavity is:

$$\Delta\varphi_{ceo} = \int_0^L \omega\left(\frac{dx}{v_{gr}} - \frac{dx}{v_{ph}}\right), \tag{3.31}$$

where L is the round trip length, and v_{gr} is the group velocity, and v_{ph} is the phase velocity. It is useful to define the carrier offset frequency:

$$\omega_{ceo} = \frac{\Delta\varphi_{ceo}}{t_{rep}}. \tag{3.32}$$

Then the individual pulse has an electric field of the form:

$$A(t)e^{i(\omega_c+\omega_{ceo})t}, \tag{3.33}$$

where ω_c is the mean angular frequency of the carrier waves in the pulse, and $A(t)$ is the pulse envelope. Then the electric field of the pulse train is the convolution of the individual pusle shape with δ-functions spaced at intervals t_{rep}:

$$E(t) = A(t)e^{i\omega_c t}\sum\delta(t - mt_{rep})e^{i\omega_{ceo}t}. \tag{3.34}$$

The Fourier transform of the first component in this convolution is:

$$\int A(t)e^{i(\omega_c-\omega)t}dt = a(\omega - \omega_c), \tag{3.35}$$

where $a(\omega)$ is the Fourier transform of A(t). For simplicity the sequence of pulses is assumed to continue indefinitely. We can then use the Poisson summation theorem [49] to re-express part of the second component of the convolution:

$$\sum_m \delta(t - mt_{rep}) = \frac{1}{t_{rep}}\sum_n e^{i\omega_{rep}nt}, \tag{3.36}$$

where $\omega_{rep} = 2\pi/t_{rep}$. Although this theorem requires that m and n should both be integers running from minus to plus infinity, the actual pulse trains are sufficiently long for the summation formula to be reliable. Thus the second component in the convolution is:

$$\sum_m \delta(t - mt_{rep})e^{i\omega_{ceo}t} = \frac{1}{t_{rep}}\sum_n e^{i(n\omega_{rep}+\omega_{ceo})t}, \tag{3.37}$$

whose Fourier transform is $\sum_n \delta(\omega - n\omega - \omega_{ceo})/t_{rep}$. The Fourier transform of a convolution is the product of transforms , hence the Fourier transform of the electric field given in Eq. 3.34 is:

$$e(\omega) = \left[\frac{a(\omega - \omega_c)}{t_{rep}}\right] \sum_n \delta(\omega - n\omega_{rep} - \omega_{ceo}). \tag{3.38}$$

This function is displayed in the lower panel of Fig. 28 and forms the optical comb with very narrow spectral lines at the frequencies:

$$\omega = n\omega_{rep} + \omega_{ceo}, \tag{3.39}$$

with a large ($\approx 10^6$) integer n . The envelope is centered at the angular frequency ω_c, the mean angular frequency of the carrier waves. Eq. 3.39 maps therefore two radio frequencies ω_{rep} and ω_{ceo} onto an optical frequency ω. A frequency comb based on a Ti-sapphire femto second laser was built by a member of our laboratory Feng Zhu in his Master Thesis [56].

1. Optical frequency measurement

In the first step the beat note from the frequency comb light f_{opt} from dye laser is observed. Only a crude frequency selection is needed to pick out the tooth in the comb nearest in the frequency to the stabilized source. This mth tooth is at frequency $f_{ceo} + mf_{rep}$, so the beat frequency is:

$$f_{beat} = f_{ceo} + mf_{rep} - f_{opt}. \tag{3.40}$$

The repetition frequency f_{rep} depends on the cavity length and is in the radio frequency range (250MHz). The difference frequency f_{beat} will also be a microwave frequency, so that both f_{beat} and f_{rep} can be measured electronically. f_{ceo} is required before f_{opt} can be determined. It can be measured by producing the second harmonic

of the low frequency teeth and beating them against the not doubled high frequency teeth in on f to $2f$ interferometer. Suppose that the teeth involved are the nth and $2n$th, then this beat frequency is:

$$2(nf_{rep} + f_{ceo}) - (2nf_{rep} + f_{ceo}) = f_{ceo}, \tag{3.41}$$

which is also in the microwave range and can be measured electronically. Inserting the measured microwave frequencies: f_{beat}, f_{rep} and f_{ceo} into Eq. 3.40 gives the laser frequency f_{opt} of interest.

Spectral broadening due to self modulation via the intensity dependent index of refraction in an optical fiber is used to increase the width of the frequency comb. To achieve a stabilized frequency comb two free parameters, i.e. comb spacing and the comb offset have to be stabilized. To gain access to the carrier offset frequency of the FC1500 optical frequency synthesizer, the doubled frequency 2100nm part of the comb was employed, and a beat with the 1050nm part was observed (Fig. 29). This was implemented in a nonlinear interferometer with photonic crystal fiber used for generating the octave spanning spectrum. Both the repetition rate and the offset frequency were phase locked by controlling the cavity length and the pump power. The frequency comb was locked to GPS as shown in Fig. 30 and Fig. 31. For a detailed description on operating FC1500 reference is made to the manual [57].

2. Almost simultaneous measurements of parallel and antiparallel laser excited radiation

To reduce the influence of the ion source instability, we employ almost simultaneous measurements of parallel and antiparallel laser excited radiation. To implement almost simultaneous measurements of parallel and antiparallel laser excited radiation the gating scheme was constructed, shown in Fig. 32. The gating was realized by two

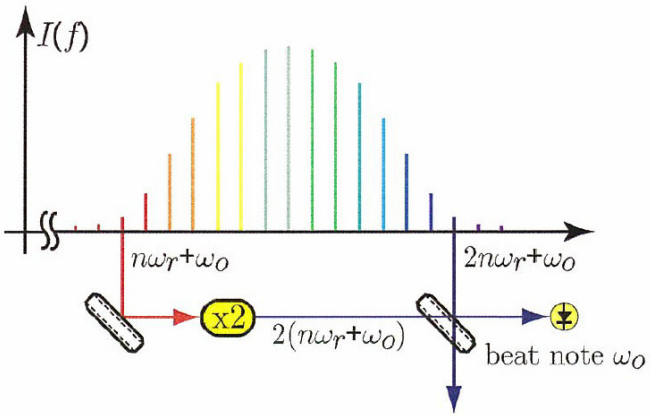

FIG. 29. The principle of the optical frequency synthesizer. The beat note between the frequency doubled mode and the mode at 2n yields the offset frequency.

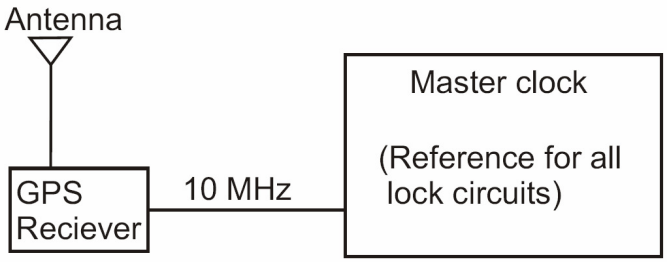

FIG. 30. Frequency comb locked to GPS signal.

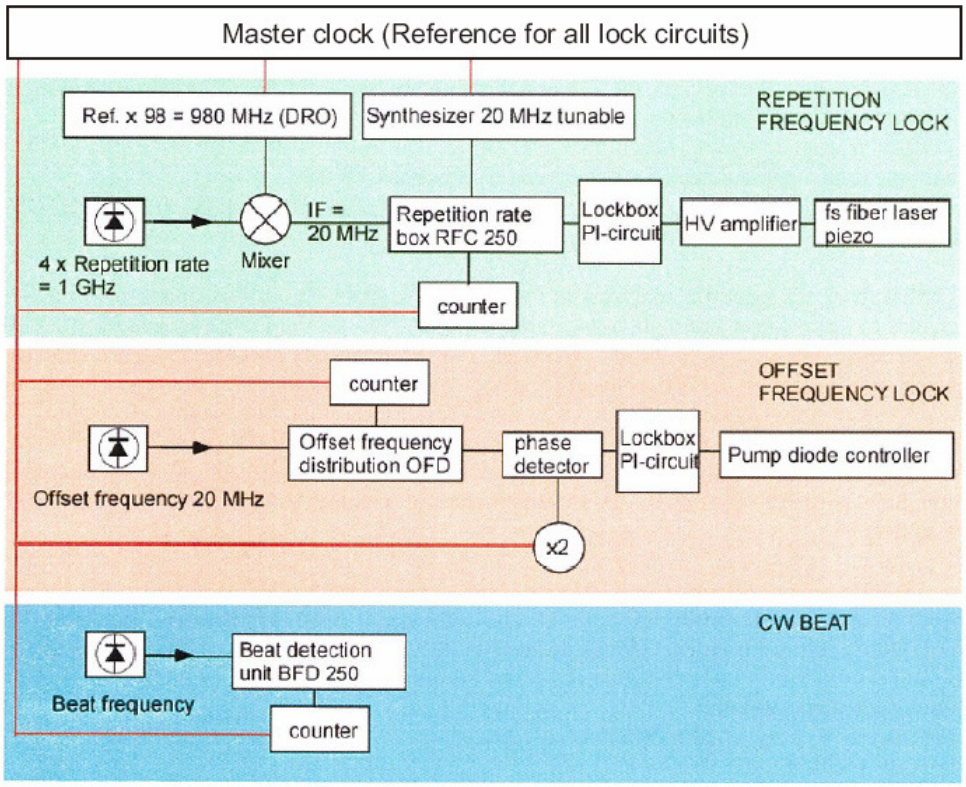

FIG. 31. Locking the frequency comb.

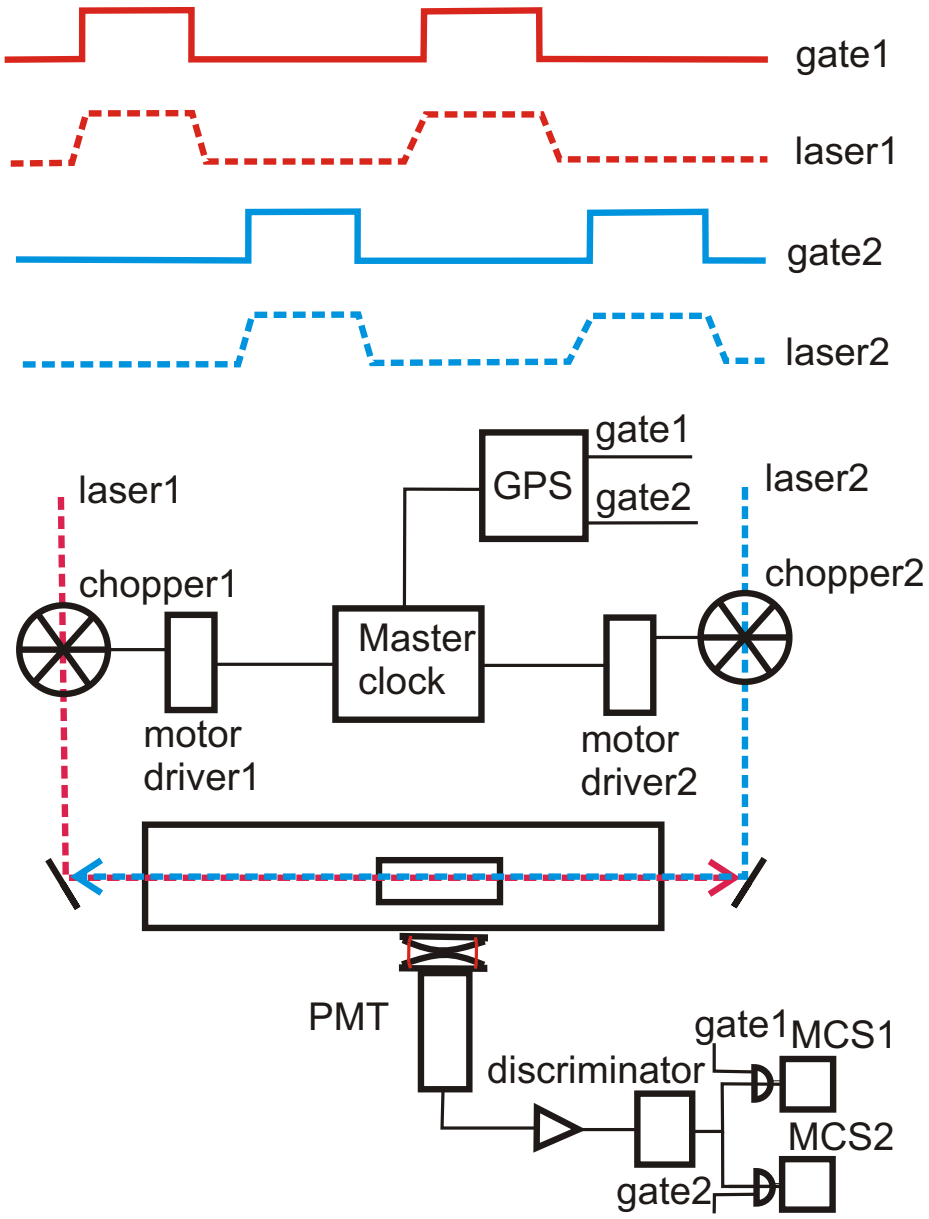

FIG. 32. Gating scheme for the almost simultaneous measurements of parallel and antiparallel laser excited radiation.

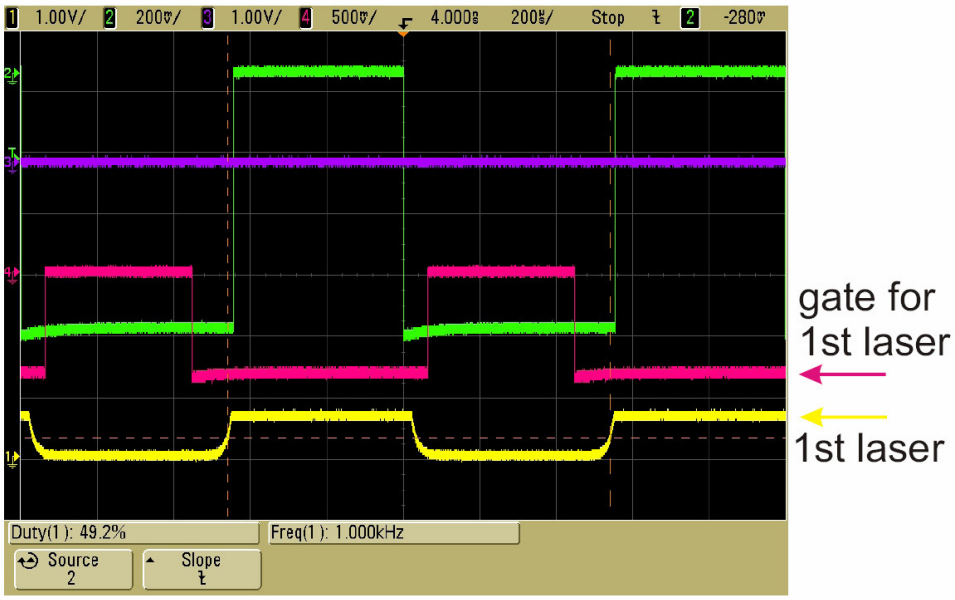

FIG. 33. Gating scheme for laser 1.

choppers with the full gate period equals 1/1kHz=1ms. The actual gating is shown in Fig. 33 for laser 1 and on Fig. 34 for laser 2.

To measure wavelength of the parallel and antiparallel laser excited radiation the frequency comb two beat signals need to be measured simultaneously by two different avalanche photodetectors. The beat signals were obtained from merging and interfering of two dye laser beams with the frequency comb radiation. Due to a slight, but sufficient difference (≈1.5nm) in the wavelength of two lasers, providing collinear (blue-shifted) and anticollinear (red-shifted) laser radiation, two beat signals can be detected independently by employing a grating. The corresponding setup was build and shown in Fig 35.

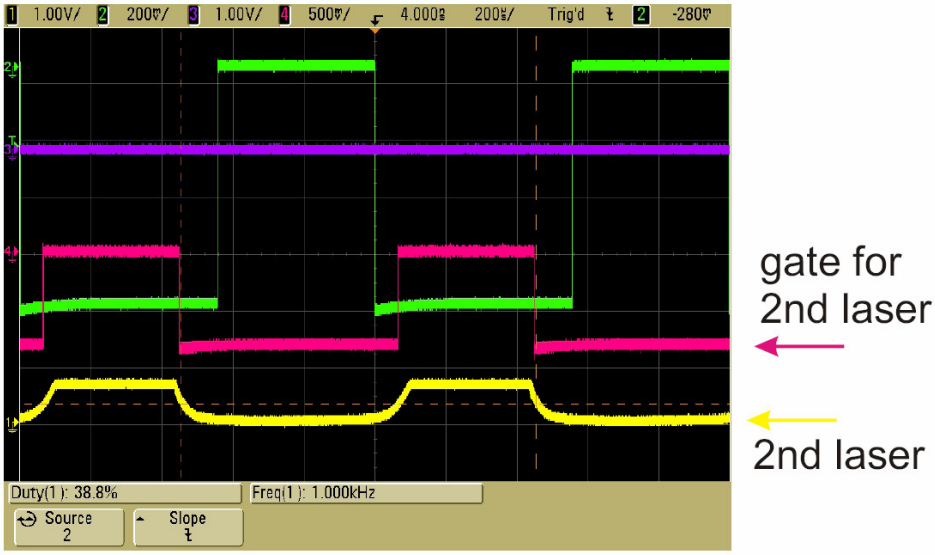

FIG. 34. Gating scheme for laser 2.

H. Optical signal recording

Emission and absorption of the light can be explained if light is considered as a stream of discrete particles, photons. Thus the measurement of light detection involves a discrete number of photons in a given interval of time. For the fluorescent light measurements the individual photons are independent. That means that the standard deviation is subject to Poisson statistics [58], yielding the best theoretical signal-to-noise ratio (SNR) as:

$$SNR = \sqrt{N} \tag{3.42}$$

where N is a number of photons reaching the detector in a given interval of time. For a given light intensity the number of photons is proportional to the detection time interval. As a result the signal-to-noise ratio (SNR) is decreasing with a decrease of the time interval of detection or another words with increasing the detection

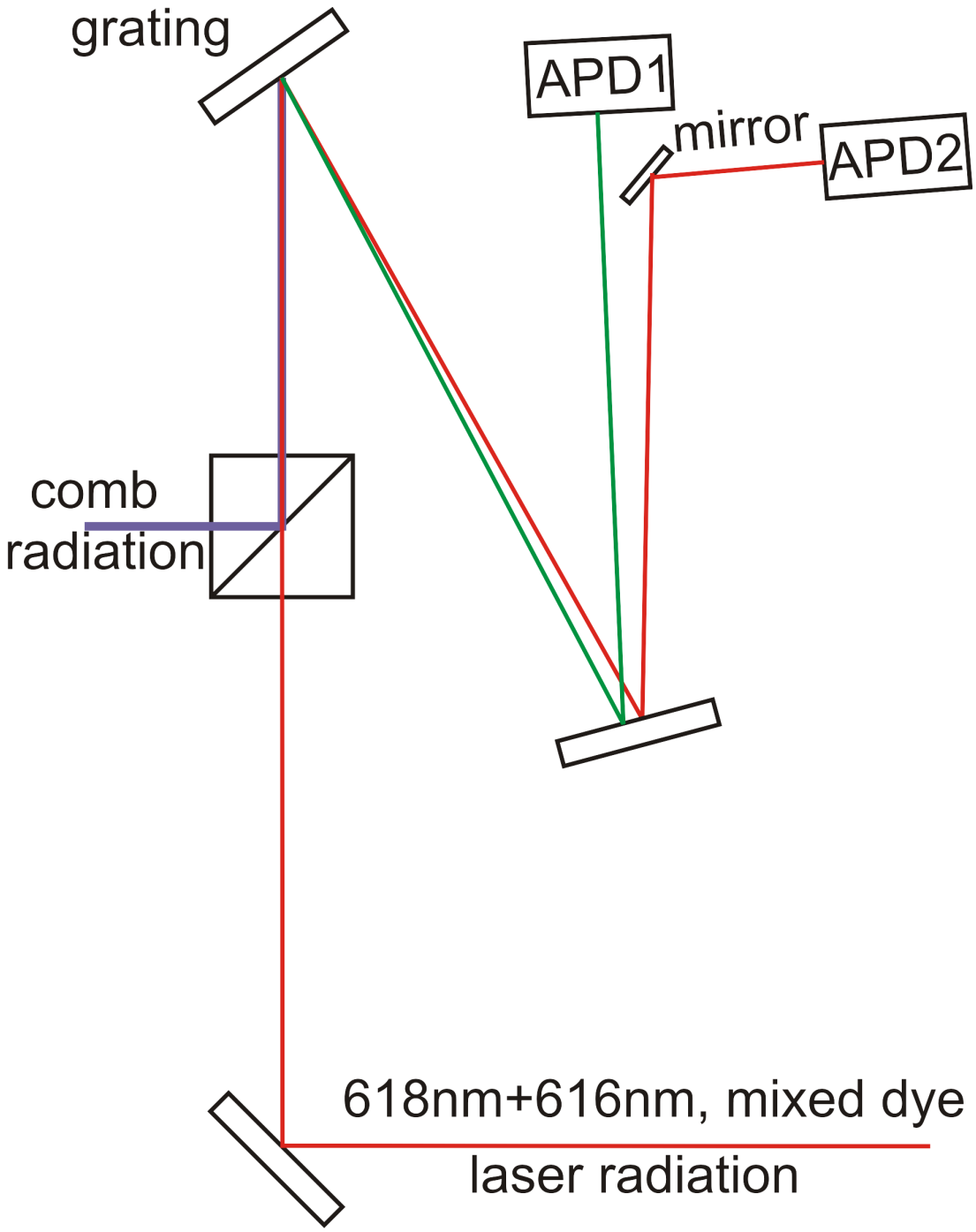

FIG. 35. Simultaneous measurements two beat frequencies by two different detectors.

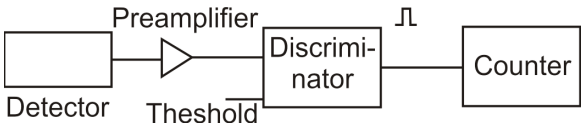

FIG. 36. Steady-state photon counting.

bandwidth. The output signal at high bandwidth is no longer a continuous signal. Instead it is a random sequence of pulses corresponding to individual photons. This situation is typical for our optical detectors which is a photomultiplier. At a high gain the single photons and the noise are difficult to distinguish, and the output signal becomes a random sequence of pulses.

The most efficient way to record a signal in the time domain is to record its intensity directly into large number of channels for a long time. The sample rate, i.e. the density of the signal points on the recorded data, must be higher than twice the frequency of the fastest signal component present in the signal. This relationship is know as the *Nyquist condition.* Only if the *Nyquist condition* is fulfilled, the signal parameters can be recovered without additional assumption about signal shape.

The simplest photon counter consist of a detector, a discriminator and a counter (Fig. 36). The discriminator receives single-photon pulses from the detector. The single-photon pulses have more or less random amplitude. There is a noise background consisting of low amplitude pulses from the detector, noise from environment, and electrical noise from electronic circuit. The discriminator has an adjustable threshold, which is set to discriminate the single-photon pulses against the background noise. The discriminator threshold is set above the noise level, but below the peak amplitude of the photon pulses delivered by the detector. When a single-photon pulse exceeds the selected threshold, the discriminator delivers a pulse of defined duration and

defined logic level. The discriminator output pulses are counted by the subsequent counter. The photons are acquired for a settled time interval, after which the result is read from counter.

CHAPTER IV

EXPERIMENTAL DATA FOR AR II

In our first fluorescence measurement the ArII line of the transition between the metastable $^2G_{9/2}$ state (154181.4942cm^{-1}) and the excited $^2F^o_{7/2}$ state (170-530.4041cm^{-1}) was chosen as test candidate for excitation. For fluorescence decay the transition between $^2F^o_{7/2}$ and $^2D_{5/2}$ (148842.4674cm^{-1}) states was observed. The metastable states are produced in fraction of 2×10^{-6} [59, 60] in ion source and we pump the optical transitions from metastable states into excitation states from where they decay into the ground state at 461.0858nm. Thus the pumping lines and fluorescence line are well separated in the wavelength and laser scattering light can be effectively suppressed using two filters each having transmission around 40% at fluorescence wavelength plus interference filter and blue cut filter with transmission around 80% each.

A. Ar II level scheme

Argon (Greek $\alpha\rho\gamma o\varsigma$ meaning "inactive") was suspected to be present in air by Henry Cavendish in 1785, but was not discovered until 1894 by Lord Rayleigh and Sir William Ramsay in an experiment in which they removed all of the oxygen and nitrogen from the air. Argon was also encountered in 1882 through independent research of H. F. Newall and W. N. Hartley. Each observed new lines in the color spectrum of air, but were unable to identify the element responsible for the lines. Argon became the first member of the noble gases to be discovered.

The singly charged ion of the nobel gas Ar has 18 protons in the nucleus, and three stable isotopes Ar^{36}, Ar^{38}, Ar^{40}. The natural isotopic composition is given in Table VII. The 17 electrons forming the electron shells have the following electronic

TABLE VII. The natural isotopic composition of Ar.

Isotope	**Atomic mass**	**Natural abundance**	**Nuclear spin**	**Magnetic moment**
	m_a/u	$atom\%$	I	μ/μ_N
^{36}Ar	35.96754552(29)	0.3365(30)	0	0
^{38}Ar	37.9627325(9)	0.0632(5)	0	0
^{40}Ar	39.9623837(14)	99.6003(30)	0	0

configuration at ground state:

$$1s^2 2s^2 2p^6 3s^2 3p^5 (^2P^o_{3/2}), \tag{4.1}$$

and ionization potential 222 848.2cm^{-1} (27.630 eV) [61]. Fig. 37 displays the transition of interest. The resonance line investigated is the transition between the metastable $^2G_{9/2}$ state (154181.4942cm^{-1}) and the excited $^2F^o_{7/2}$ state (170-530.4041cm^{-1}). The fluorescence observed as the signal is mainly between $^2F^o_{7/2}$ and $^2D_{5/2}$ (148842.4674cm^{-1}) states. The long lifetime of the metastable state [62] makes it possible for the ions to travel from the ion source to the interaction chamber where they are excited. The levels were chosen so that their transitions fall in the range of visible light where dye laser light can be used for excitation. The resonance wavelength is 611.6616nm in vacuum. The fluorescent light occurs at wavelength 461.0858nm and 468.3587nm in vacuum which is far from that of the resonance, thus it can be effectively separated from the scattered light of the laser by using filters. The summary of excitation lines is presented in Table VIII. The decay lines and their energy levels are summarized in Table IX. The lifetime of the metastable state (^{2}G$_{7/2}$ τ=6.10s, ^{2}G$_{9/2}$ τ=4.90s) [62] is longer than the flight time $\approx 1 \times 10^{-5}$ sec of

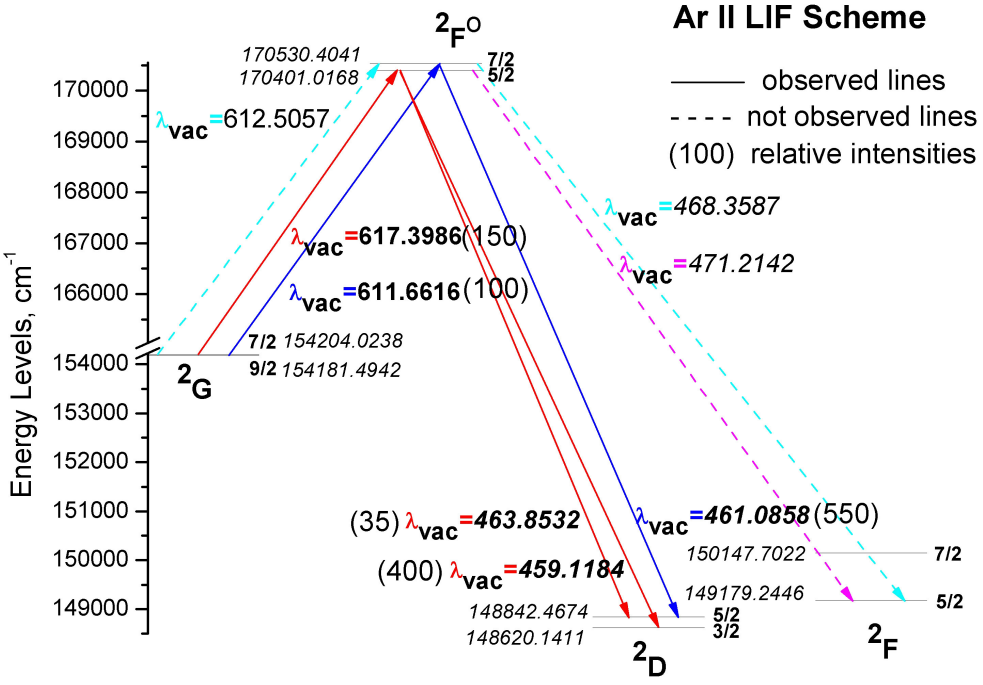

FIG. 37. Ar II laser induced fluorescence (LIF) scheme.

TABLE VIII. Ar II excitation lines.

	State	**Energy**	**Line**
		cm^{-1}	nm
initial	$^2G_{9/2}$	154181.4942	611.6616
final	$^2F^o_{7/2}$	170530.4041	
initial	$^2G_{7/2}$	154204.0238	617.3986
final	$^2F^o_{5/2}$	170401.0168	

TABLE IX. Ar II decay lines.

	State	**Energy**	**Line**
		cm^{-1}	nm
initial	$^2\mathrm{F}^o_{7/2}$	170530.4041	461.0858
final	$^2\mathrm{D}_{5/2}$	148842.4647	
initial	$^2\mathrm{F}^o_{7/2}$	170530.4041	468.3587
final	$^2\mathrm{F}_{5/2}$	149179.2446	
initial	$^2\mathrm{F}^o_{5/2}$	170530.4041	463.8532
final	$^2\mathrm{D}_{5/2}$	148842.4647	
initial	$^2\mathrm{F}^o_{5/2}$	170530.4041	459.1184
final	$^2\mathrm{D}_{3/2}$	148620.1411	
initial	$^2\mathrm{F}^o_{5/2}$	170530.4041	471.2142
final	$^2\mathrm{F}_{5/2}$	149179.2446	

the metastable ions from the ion source to the interaction region, and much longer that that of the upper state so that it has negligible effect on the natural line width. The lifetime of the level $^2F^o_{7/2}$ of ArII is known to be $\tau = 8.414 \pm 0.025$ns [19]. The natural width was found to be 3.18 MHz according to $\Delta\nu = 1/2\pi\tau$. This natural line width limits the resolution.

The metastable state $3d^2G_{9/2}$, some 34 eV above the ground state of the argon neutral atom is populated [60, 63, 64] primarily by a single ionization events with energetic electrons:

$$Ar + e \rightarrow Ar^{+*} + 2e, \tag{4.2}$$

since the metastable state density has been found to be directly proportional to the discharge current.

B. Sensitivity estimate

The laser excitation fluorescent detection method for the Ar II signal (611nm, 617nm) takes advantage of the fact that the laser excitation is in red spectral region, while the fluorescence detection occurs in the blue spectral region (464nm, 461nm, 459nm). It is assumed that each ion emits only one signal photon. The Rabi oscillations of several subsequent absorptions and emissions by the same ion are possible, depending on the laser power, but emission photons of Rabi oscilllation will not be observed as they occur on the same wavelength as that of exciting laser light. As the signal fluorescence occurs from a long-lived metastable state and not from the ground state, we estimated that only about 0.02% of ions in the ion beam can participate in the detection scheme. The sensitivity depends on the strength of the optical transition, as well as the ratio between the natural and reduced Doppler width.

The theoretical value of the detection sensitivity β is given as the product of the

emission probability ϵ_E, the detection probability ϵ_N, the fraction of the metastable state α, the geometrical overlap ϵ_O and the spectral overlap ϵ_ν:

$$\beta = \alpha \cdot \epsilon_E \cdot \epsilon_N \cdot \epsilon_O \cdot \epsilon_\nu. \tag{4.3}$$

We use $\alpha = 0.0002$, and $\epsilon_E = 1$, $\epsilon_O = 1$ since the laser beam is wider than the ion beam so all ions interacting with laser radiation. The other parameters in Eq. 4.3 given by:

$$\epsilon_\nu = \frac{\delta\nu_{nat}}{\delta\nu_{obs}} = \frac{3.18}{102} = 0.03, \tag{4.4}$$

$$\epsilon_N = \eta\Omega\delta = 0.2 \times 0.085 \times 0.1436 = 0.00244, \tag{4.5}$$

where ν_{nat}=3.18MHz and $\delta\nu_{obs}$=102MHz are the natural width and observed signal linewidth respectively, η=0.2 is the quantum efficiency of the photomultiplier, Ω=1.07/4π=0.085 is the collection efficiency related to the solid angle of observation and δ=0.8×0.469×0.454 ×0.843=0.1436 is the combined transmission of the four filters (SPF-500= interference filter, Hoya B390, Hoya B440, Hoya Y44). Therefore the expected detection efficiency is:

$$\beta = 0.0002 \times 1 \times 0.00244 \times 1 \times 0.03 = 1.5 \times 10^{-8}. \tag{4.6}$$

The minimum number of ions required for observing a signal can be derived using expected value of β and the dark current count rate from Burle 8850 N=80cps. If we require that the minimum detectable signal should have a signal-to-noise ratio of:

$$\frac{S}{N} = 2, \tag{4.7}$$

then the signal count rate follows as:

$$S = 160. \tag{4.8}$$

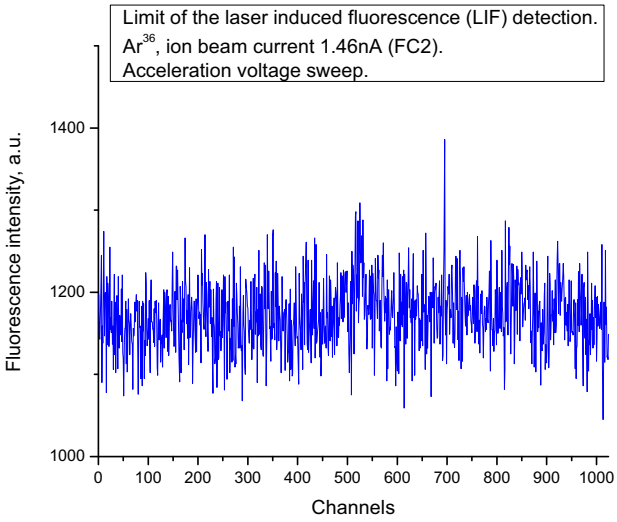

FIG. 38. Laser induced fluorescence (LIF) detection limit.

The minimum number is

$$n_{min} = \frac{S}{\beta} = \frac{160}{1.5 \times 10^{-8}} \approx 1 \times 10^{10} \text{ ions/sec}, \tag{4.9}$$

which corresponds to a minimum ion beam current:

$$I_{min} = 1 \times 10^{10} \cdot 1.6 \times 10^{-19} = 1.6 \times 10^{-9} = 1.6\text{nA}. \tag{4.10}$$

Typically we had 1.46nA at Faraday cup (FC2) for mass separated Ar^{36} which was the limit for our detection (Fig. 38). However, we did not use Hoya Y44 filter at that time, which changes the theoretical minimum ion beam current to the value 1.35nA. The population of the metastable state could be different, depending on the ion source operation condition and our 0.02% is only rough estimate.

C. Data acquisition

Data acquisition was carried out in two ways: either by scanning the laser frequency through resonance at a constant acceleration voltage or by scanning postacceleration volatge at a fixed laser frequency. The scanning voltage method has more sensitivity, which was shown by the detection of Ar^{36} laser induced fluorescence (Fig. 38), however the scanning frequency of the laser has more accuracy, as we employed the frequency comb for measuring the exact laser frequency radiation.

D. Laser frequency scanning

1. Iodine calibration

a. Iodine absorption lines

The absorption spectrum of the iodine molecule I_2 is widely used as the reference for determing the absolute value of the laser frequency. The iodine atoms have large atomic weight and the chemical bond between the two iodine atoms in the molecule is weak. As a result, the vibrational frequency of the iodine molecule is small, so the gaps between the vibrational levels are small. The weak chemical bonds result in a large distance between atoms in molecule. Combined with the large mass of the atoms it produces a high moment of inertia. Therefore the gap between rotational energy is small as well. These factors cause a huge number of vibrational and rotational sublevels of the ground electronic state to be populated at room temperature. In turn it results in many absorption lines that span the major part of visible spectrum . The iodine absorption spectrum consists of thousands of lines from several to dozen GHz apart.

b. Doppler-free absorption spectroscopy

Each of the iodine absorption line is in fact a group of narrow spaced hyperfine absorption lines. The natural linewidth of the hyperfine lines are of the order of a few MHz. However, due to Doppler broadening, groups of these lines are overlapped. To observed these hyperfine lines, one has to employ Doppler-free technique for spectroscopy. For iodine calibration the most popular method is the *saturation spectroscopy* [65, 66]. Saturation spectroscopy is based on a simple principle: each molecular (or atomic) optical transition can only absorb (scatter) a limited number of photons per second. When a limited number of molecules (atoms) are exposed to the incoming photon flux, they can only remove photons from that flux at a fixed rate. Once that rate is reached, any increase in the photon flux will not be absorbed. Therefore the relative attenuation of the light passing through an absorbing medium will decrease as the the light intensity is increased. This effect is called *saturation* of the absorption. It can be used to target only molecules that are not moving in the direction of the laser beam and therefore not exhibiting a Doppler shift. To achieve this technique, two beams are sent through the cell filled with iodine vapor. The beams of the same frequency are overlapped and are traveling along the same line in opposite direction. One of the beams is usually much stronger than the other, it is called the *pump beam*. The weaker beam is called the *probe beam* and its transmission is monitored. A molecule that has velocity v_z in the direction of the pump beam will *see* the pump beam as having frequency $\nu_{\mathrm{L}}(1 - v_z/c)$, where ν_{L} is the laser frequency. A molecule will *see* the probe beam as having frequency $\nu_{\mathrm{L}}(1 + v_z/c)$, according to the Doppler shift relation 2.9 with $v_z \ll c$. Thus only the molecule with $v_z = 0$ will see two beams at the same frequency. If that frequency coincides with one of the absorption frequencies of the molecule, the transmission of the probe beam will

increase due to saturation effect. An example of the iodine saturation signal (green line) is presented in Fig. 40. The setup used for iodine saturation spectroscopy is shown in Fig. 27. The iodine saturation setup was build in our Texas A&M Stored Ion Laboratory by Dr. Vladimir Ryjkov [67] and independently by Dr. Takamine [54] in RIKEN Atomic Physics Laboratory.

2. Laser frequency measurements with frequency comb

The signals from fluorescence for collinear and anticollinear measurements were recorded in Channel D and Channel C, respectively. The corresponding laser scanning voltages were recorded in Channel A for collinear and Channel B for anticollinear. An example of the recorded data are shown in Fig. 39.

The ultimate goal of the iodine calibration procedure for the recorded data is to find the absolute frequency of the laser radiation. To enhance the precision of the laser frequency measurements the frequency comb was employed and related procedure for extracting beat frequency was developed. The first step was to calibrate integer number n related with the comb tooth number 3.40 using the iodine spectra as a marker, as well as to relate the corresponding n in the frequency domain in the vicinity of the resonance (Fig. 40). Once we know n from iodine spectra, it's possible to determine the sign (plus or minus) of the offset of the frequency comb. The next step in the procedure is to determine the beat frequency. For that reason the custom beat frequency fitting function was introduced. The parameters of the function are determined by the repetition rate. It has the form of the saw teeth and presented

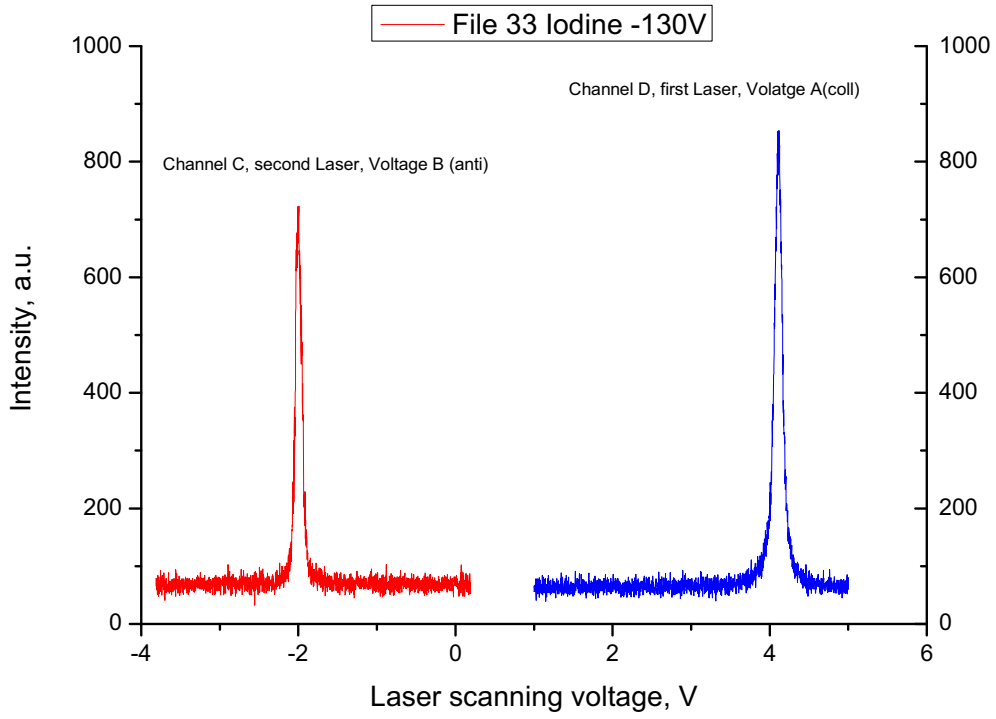

FIG. 39. Simultaneous data recording for collinear (voltage channel A, fluorescence channel D) and anticollinear (voltage channel B, fluorescence channel C) measurements.

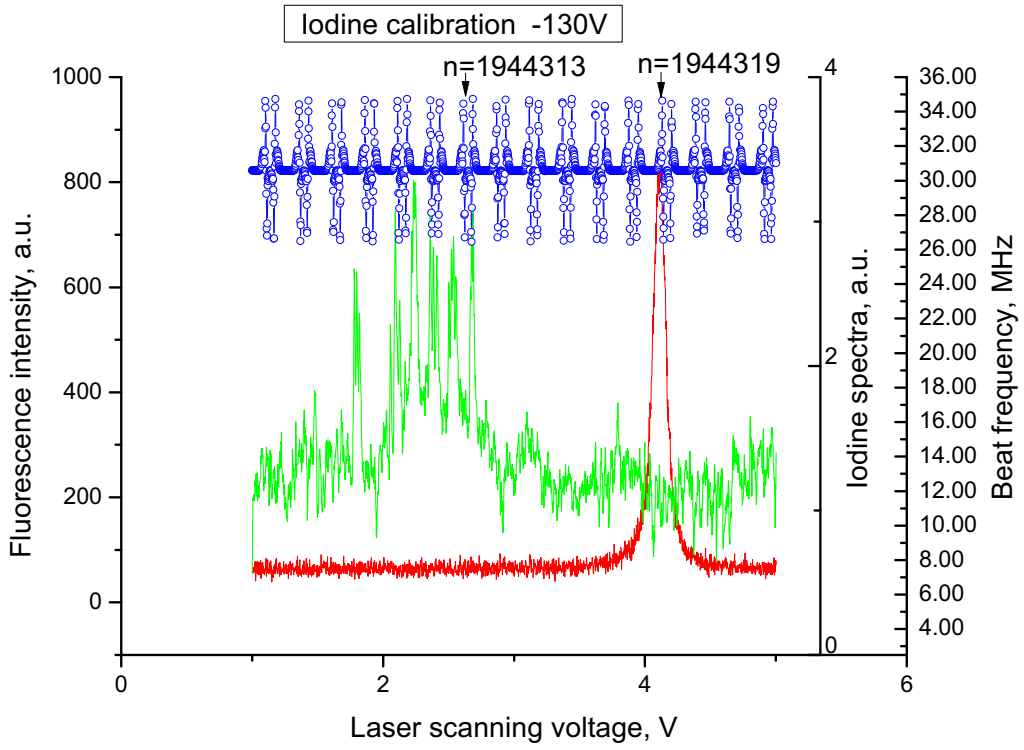

FIG. 40. Calibration procedure to determine the n-th comb mode near the resonance from the iodine spectra.

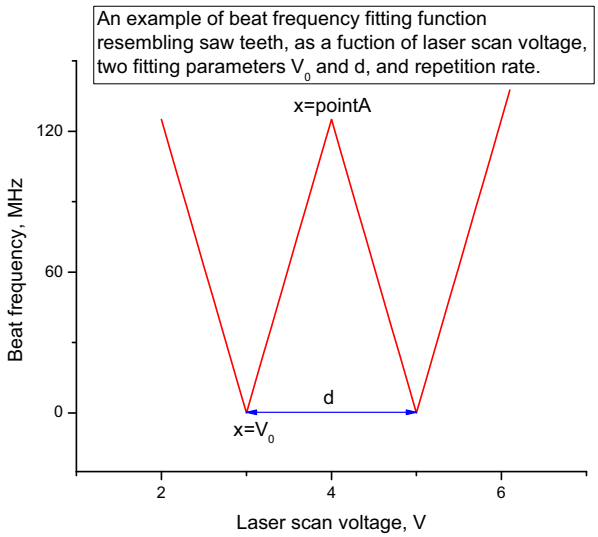

FIG. 41. An example of the beat fitting function model.

in Fig. 42. The analytical expression of the function is given by:

$$y(x) = \begin{cases} -\frac{fr}{d}(x - V_0), & \text{if } V_0 < x; \\ \frac{fr}{d}(x - V_0), & \text{if } V_0 < x < \text{pointA}; \\ -\frac{fr}{d}\left(x - (V_0 + d)\right), & \text{if pointA} < x < (V_0 + d); \\ \frac{fr}{d}\left(x - (V_0 + d)\right), & \text{if } x > (V_0 + d), \end{cases} \tag{4.11}$$

where fr=(reprate+980MHz)/4, V_0 is the starting point of one of the beat, d is the full period between two beats in laser scanning voltage domain, and point A is a point somewhere in the middle between two beats in laser scanning voltage domain. The implementation of the code of the beat fitting function in Origin C is presented in Fig. 42.

The electronics associated with avalanche photodetector, which is recording the beat frequency has two frequency windows for recording: one has a pass filter around

```
//-----------------------------------------------------------
//
void _nlsffreqdom2_p_c_mod(
// Fit Parameter(s):
double V0, double d,
// Independent Variable(s):
double x,
// Dependent Variable(s):
double& y)
{
    // Beginning of editable part
        double fr=0;
        double reprate=20000108;
        double pointA=4.05; // point in the middle between two beats
        fr=(reprate+980E6)/4;
          if(x<V0)
          {y=-fr/d*(x-V0);}
        if (x>V0 && x<pointA)
          {y=fr/d*(x-V0);}
        if(x>pointA && x<(V0+d))
          {y=-fr/d*(x-(V0+d));}
        if(x>(V0+d))
          {y=fr/d*(x-(V0+d));}


    // End of editable part
}
```

FIG. 42. Origin C code for fitting function for beat frequency.

20MHz for signal from laser 1, and the another one has a pass filter around 30MHz for signal from laser 2. This way the corresponding data for the proper frequency window must be selected from the beat frequency data file. For example, on Fig. 43 for collinear measurements the recording window for the beat frequency was around 30MHz, thus only data points representing the linear dependence with positive and negative slope within the frequency window 30MHz were selected for data fitting analysis in Fig. 44. From the fit it was possible to determine initial starting voltage V_0 and the distance d between two consecutive beats. These parameters allow to convert laser scanning voltage domain into the frequency domain by the formula:

$$\boxed{\text{Laser Frequency} = \left(\frac{\text{rep.rate}+980\text{MHz}}{4}\right)\left(n + \frac{x - V_0}{d}\right) \pm 2 \times \text{offset},} \qquad (4.12)$$

where $\pm$ sign was determined from iodine spectra and offset value was 20MHz.

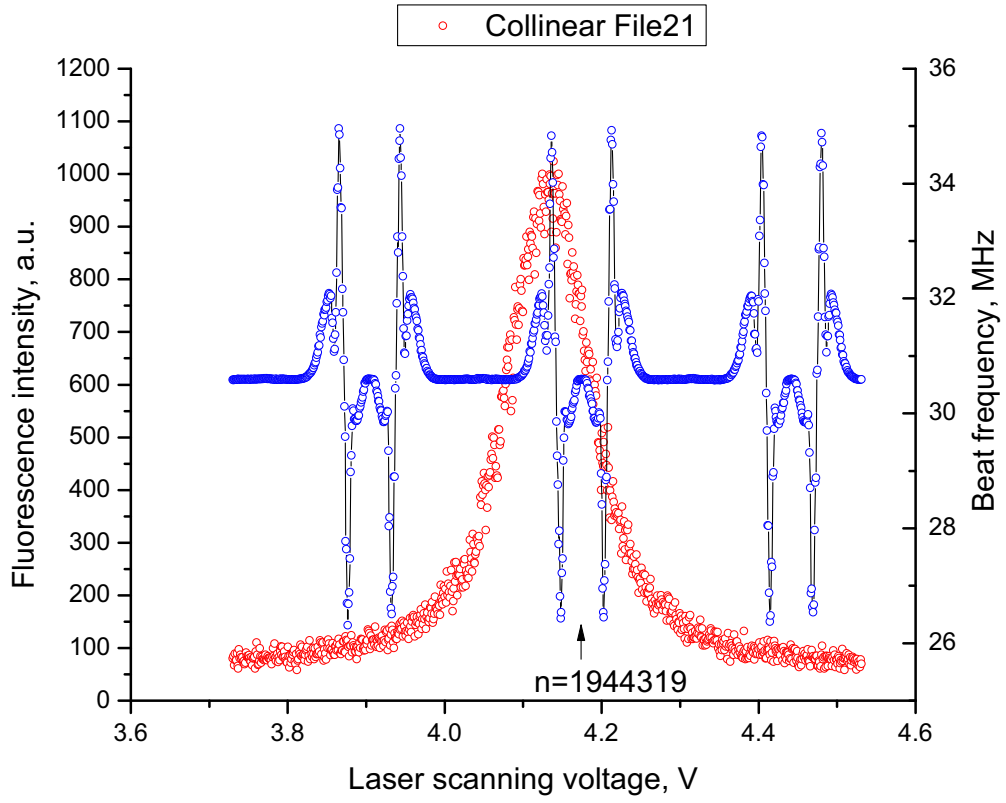

FIG. 43. Fluorescence signal for collinear measurements with respect to the beat frequency.

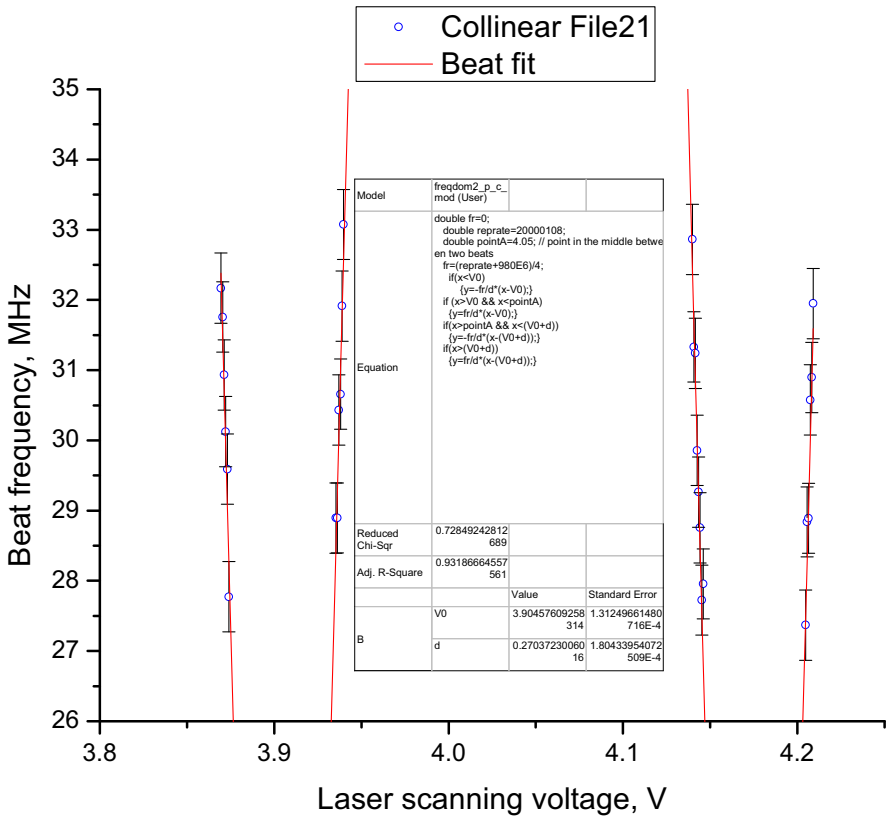

FIG. 44. Fitting beat frequency data in linear function model.

3. Line shape analysis and fitting procedure

An accurate line shape analysis is subject to different contributions such as collisions with residual gas, the Dopller effect, divergence of the beam, crossing angle between the laser beam and the ion beam, as well as inhomogeneity of the electric field in the post-acceleration cage. Usually Gaussian and Lorentzian models are well described and employed in the fitting procedure of the inhomogeneously and homogeneously broadened resonance line shape. The asymmetry of the line shape was tested with custom built asymmetric Gaussian and asymmetric Lorentzian models. Gaussian function with exponential tails model was also constructed, which could take into account the asymmetry of the wings of the line profile. Several Origin Pro 8.0 built-in function were tested as well to determine the best fitting model. Some of them, such as LogNorm function could test the asymmetry of the line shape. The main fitting function was Voigt function for the following reasons. The velocity distribution of the ions in the ion beam is described by a Gaussian (Maxwellian), while the absorption/fluorescence profile of a transition of any of those ions is described by Lorentzian. Thus the absorption/fluorescence line shape of an ensemble of ions in the ion beam is a sum of all the individual ions' profile, which is in general neither Lorentzian nor Gaissian, but a convolution of both, described by Voigt model. In total eight different models were used to fit the resonance curve. Five of them were Origin Pro 8.0 built-in functions.

a. Gauss model

The Gauss model represents inhomogeneous broadening, such as Doppler effect. We tested two different definitions of the Gauss function, which give different normalization and hence different values for the linewidth parameter w. One have

to be careful extracting and comparing parameters from different fitted curves to pay attention to the definition of the linewidth parameter w in particular model. For example, essentially the same Gaussian models: standard Gauss function and amplitude Gauss function give different values for linewidth parameter w for the same data fit. In our case, the former was 0.101 and the latter was 0.051. Converting linewidth parameter w to a full width at half maximum (FWHM) parameter would avoid possible confusion. The standard Gauss function model is presented in Fig. 45 and tested in Fig. 46. The amplitude Gauss model is shown in Fig. 48 and fitted in Fig. 48.

b. Lorentz model

Lorentz model represents homogeneous broadening, such as natural linewidth or saturation broadening. The Lorentz model is presented in Fig. 49 and tested in Fig. 50.

c. Voigt model

The Voigt model is deduced as an averaging procedure of the intensity distribution for an assembly of ions in the ion beam over the velocity distribution of the ions in the ion beam. The Voigt model is presented in Fig. 51 and tested in Fig. 52.

d. LogNormal model

The LogNormal function is build-in Origin Pro 8.0 function which carries an asymmetry, and can be tested to fit asymmetric function. The model is presented in Fig. 53 and fitted in Fig. 54.

Gauss

Function

$$y = y_0 + \frac{A}{w\sqrt{\pi / 2}} e^{-2\frac{(x-x_c)^2}{w^2}}$$

Brief Description

Area version of Gaussian function.

Sample Curve

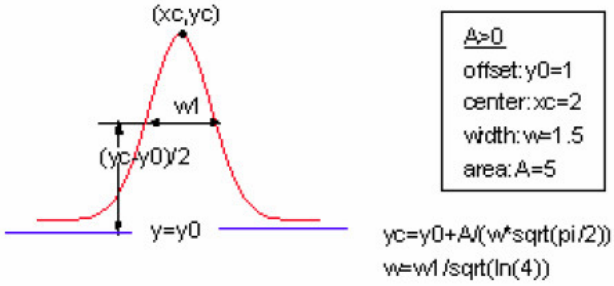

Parameters

Number: 4

Names: y0, xc, w, A

Meanings: y0 = offset, xc = center, w = width, A = area

Initial Values: y0 = 0.0 (vary), xc = 0.0 (vary), w = 1.0 (vary), A = 10 (vary)

Lower Bounds: w > 0.0

Upper Bounds: none

FIG. 45. Gauss model.

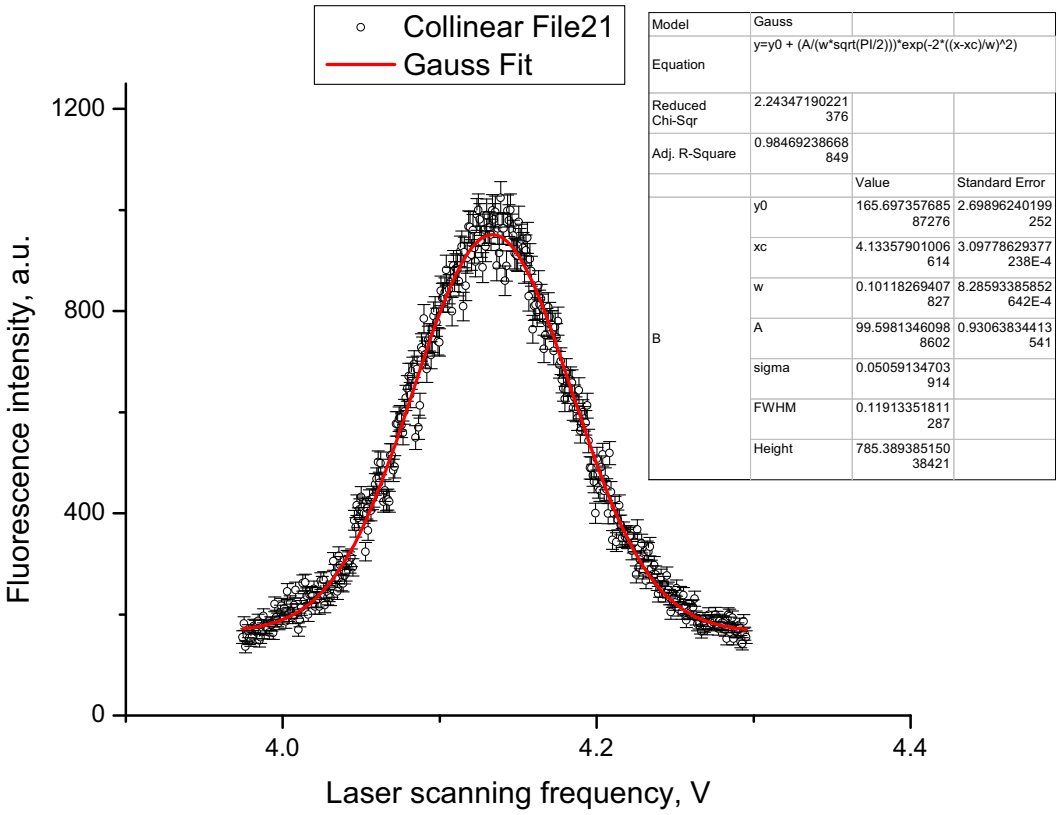

Model	Gauss		
Equation	y=y0 + (A/(w*sqrt(PI/2)))*exp(-2*((x-xc)/w)^2)		
Reduced Chi-Sqr	2.24347190221376		
Adj. R-Square	0.98469238668849		
		Value	Standard Error
B	y0	165.69735768587276	2.69896240199252
	xc	4.13357901006614	3.09778629377238E-4
	w	0.10118269407827	8.28593385852642E-4
	A	99.59813460988602	0.93063834413541
	sigma	0.05059134703914	
	FWHM	0.11913351811287	
	Height	785.38938515038421	

FIG. 46. Gauss model fit.

GaussAmp

Function

$$y = y_0 + Ae^{\frac{(x-x_c)^2}{2w^2}}$$

Brief Description

Amplitude version of Gaussian peak function.

Sample Curve

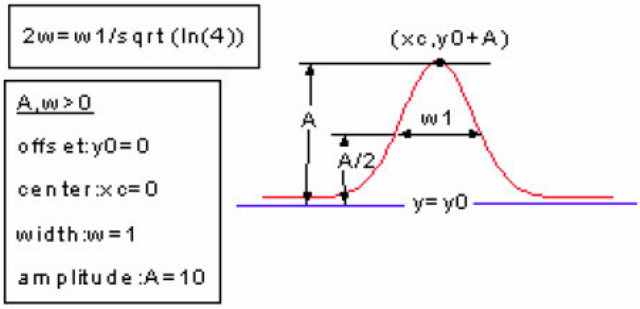

Parameters

Number: 4

Names: y0, xc, w, A

Meanings: y0 = offset, xc = center, w = width, A = area

Initial Values: y0 = 0.0 (vary), xc = 0.0 (vary), w = 1.0 (vary), A = 10 (vary)

Lower Bounds: w > 0.0

Upper Bounds: none

FIG. 47. Gauss amplitude model.

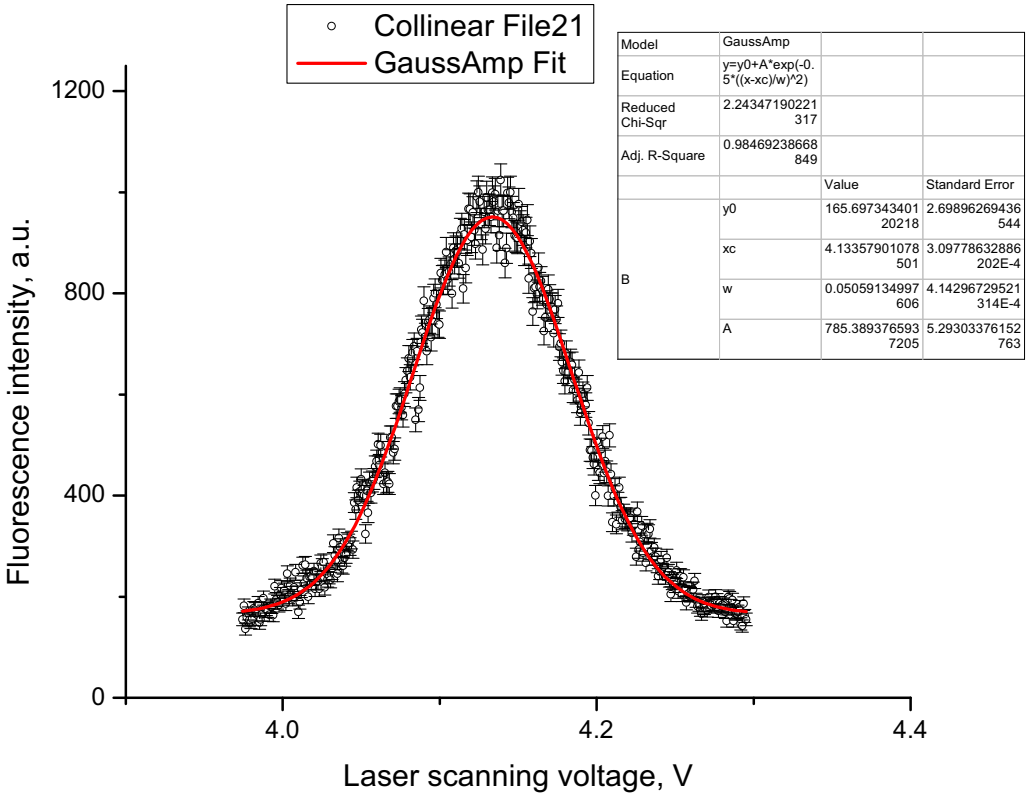

FIG. 48. Gauss amplitude model fit.

Lorentz

Function

$$y = y_0 + \frac{2A}{\pi}\frac{w}{4(x - x_c)^2 + w^2}$$

Brief Description

Lorentzian peak function.

Sample Curve

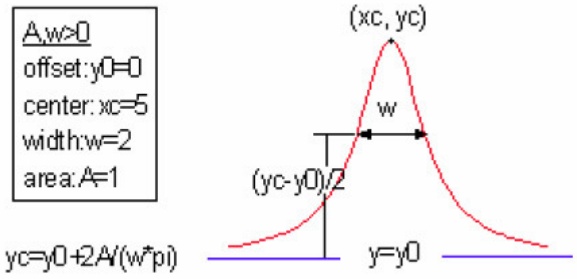

Parameters

Number: 4

Names: y0, xc, w, A

Meanings: y0 = offset, xc = center, w = width, A = area

Initial Values: y0 = 0.0 (vary), xc = 0.0 (vary),w = 1.0 (vary), A = 1.0 (vary)

Lower Bounds: w > 0.0

Upper Bounds: none

FIG. 49. Lorentz model.

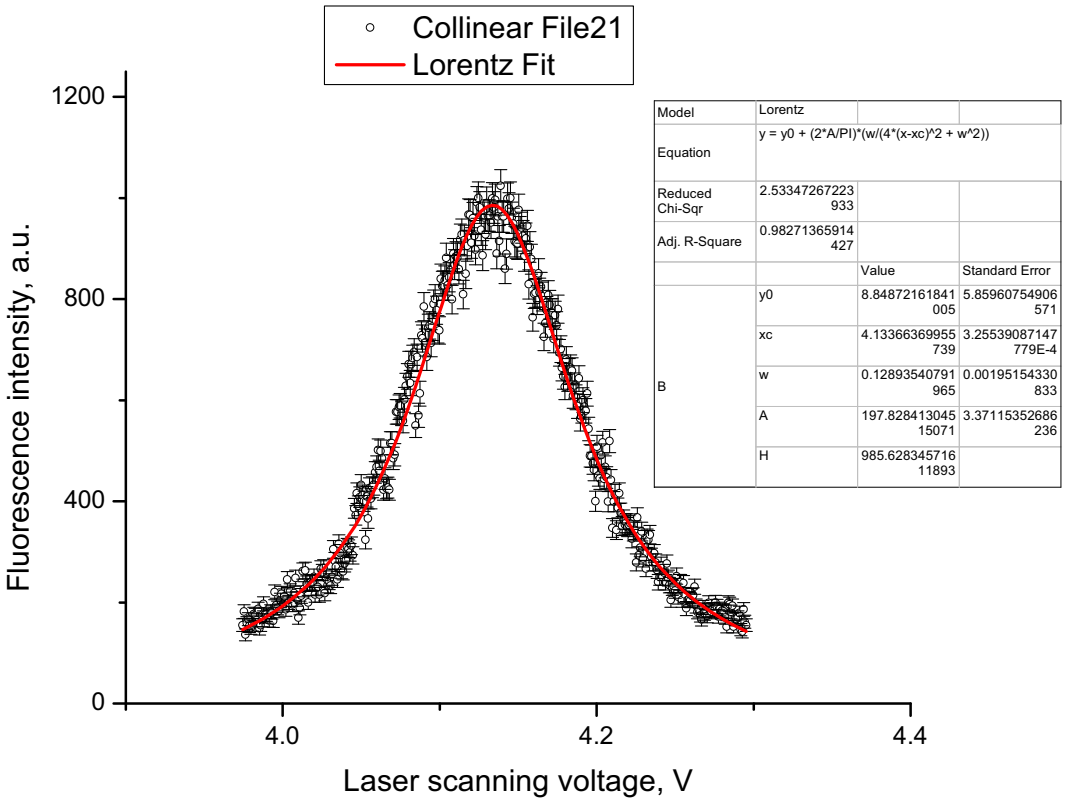

Model	Lorentz		
Equation	y = y0 + (2*A/PI)*(w/(4*(x-xc)^2 + w^2))		
Reduced Chi-Sqr	2.53347267223933		
Adj. R-Square	0.98271365914427		
		Value	Standard Error
B	y0	8.84872161841005	5.85960754906571
	xc	4.13366369955739	3.25539087147779E-4
	w	0.12893540791965	0.00195154330833
	A	197.82841304515071	3.37115352686236
	H	985.62834571611893	

FIG. 50. Lorentz model fit.

Voigt

Function

$$y = y_0 + A \cdot \frac{2\ln 2}{\pi^{3/2}} \frac{w_L}{w_G^2} \cdot \int_{-\infty}^{\infty} \frac{e^{-t^2}}{\left(\sqrt{\ln 2}\,\frac{w_L}{w_G}\right)^2 + \left(\sqrt{4\ln 2}\,\frac{x - x_c}{w_G} - t\right)^2} dt$$

Brief Description

Voigt peak function.

Sample Curve

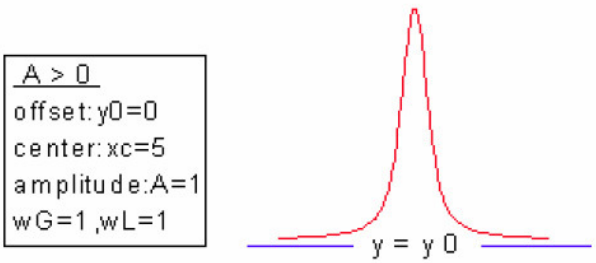

Parameters

Number: 5

Names: y0, xc, A, wG, wL

Meanings: y0 = offset, xc = center, A = amplitude, wG = Gaussian width, wL = Lorentzian width

Initial Values: y0 = 0.0 (vary), xc = 0.0 (vary), A = 1.0 (vary), wG = 1.0 (vary), wL = 1.0 (vary)

Lower Bounds: wG > 0.0, wL > 0.0

Upper Bounds: none

FIG. 51. Voigt model.

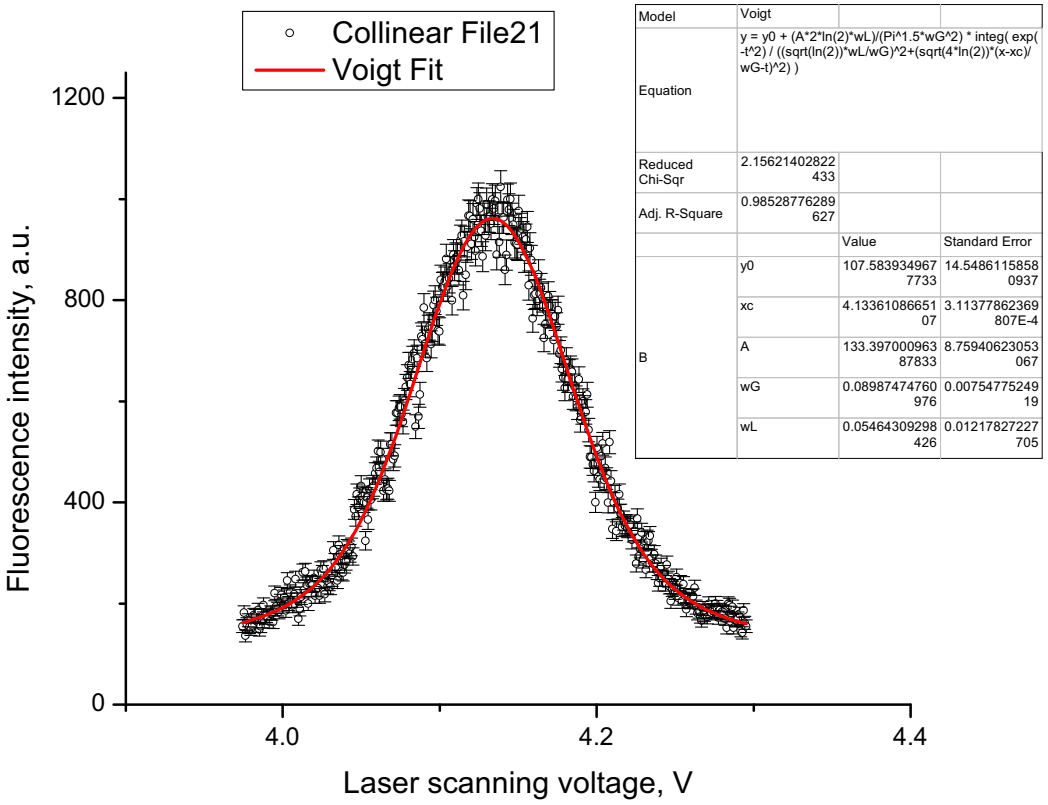

Model	Voigt		
Equation	y = y0 + (A*2*ln(2)*wL)/(Pi^1.5*wG^2) * integ(exp(-t^2) / ((sqrt(ln(2))*wL/wG)^2+(sqrt(4*ln(2))*(x-xc)/ wG-t)^2))		
Reduced Chi-Sqr	2.15621402822433		
Adj. R-Square	0.98528776289627		
		Value	Standard Error
B	y0	107.58393496777733	14.548611585880937
	xc	4.1336108665107	3.11377862369807E-4
	A	133.39700096387833	8.75940623053067
	wG	0.08987474760976	0.0075477524919
	wL	0.05464309298426	0.01217827227705

FIG. 52. Voigt model fit.

LogNormal

Function

$$y = y_0 + \frac{A}{\sqrt{2\pi}wx} e^{\frac{-[\ln x / x_c]^2}{2w^2}}$$

Brief Description

Log-Normal function.

Sample Curve

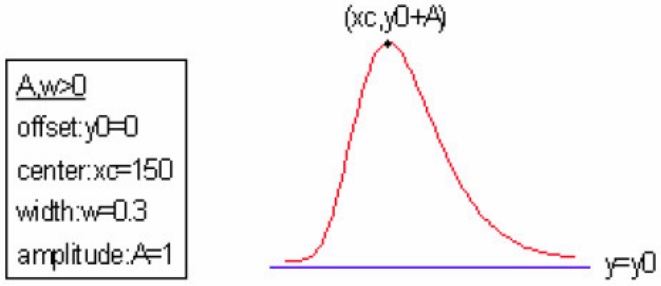

Parameters

Number: 4

Names: y0, xc, w, A

Meanings: y0 = offset, xc = center, w = width, A = amplitude

Initial Values: y0 = 0.0 (vary), xc = 1.0 (vary), w = 1.0 (vary), A = 1.0 (vary)

Lower Bounds: xc > 0, w > 0

Upper Bounds: none

FIG. 53. LogNormal model.

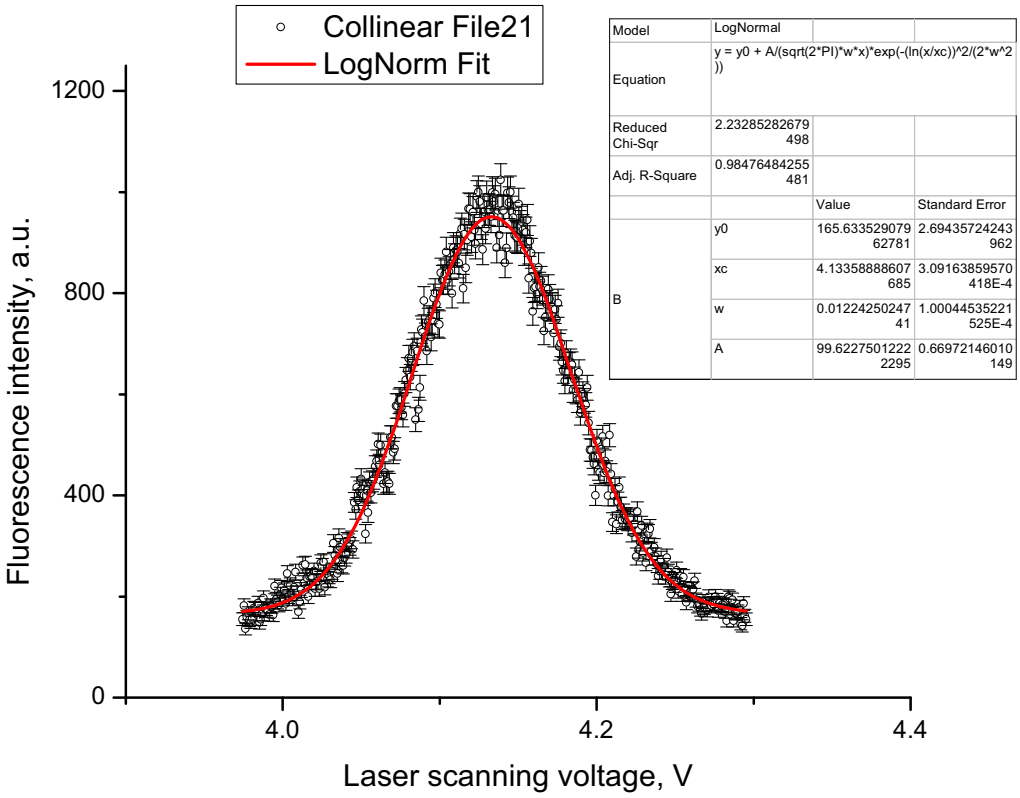

FIG. 54. LogNormal model fit.

e. Asymmetric functions: asymmetric Gauss, asymmetric Lorentz and Gaussian with exponential tails

Three custom functions were built, taking into account asymmetry of the peak. The first one was asymmetric Gaussian model, having analytical form:

$$y(x) = \begin{cases} y_0 + B \cdot e^{-\frac{(x-x_c)^2}{2\sigma_1^2}} & \text{if } x < x_c; \\ y_0 + B \cdot e^{-\frac{(x-x_c)^2}{2\sigma_2^2}} & \text{if } x > x_c, \end{cases} \tag{4.13}$$

where

$$B = \frac{A}{\frac{1}{2}\sqrt{2\pi}\,(\sigma_1 + \sigma_2)}, \tag{4.14}$$

and y_0, A, x_c, σ_1, σ_2 are parameters. Origin C code for that model is depicted on Fig. 55 and the data fitted by this function are shown in Fig. 56.

The second function was Gaussian with exponential tails model, which has analytical expression:

$$y(x) = \begin{cases} y_0 + A \cdot e^{-\frac{(P_1-x_c)^2}{2w^2} + \frac{(P_1-x_c)\cdot P_1}{w^2}} \cdot e^{-\frac{(P_1-x_c)\cdot x}{w^2}}, & \text{if } x < P_1; \\ y_0 + A \cdot e^{-\frac{(x-x_c)^2}{2w^2}} & \text{if } P_1 < x < P_2; \\ y_0 + A \cdot e^{-\frac{(P_2-x_c)^2}{2w^2} + \frac{(P_2-x_c)\cdot P_2}{w^2}} \cdot e^{-\frac{(P_2-x_c)\cdot x}{w^2}}, & \text{if } x > P_2; \end{cases} \tag{4.15}$$

where y_0, A, w, x_c, P_1, P_2, are parameters. The code in Origin C for this function is shown in Fig. 57 and the fitting procedure presented in Fig. 58.

The last function was asymmetric Lorentzian model, described by

$$y(x) = \begin{cases} y_0 + \frac{h}{1+\lambda_l^2\cdot(x-x_c)^2}, & \text{if } x \le x_c; \\ y_0 + \frac{h}{1+\lambda_r^2\cdot(x-x_c)^2}, & \text{if } x > x_c, \end{cases} \tag{4.16}$$

where y_0, h, x_c, λ_l, λ_r are parameters. The code in Origin C of such function is presented in Fig. 59 and the fitted line profile shape with this model is shown in

```
//-----------------------------------------------------------
//
void _nlsfAsymmetricGaussian(
// Fit Parameter(s):
double y0, double A, double xc, double sig1, double sig2,
// Independent Variable(s):
double x,
// Dependent Variable(s):
double& y)
{
    // Beginning of editable part
    double B;
    B=A/(0.5*(sig1+sig2)*sqrt(2*3.14));
     if(x<xc)
       {
     y=y0+B*exp(-0.5*(x-xc)*(x-xc)/(sig1*sig1));
       }
     else
      {
        y=y0+B*exp(-0.5*(x-xc)*(x-xc)/(sig2*sig2));
      }


    // End of editable part
}
```

FIG. 55. Asymmetric Gaussian model.

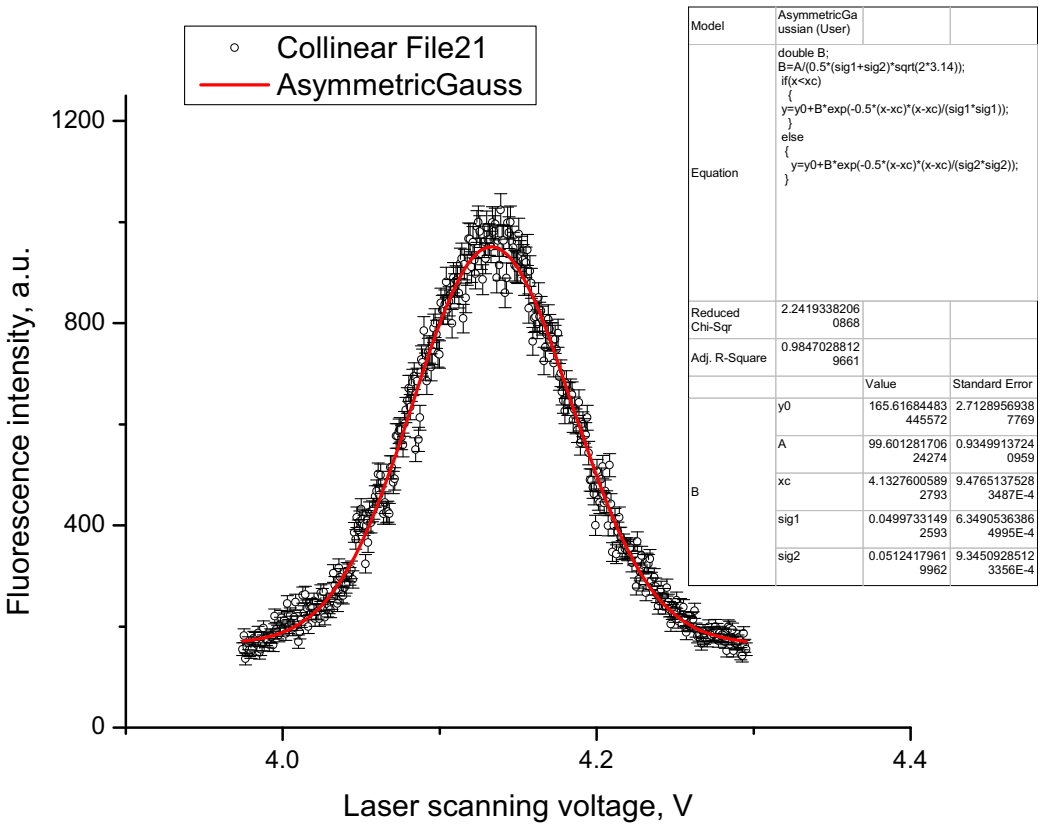

Model	AsymmetricGaussian (User)		

Equation	double B;
	B=A/(0.5*(sig1+sig2)*sqrt(2*3.14));
	if(x<xc)
	{
	y=y0+B*exp(-0.5*(x-xc)*(x-xc)/(sig1*sig1));
	}
	else
	{
	y=y0+B*exp(-0.5*(x-xc)*(x-xc)/(sig2*sig2));
	}		

Reduced Chi-Sqr	2.24193382060868		
Adj. R-Square	0.98470288129661		
		Value	Standard Error
B	y0	165.61684483445572	2.71289569387769
	A	99.60128170624274	0.93499137240959
	xc	4.13276005892793	9.4765137528 3487E-4
	sig1	0.04997331492593	6.3490536386 4995E-4
	sig2	0.05124179619962	9.3450928512 3356E-4

FIG. 56. Asymmetric Gaussian model fit.

```
//-----------------------------------------------------------
//
void _nlsfGauss_Exponent(
// Fit Parameter(s):
double y0, double A, double w, double xc, double P1, double P2,
// Independent Variable(s):
double x,
// Dependent Variable(s):
double& y)
{
    // Beginning of editable part
    if(x<P1)
    {y=y0+A*exp(-(P1-xc)*(P1-xc)/(2*w*w)+(P1-xc)*(P1)/(w*w))*exp(-(P1-xc)*x/(w*w));}
    else if (x<P2)
    {y=y0+A*exp(-(x-xc)*(x-xc)/(2*w*w));}
         else
         {y=y0+A*exp(-(P2-xc)*(P2-xc)/(2*w*w)+(P2-xc)*(P2)/(w*w))*exp(-(P2-xc)*x/(w*w));}


    // End of editable part
}
```

FIG. 57. Gaussian with exponential tails model.

Fig. 60.

The recorded data for collinear measurement (File21) were fitted to all models, the resulting centers of the peak of the resonance were fitted (Fig. 61) to *constant* model to see the discrepancy between different models. The center of the peak, the uncertainty, and the characteristic parameter of the each individual fit called *reduced* χ^2 were compiled in Table 61. The best results were achieved with Voigt profile function as the reduced χ^2 is the smallest for Voigt model fitting procedure.

4. Voltage drift, pressure drift and the necessity for simultaneous measurements in collinear and anticollinear geometry

There is an acceleration voltage fluctuations during the single resonance scan Fig 62, as well as a trend of an acceleration voltage with long time scale Fig. 63. To compensate the acceleration voltage fluctuations software feedback PID loop was

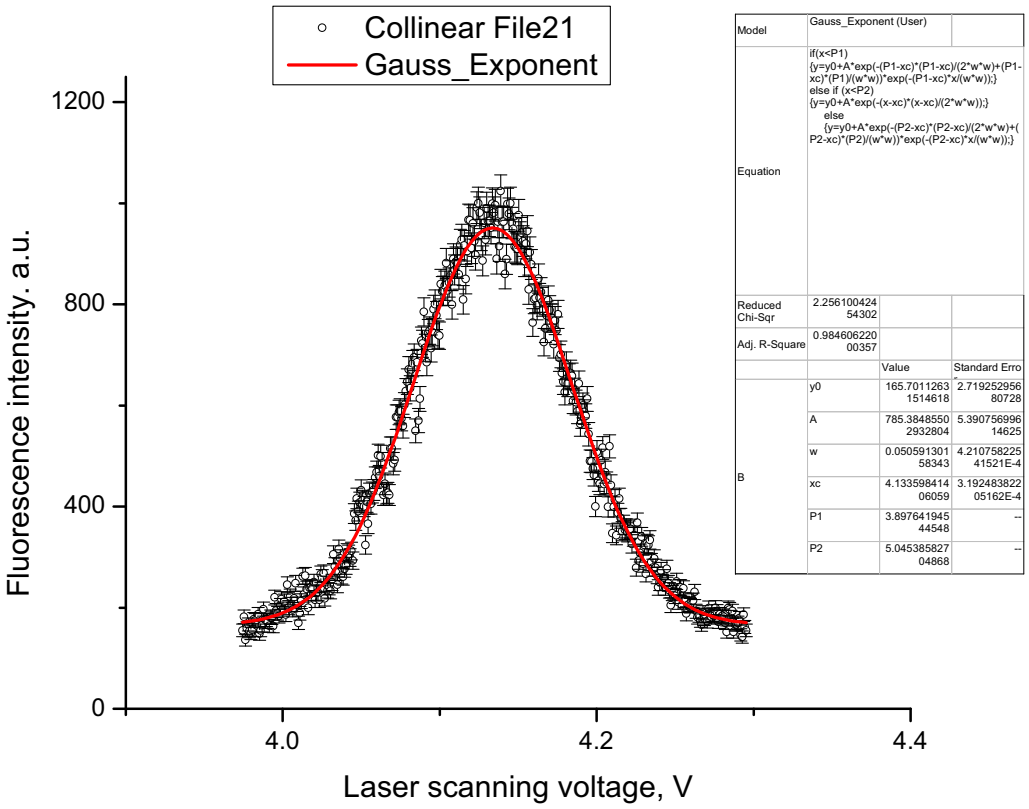

FIG. 58. Gaussian with exponential tails model fit.

```
//-----------------------------------------------------------
//
void _nlsfAsymmetricLorentz(
// Fit Parameter(s):
double y0, double h, double xc, double lyambda_l, double lyambda_r,
// Independent Variable(s):
double x,
// Dependent Variable(s):
double& y)
{
    // Beginning of editable part
    if (x<=xc)
      y=y0+h/(1+lyambda_l*lyambda_l*(x-xc)*(x-xc));
      else
      y=y0+h/(1+lyambda_r*lyambda_r*(x-xc)*(x-xc));


    // End of editable part
}
```

FIG. 59. Asymmetric Lorentzian model.

TABLE X. Comparison between eight fitting models.

Model	x_c**'s last digit, MHz**	**Uncertainty, kHz**	χ^2
Gauss	5.0	286.8	2.24347
GaussAmp	5.0	286.8	2.24347
GaussAsym	4.3	877.4	2.24193
GaussExp	5.0	295.6	2.25610
LogNorm	5.0	286.2	2.23285
LorentzAsym	4.8	748.2	2.53321
Lorentz	5.1	301.4	2.53347
Voigt	5.0	288.3	2.15621

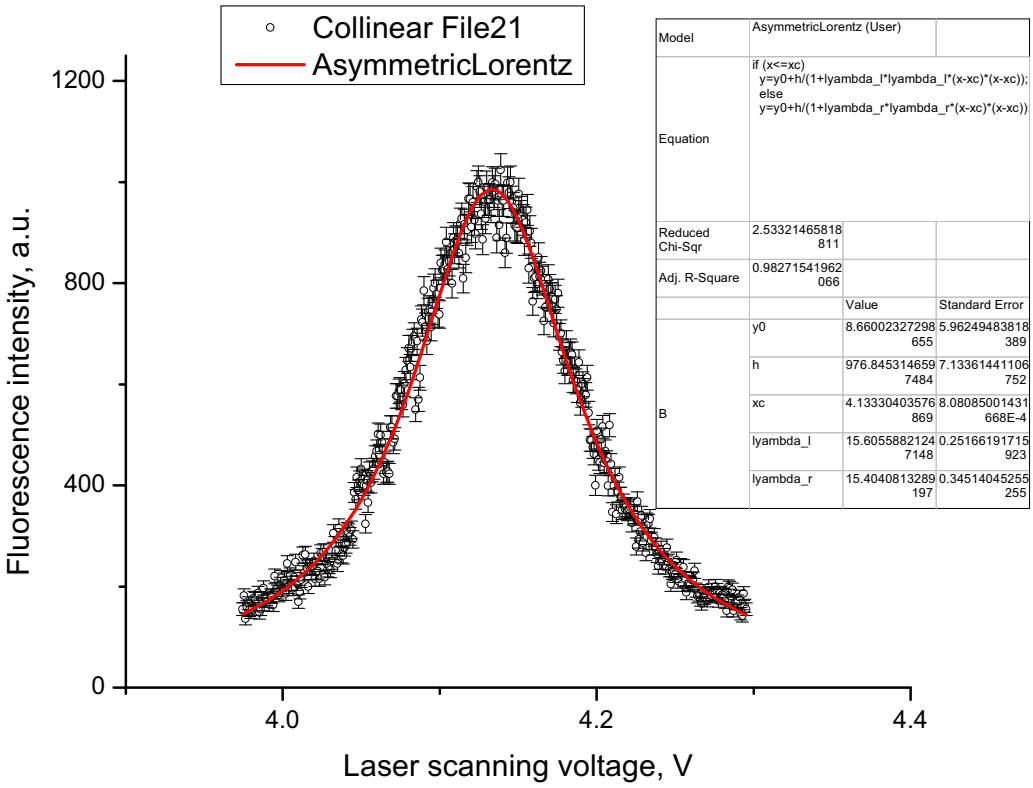

FIG. 60. Asymmetric Lorentzian model fit.

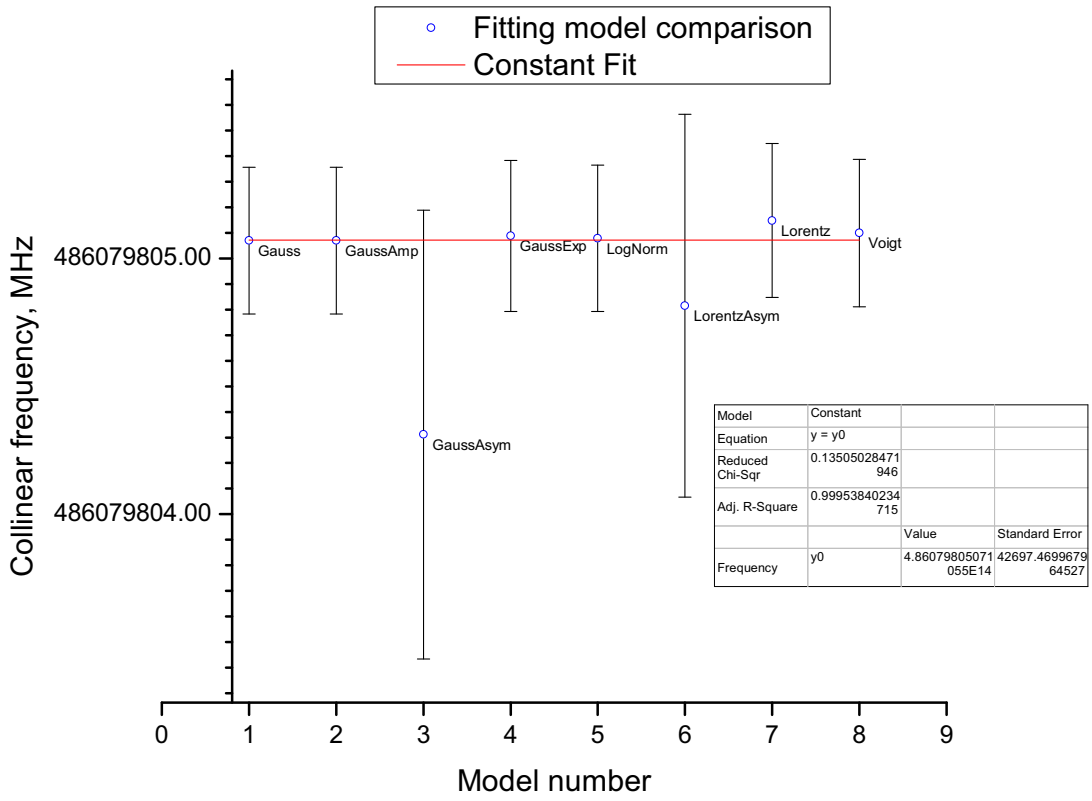

FIG. 61. Fitting model comparison.

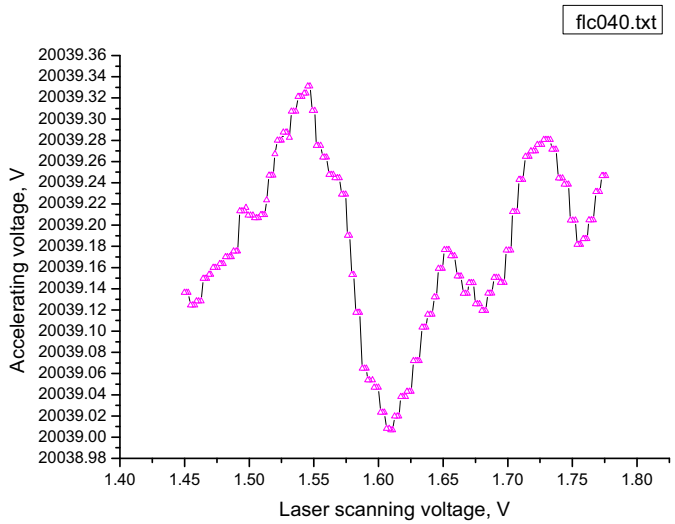

FIG. 62. Acceleration voltage fluctuation during one single resonance scan.

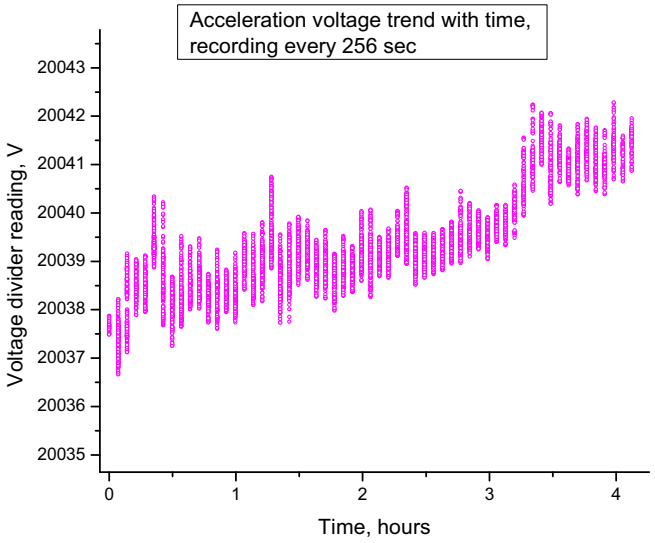

FIG. 63. Acceleration voltage fluctuation trend during longer times.

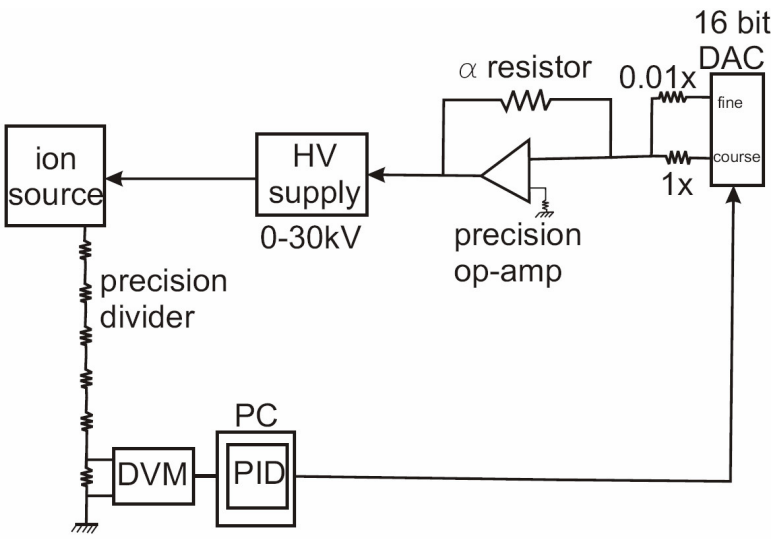

FIG. 64. Circuit diagram of the feedback loop to compensate the acceleration voltage fluctuations.

proposed. The schematic of the feed back loop is depicted in Fig. 64. The implementation of the software PID feedback loop allowed to stabilize acceleration voltage within uncertainty less then 0.1 V, which corresponds 1.35MHz in the frequency domain of the transition of interest. There is a dependence of the position of the center of the resonance line on the anode voltage in the in source as it shown in Fig. 65. Each peak corresponds to the different anode voltage in the ion source, and it clearly affects on the position of the center of the fluorescence curve. The ion source was in *constant current* operation mode and the corresponding ion source anode current and anode voltage with respect to the file number are presented in Tab. XI. To reduce further the acceleration voltage fluctuations the operation mode of the ion source was switched from *constant current* mode to *constant voltage* mode. The resulting resonance curves are presented in Fig. 66 for collinear and in Fig. 67 for anticollinear measurements. The shift from measurement (file) to measurement

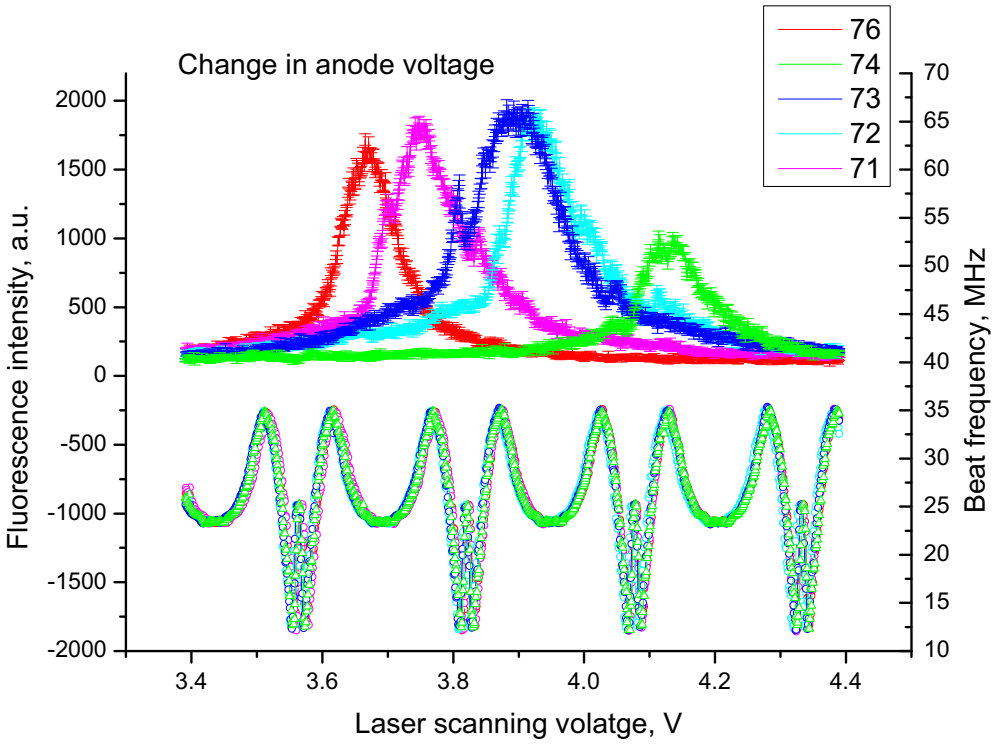

FIG. 65. Changes in anode voltage cause a change in the position of the resonance peak.

TABLE XI. Change in anode voltage of the ion source operation parameters.

File number	**I, anode current**	**V, anode voltage**
	A	*V*
71	60	130
72	65	142-136.2
74	70	168.6-156.5
76	55	120.9-127

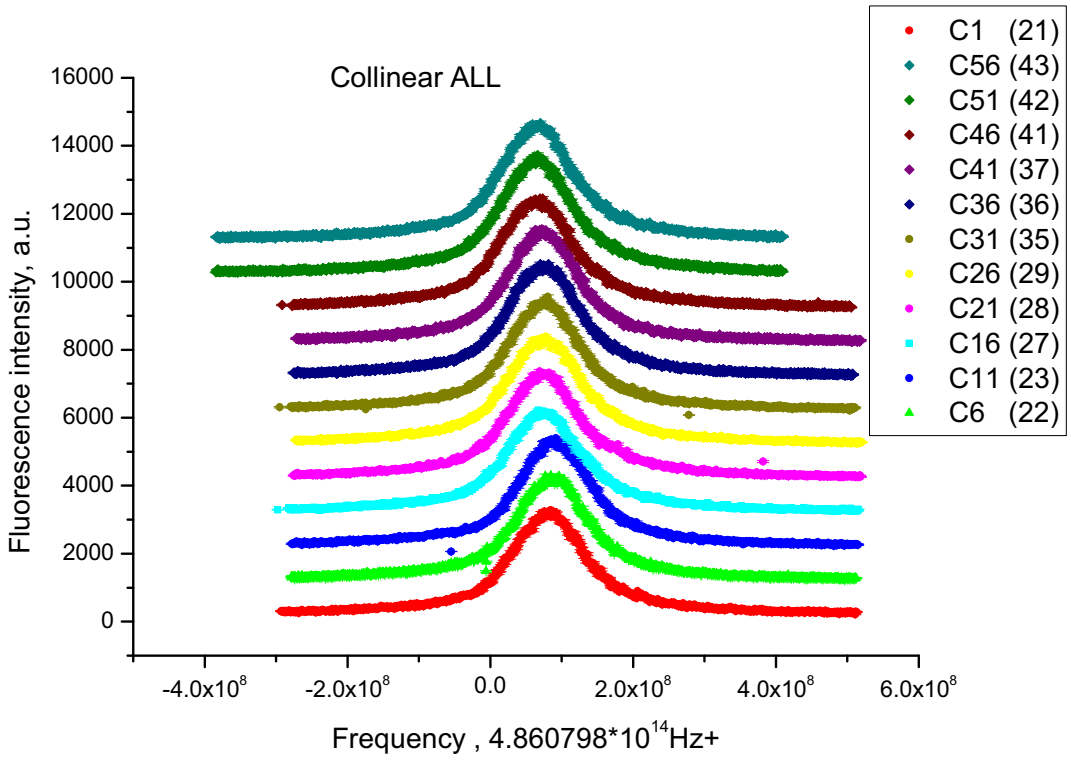

FIG. 66. Operating the anode voltage in constant voltage mode. Collinear geometry scan.

(file) in the position of the peak of the resonance line was reduced. Still, one can visually observe noticeable fluctuations in the position of the peak of the fluorescence curve. The remaining instabilities could be related to the pressure drift inside the ion source. To test this hypothesis the pressure inside of the ion source was recorded as a function of time and at different time the collinear (blue points on the curve) and anticollinear (red points on the curve) measurements were taken. The pressure drift is presented in Fig. 68 along with collinear and anticollinear measurements in Fig. 69. To establish the dependence of the resonance center line from the feeding Ar gas pressure in the ion source, the data on the collinear measurements were

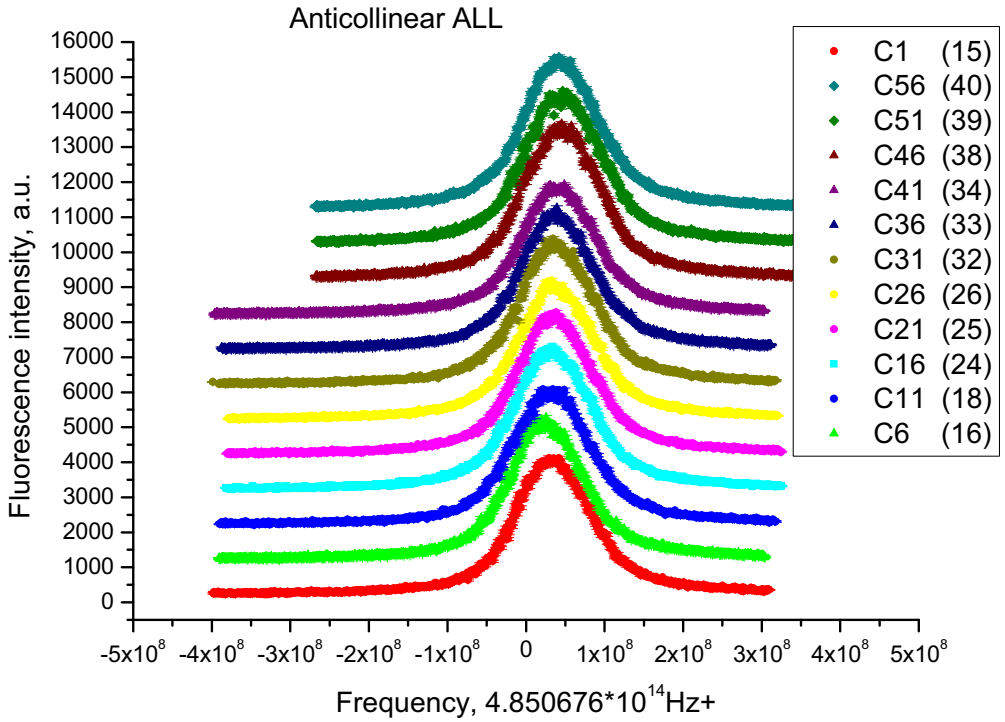

FIG. 67. Operating anode voltage in constant voltage mode. Anticollinear geometry scan.

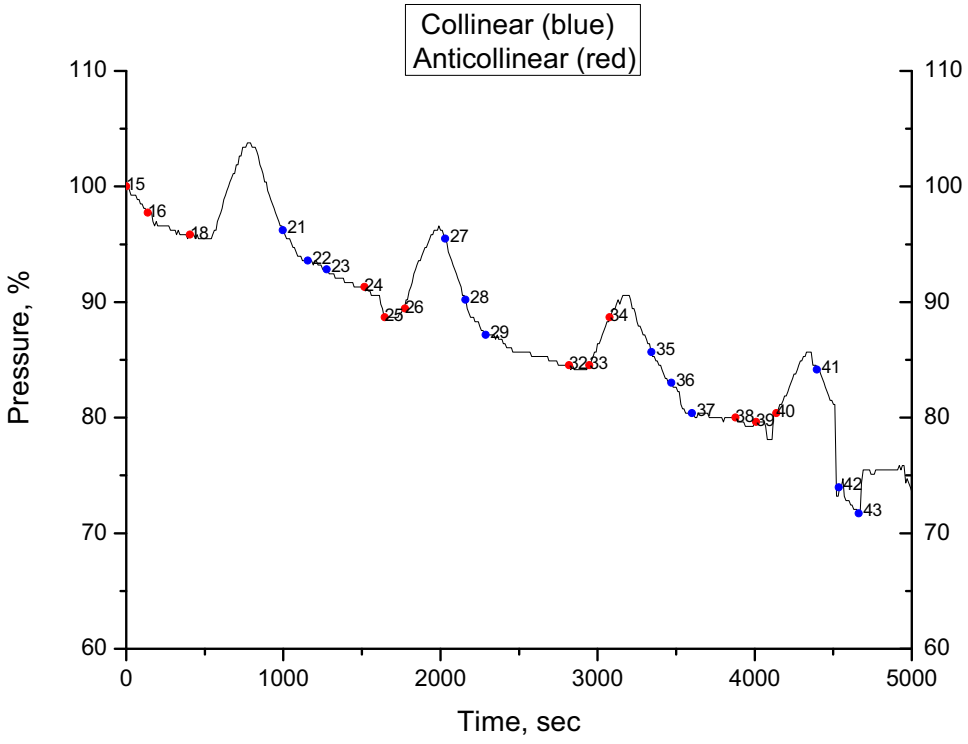

FIG. 68. Pressure drift in the ion source.100% pressure corresponds to the pressure at the beginning of the experiment.

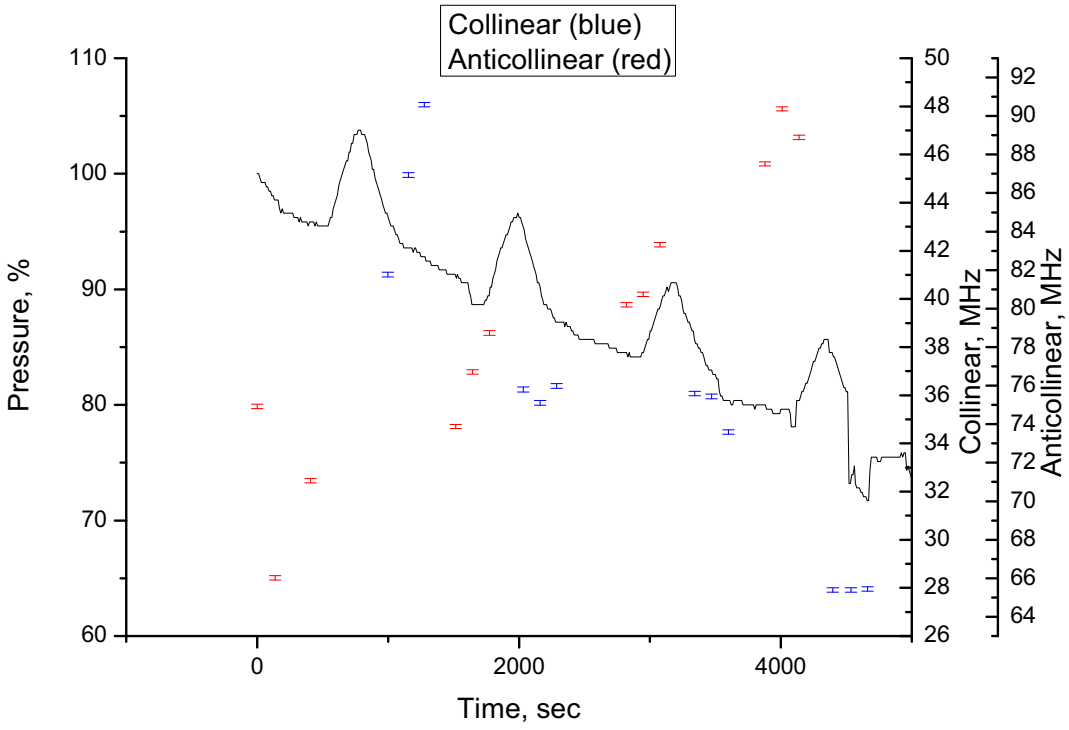

FIG. 69. Pressure drift in the ion source and the corresponding change in the peak of the resonance in collinear (blue) and anticollinear (red) geometries.

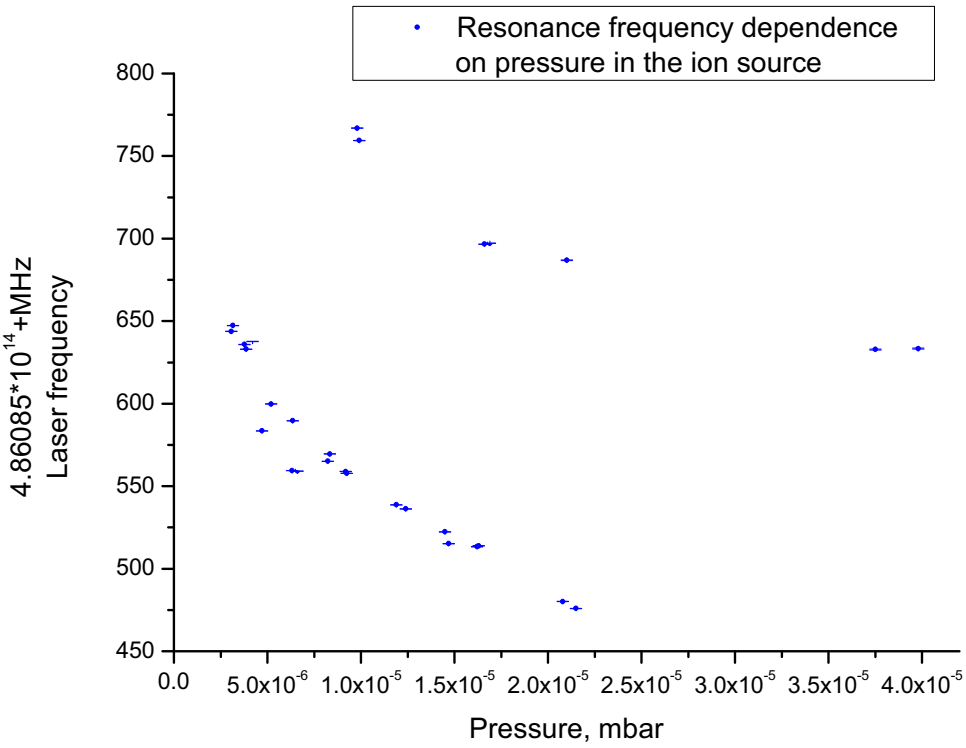

FIG. 70. The frequency of the collinear resonance as a function of the pressure in the ion source.

collected as a function of pressure inside of the ion source (Fig. 70). They indicated that the frequency can shift about 200MHZ depending on the pressure inside of the ion source. Since there was limited control over the pressure fluctuation via needle valve, the only possibility to reduce the influence of the pressure fluctuations was to simultaneously measure collinear and anticollinear frequency. That would reduce the fluctuations of the velocity of the ions in the ion beam.

TABLE XII. Ar II $^2G_{7/2}$-$^2F^o_{5/2}$ transition frequency.

Source	**Transition last three digits, MHz**	**Uncertainty, MHz**
NIST	630	±34
Our results	619.7	± 0.3

5. Main results and discussion on the systematic error

The main results were obtained with almost simultaneous measurements of collinear and anticollinear geometry to reduce the influence of ion source and acceleration voltage instabilities. The data for collinear and anticollinear resonance line shape were fitted with Voigt profile. From the fitting procedure the peaks of the resonance were obtained from collinear and anticollinear measurements and combined according to formula 2.16 to result in transition frequency. The error bar was adjusted to 300kHz (that would constitute the statistical error) such a way to make the reduced χ^2 parameter close to 1 during the transition frequency fitting procedure with the *constant* model over the data of six independent measurements with different kinetic energies of the ion beam and different ion source condition. The calculations of the kinetic energy of the beam and its uncertainty are performed in Appendix D. The data showed good agreement in ν_0 (Fig 71). The resultant transition frequency ν_0 is:

$$\boxed{\nu_0 = 485,573,619.7 \pm 0.3\text{MHz}} \tag{4.17}$$

For comparison NIST [26] value gives for transition$^2G_{7/2}$-$^2F^o_{5/2}$ (last three digit in MHz) 630 ± 34MHZ. The result is compiled in Table XII. For an accurate data analysis, a detailed understanding of systematic effects is necessary. Although they

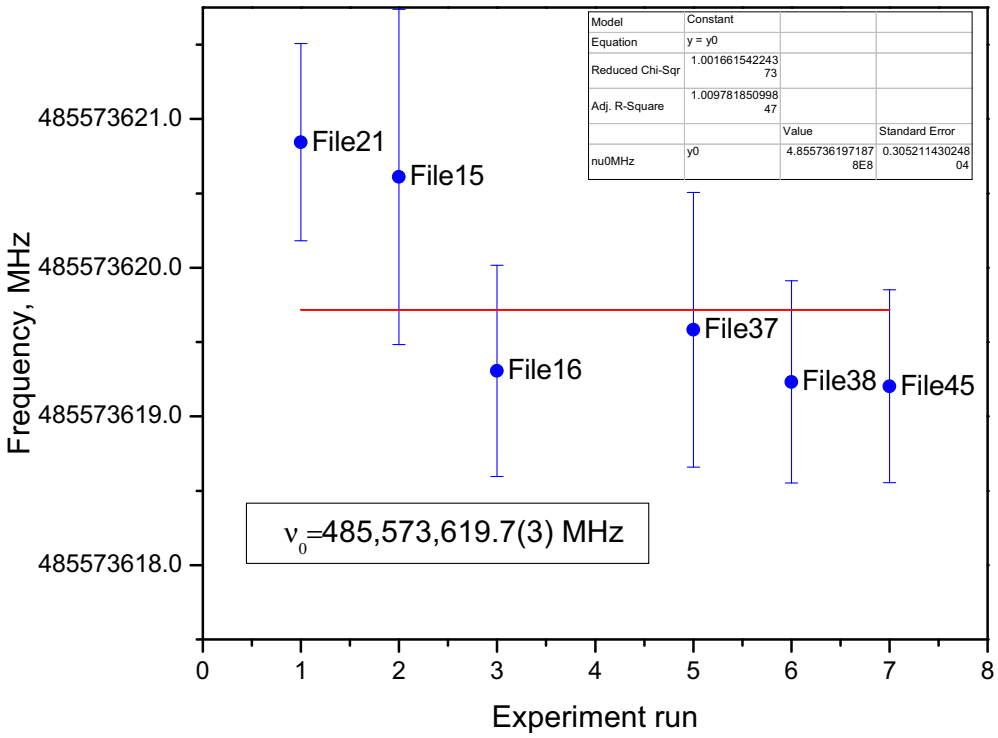

FIG. 71. The transition frequency of Ar II $^2G_{7/2}$-$^2F^o_{5/2}$, Voigt fit.

are significantly reduced with improved spectroscopy techniques described above, they still broaden the absorption line profile and shift the center frequency. In particular, the systematic error of our measurements could be attributed to the divergence of the ion and laser collinear and anticollinear beam, to the residual gas collisions, as well as to the laser frequency measurements with a frequency comb when the data are converted from laser frequency scanning voltage domain to the laser frequency domain. The previous results of other research group [68, 11] show that the uncertainty with the laser frequency measurements could contribute about 3∼5MHz to the uncertainty. In our case this contribution is only 56kHz, which was obtained as following:

$$\delta = \frac{rep.rate + 980MHz}{4}\sqrt{(\delta V_0)^2 + (\delta d)^2} = \tag{4.18}$$

$$= \frac{20MHz + 980MHz}{4}\sqrt{(1.3 \times 10^{-4})^2 + (1.8 \times 10^{-4})^2} \approx 56\text{kHz} \tag{4.19}$$

Several research groups encountered with asymmetry of the line shape due to the residual gas collision [59, 11] or due to inhomogeneous electric field in the fluorescence region [69]. We have tested all our 6 different measurements with symmetric Lorentzian and the result in Fig. 72 let us conclude that we do not have much contribution from asymmetric broadening attributed to collisions with residual gas or homogeneous electric field in the fluorescence region. Thus the main contribution to systematic error seems to be the divergence of the beam. The calculations shows that:

$$\nu_c = \nu_0 \frac{1 + \cos\theta_c}{\gamma}, \tag{4.20}$$

$$\nu_a = \nu_0 \frac{1 - \cos\theta_a}{\gamma}. \tag{4.21}$$

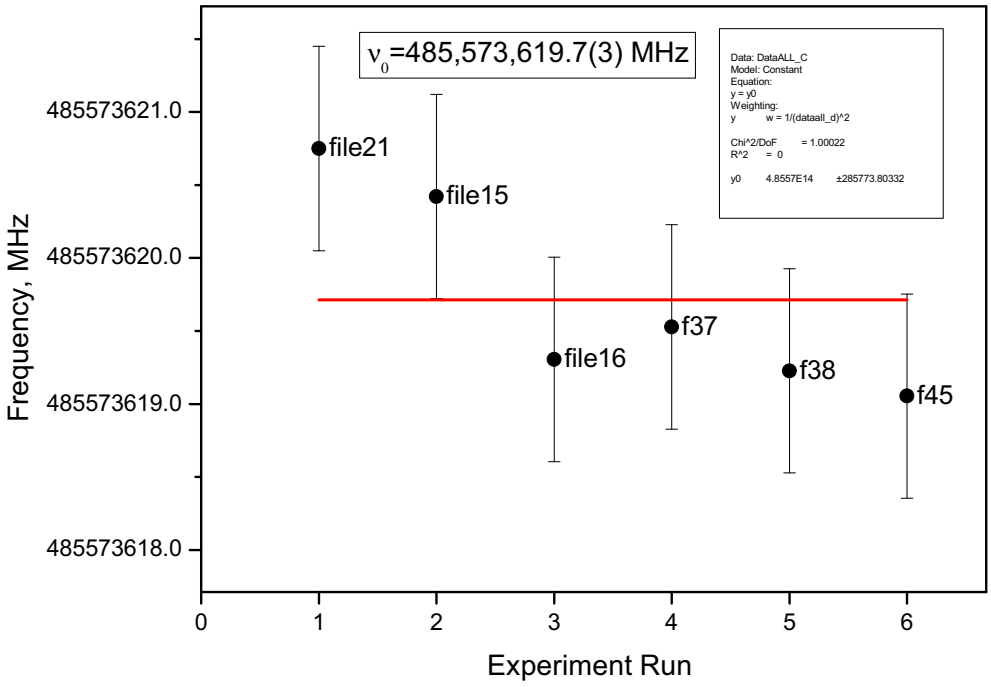

FIG. 72. The transition frequency of Ar II $^2G_{7/2}$-$^2F^o_{5/2}$, Lorentz fit.

$$\nu_c \cdot \nu_a = \nu_0^2 \frac{1 + \beta(\cos\theta_c - \cos\theta_a) - \beta^2 \cdot \cos\theta_c \cos\theta_a}{1 - \beta^2} = \tag{4.22}$$

$$= \nu_0^2 \left(1 + \frac{\beta(\cos\theta_c - \cos\theta_a) + \beta^2(1 - \cos\theta_c \cdot \cos\theta_a)}{1 - \beta^2}\right); \tag{4.23}$$

$$\sqrt{\nu_c \cdot \nu_a} \approx \nu_0 \left(1 + \frac{1}{2}\epsilon\right), \tag{4.24}$$

with $\theta_c = 10 \times 10^{-3}$rad which comes from the ion beam divergence 10mrad and $\theta_a = 10 \times 10^{-3} + 1 \times 10^{-3}$rad as the difference between collinear and anticollinear laser beams are less than 1mrad, we obtain:

$$\delta \approx 2.6\text{MHz}, \tag{4.25}$$

which is about within the margin of our data points with their uncertainties (Fig. 71 and Fig. 72). The other groups have reported [70, 11] δ due to divergence of the beam is:

$$\delta \approx \frac{\nu_0 \beta \theta^2}{8} \tag{4.26}$$

in this case our broadening would give $\delta \approx 6.3$MHz, which is still 5 times less uncertainty than previous data [71].

CHAPTER V

SUMMARY

This dissertation describes the precise absolute measurements of the frequency transition with a frequency comb. The collinear fast beam laser spectroscopy method was employed to measure the frequency transition between the ArII metastable state $^2G_{7/2}$ and the excited $^2F^o_{5/2}$ state. An ion beam apparatus, consisting of an Danfysik 911A ion source, an extractor, an Einzel lens, a dipole magnet, quadrupole quartet and quadrupole triplet was constructed and tested at RIKEN, Japan. Reduced Doppler width of around 100MHz were reached. The experimental data were evaluated with Voigt fitting function. The obtained accuracy of the frequency transition was two orders of magnitude higher then previous results. The various contributions for systematic error were discussed.

REFERENCES

[1] S. L. Kaufmann, Opt. Commun. **17**, 309 (1976).

[2] J. C. Berengut *et al.*, arXiv:physics/0408017 **3**, 8 Mar (2006).

[3] M. T. Murphy *et al.*, Mon. Not. R. Astron. Soc. **380**, 839 (2007).

[4] M. Aldenius, S. Johansson, and M. T. Murphy, Mon. Not. R. Astron. Soc. **370**, 444 (2006).

[5] M. Aldenius and S. Johansson, arXiv:astro-ph/0703145 **1**, 7 Mar (2007).

[6] I. M. Savukov and V. A. Dzuba, Phys. Rev. A **77**, 042501 (2008).

[7] C. Araujo-Hauck *et al.*, The Messenger **129**, 24 (2007).

[8] Ch. H. Li *et al.*, Nature **452**, 610 (2008).

[9] S. Reinhardt *et al.*, Nature **3**, 861 (2007).

[10] O. Poulsen, Nucl. Instrum. Methods Phys. Res. **202**, 503 (1982).

[11] S. Götte *et al.*, Rev. Sci. Instrum. **75**, 1039 (2004).

[12] M. Wada *et al.*, RIKEN Accel. Prog. Rep. **38**, 168 (2005).

[13] E. W. Otten, in *Treatise on Heavy-Ion Science*, edited by D. Bromley (Plenum press, New York and London, 1989), Vol. 8.

[14] H. J. Kluge and W. Nörtershäuser, Spectrochim. Acta, Part B **58**, 1031 (2003).

[15] P. Bricault *et al.*, Rev. Sci. Instrum. **79**, 2 (2008).

[16] M. Wada *et al.*, Hyperfine Interact. **173**, 163 (2006).

[17] J. Lassen, Ph.D. thesis, Texas A&M, 2000.

[18] X. Li, J. Lassen, and H. A. Schuessler, edited by J. W. Wilkerson (SPIE, Methods for Ultrasensitive Detection II, 2002), Vol. 4634, p. 23.

[19] J. Jin and D. A. Church, Phys. Rev. A **47**, 132 (1993).

[20] I. V. Savelyev, *Mechanics and Electrodynamics* (Nauka, Moscow, 1991).

[21] J.D. Jackson, *Classical Electrodynamic* (Mir, Moscow, 1965).

[22] G. Borghs *et al.*, Opt. Commun. **38**, 101 (1981).

[23] *The Physics and Technology of Ion Sources*, edited by I. Brown (WILEY-VCH, Weinheim, 2004).

[24] A. N. Matveev, *Molecular Physics* (Mir, Moscow, 1985).

[25] W. Demtröder, *Atoms, Molecules and Photons* (Springer, Berlin, Heidelberg, New York, 2006).

[26] Yu. Ralchenko *et al.*, http://physics.nist.gov (2008).

[27] R. Kirchner, Nucl. Instrum. and Methods **186**, 275 (1981).

[28] O. Svelto, *Principles of Lasers* (Plenum press, New York, 1998).

[29] *High-Resolution Laser Spectroscopy*, Vol. 13 of *Topics in Applied Physics*, edited by K. Shimoda (Springer-Verlag, Berlin, Heidelberg, New York, 1976).

[30] I.S. Osad'ko, *Selective Spectroscopy of Single Molecules* (Springer, Berlin, New York, 2003).

[31] W. Demtröder, *Laser Spectroscopy* (Springer, Berlin, Heidelberg, 2003).

[32] J. H. Freeman and G. Sidenius, Nucl. Instrum. and Methods **107**, 477 (1972).

[33] G. Sidenius, Nucl. Instrum. and Methods **38**, 19 (1965).

[34] *The Danfysik Ion Source Model 911A*, Danfysik Jyllinge-Denmark, 1973.

[35] *Handbook of Ion Sources*, edited by B. Wolf (CRC press, Boca Raton, New York, London, Tokyo, 1995).

[36] A. Pyszniak *et al.*, Instrum. and Exp. Tech. **50**, 552 (2007).

[37] M. Turek, A. Drozdziel, K. Pyszniak, and J. Sielanko, Vacuum **78**, 649 (2005).

[38] P. Grivet, *Electron Optics* (Pergamon press, Oxford, London, Edinburgh, New York, Paris, Frankfurt, 1965).

[39] A. Adams and F.H. Read, J. Phys. E **5**, 150 (1972).

[40] *Focusing of Charged Particles*, edited by A. Septier (Academic press, Orlando, San Diego, San Francisco, New York, London, Toronto, Montreal, Sydney, Tokyo, San Paulo, 1967), Vol. 1.

[41] H. Wollnik, B. Hartmann, and M. Berz, in *Principles of GIOS and COSY*, edited by C. Eminhizer (AIP, Conf. Proc., 1988), Vol. 177, p. 74.

[42] P.W. Hawkes, in *Quadrupoles in Electron Lens Design*, Vol. 7 of *Advances in Electronics and Electron Physics*, edited by L. Marton (Academic press, New York, London, 1970).

[43] *Model 2000 Multimeter*, Keithley instruments, 2003.

[44] M. Drosg, *Dealing with Uncertainties* (Springer, Berlin, Heidelberg, New York, 2007).

[45] H. Wollnik, *Optics of Charged Particles* (Academic press, Orlando, San Diego, New York, Austin, Boston, London, Sydney, Tokyo, Toronto, 1987).

[46] J. J. Livingood, *The Optics of Dipole Magnets* (Academic press, New York, London, 1969).

[47] L. D. Landau and E. M. Lifshitz, *The Classical Theory of Fields* (Nauka, Moscow, 1988).

[48] S. Humphries, *Charged Particle Beams* (Wiley, New York, 1990).

[49] I. R. Kenyon, *The Light Fantastic* (Oxford University press, New York, 2008).

[50] W. J. Smith, *Modern Optical Engineering* (McGraw Hill, New York, 2008).

[51] N. P. Zakaznov, S. I. Kiryushin, and V. N. Kuzichev, *Theory of Optical Systems* (Mashinostroenie, Moscow, 1992).

[52] A. Gerrard, *Introduction to Matrix Methods in Optics* (Mir, Moscow, 1978).

[53] A. N. Matveev, *Optics* (Vysshaya Shkola, Moscow, 1985).

[54] A. Takamine, Ph.D. thesis, Tokyo, 2007.

[55] H. Kato *et al.*, *Doppler-Free High Resolution Spectral Atlas of Iodine Molecule 15,000 to 19,000 cm^{-1}* (Japan society for the promotion of science, Tokyo, 2000).

[56] F. Zhu, Master's thesis, Texas A&M, 2005.

[57] *FC1500 Optical Synthesizer*, MenloSystem, GmbH, 2007.

[58] W. Becker, *Advanced Time-Correlated Single Photon Counting Techniques* (Springer-Verlag, Berlin, Heidelberg, 2005).

[59] J. Zhang, Ph.D. thesis, Texas A&M, 1986.

[60] W. Hofer, W. Vanek, P. Varga, and H. Winter, Rev. Sci. Instrum. **54**, 150 (1983).

[61] R. L. Kelly, *Atomic and Ionic Spectrum Lines below 2000 Angstroms. Hydrogen through Krypton* (American Insitute of Physics (AIP), American Chemical Society and the National Bureau of Standards, New York, 1987).

[62] P. Schef *et al.*, Eur. Phys. J. D **29**, 195 (2004).

[63] B. K. McMillin and M. R. Zachariah, J. Appl. Phys. **77**, 5538 (1995).

[64] G. D. Severn, D. A. Edrich, and R. McWilliams, Rev. Sci. Instrum. **69**, 10 (1998).

[65] S. Haroche and F. Hartmann, Phys. Rev. A **6**, 1280 (1972).

[66] J. H. Shirley, Phys. Rev. A **8**, 347 (1973).

[67] V. Ryjkov, Ph.D. thesis, Texas A&M, 2003.

[68] E. Riis, H. G. Berry, and O. Poulsen, Phys. Rev. A **33**, 3023 (1986).

[69] R. T. Short *et al.*, Phys. Rev. A **39**, 3969 (1973).

[70] R. Neugart, in *Progress in Atomic Spectroscopy*, edited by H. J. Beyer and H. Kleinpoppen (Plenum press, New York, 1987), Vol. D.

[71] G. Norlen, Physica Scripta **8**, 249 (1973).

[72] J.R. Taylor, *An Introduction to Error Analysis* (University Science Books, Mill Valley, California, 1982).

APPENDIX A

EXAMPLE OF *LABVIEW* PROGRAM TO CONTROL THE ACCELERATION VOLTAGE FEEDBACK LOOP

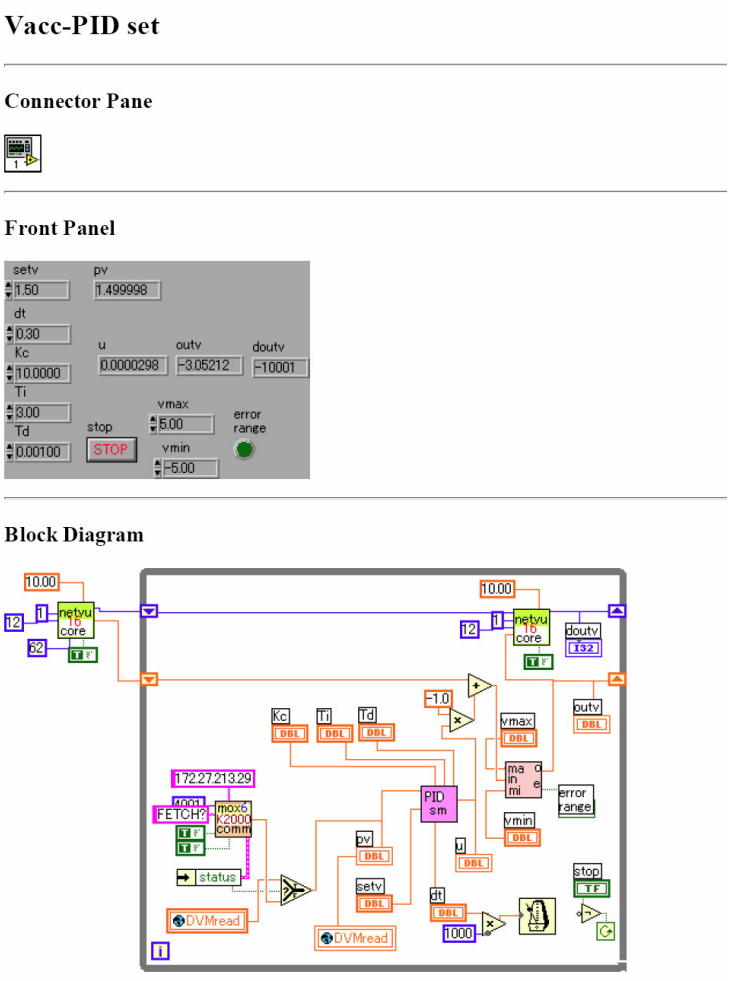

FIG. 73. *Labview* code for acceleration voltage PID set.

sPID

Connector Pane

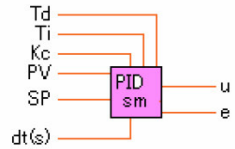

Front Panel

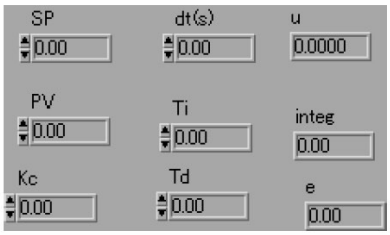

Block Diagram

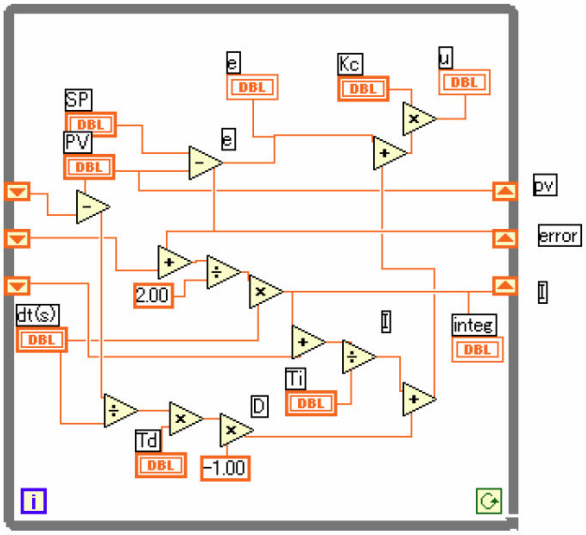

FIG. 74. *Labview* code for sPID.

APPENDIX B

C++ CODE FOR CALCULATION THE TRANSITION PROBABILITY FOR THE EXCITED STATE $^{40}AR^{+}$ LINE 617.3986NM

The probability that the atom will be in excited state can be found solving equations for absorption and emission coefficients using Laplace transform. For the resonance case one would have:

$$G_0(t) = -i \exp^{-ibt} \left(\cos Rt - i \frac{b}{R} \sin Rt \right), \tag{B.1}$$

and

$$G_1(t) = \exp^{-ibt} \frac{\Lambda}{R} \sin Rt, \tag{B.2}$$

where

$$b = -i\frac{\gamma}{4}, \; R = \sqrt{|\Lambda|^2 - \frac{\gamma^2}{16}}. \tag{B.3}$$

The solution greatly depends on the intensity of laser radiation and can be subdivided in two major cases: when $I < I_c$ which corresponds to weak pumping and $I > I_c$ which corresponds to strong pumping, where

$$I_c = \frac{\pi}{12} \frac{\gamma}{\lambda^2}. \tag{B.4}$$

For our case λ=617.3986nm,

$$\gamma = \frac{1}{\tau} = A_{ik} = 2 \times 10^7; \tag{B.5}$$

I=0.43mW, then:

$$I_c = \frac{\pi}{12} \cdot \frac{2 \times 10^7}{(617.3986)^2 \times 10^{-18}} = 1.37362 \times 10^{19} \frac{\text{photons}}{\text{m}^2 \cdot \text{sec}}, \tag{B.6}$$

$$I_c = 1.37362 \times 10^{15} \frac{\text{photons}}{\text{cm}^2 \cdot \text{sec}}, \tag{B.7}$$

$$I_c = 1.37362 \times 10^{15} \cdot \frac{hc}{\lambda} \cdot \frac{1}{\text{cm}^2} = 0.442189 \frac{\text{mW}}{\text{cm}^2}; \tag{B.8}$$

$$I_{\text{input}} = \frac{0.43mW}{\pi \cdot \frac{0.5^2}{4}} = 2.1 \frac{\text{mW}}{\text{cm}^2}; \tag{B.9}$$

$$\boxed{I_{\text{input}} > I_c.} \tag{B.10}$$

$$N(t) = e^{-\frac{\gamma t}{2}} \cdot \frac{|\Lambda|^2}{R^2} \sin^2 Rt; \tag{B.11}$$

$$\Lambda = |\lambda_0|\sqrt{n} \Rightarrow |\lambda_0| = \frac{\gamma}{4} \cdot \frac{1}{\sqrt{n_c}} = \frac{2 \times 10^7}{\sqrt{1.37362 \times 10^{19}}} = 0.00134908. \tag{B.12}$$

$$|\Lambda|^2 = |\lambda_0|^2 \cdot n = \frac{\gamma^2}{16} \cdot \frac{n}{n_c}; \tag{B.13}$$

$$R = \sqrt{|\Lambda|^2 - \frac{\gamma^2}{16}} = \sqrt{\frac{\gamma^2}{16}\left(\frac{n}{n_c} - 1\right)} = \tag{B.14}$$

$$= \frac{\gamma}{4}\sqrt{\frac{n}{n_c} - 1}; \tag{B.15}$$

$$\frac{|\Lambda|^2}{R^2} = \frac{n}{n_c} \frac{1}{\left(\sqrt{\frac{n}{n_c} - 1}\right)^2} = \frac{n}{n_c} \cdot \frac{1}{\left(\frac{n}{n_c} - 1\right)} = \tag{B.16}$$

$$= \frac{n}{n - n_c} = \frac{1}{1 - \frac{n_c}{n}}; \tag{B.17}$$

$$\boxed{N(t) = e^{-\frac{\gamma t}{2}} \cdot \frac{1}{1 - \frac{I_c}{I}} \cdot \sin^2\left(\frac{\gamma}{4} \cdot \sqrt{\frac{I}{I_c} - 1} \cdot t\right).} \tag{B.18}$$

```
# include <iostream.h>

# include <math.h>

# include <iomanip.h>

double I_0=40E-6; // I_0 -initial intensity, milliwatt

double I_S=1.8; //saturation intensity, milliwatt

double tau=0; // relaxation time
```

```
double A21=2E7; // Einstein coefficient for spontenious radiation
double lyambda=611.6616E-9; // wavelength of radiation
double t=0;
const double  c=299792458;
const double  h=6.625E-34;
const double Pi=3.14;
main (){
for (int i=0; i<=700; i++){
cout<<t<<"   "<<((exp(-A21*t/2))*1/(1-I_S/I_0)*
sin(A21/4*sqrt(I_0/I_S-1)*t)*
sin(A21/4*sqrt(I_0/I_S-1)*t))<<endl;
t=t+0.000000001;}
return 0;}
```

APPENDIX C

C++ CODE FOR CALCULATION CONDENSOR LENS SYSTEM

The optical system of the lenses is characterized by the transition matrix of optical system S_{21} with gaussian parameters a, b, c, d.

$$S_{21} = \begin{pmatrix} b & -a \\ -d & c \end{pmatrix}, \tag{C.1}$$

where

$$\begin{aligned} a &= k_1 + k_2 - k_1 k_2 \Delta_1'/n_1'; \quad & b &= 1 - k_2 \Delta_1'/n_1'; \\ c &= 1 - k_1 \Delta_1'/n_1'; & d &= -\Delta_1'/n_1', \end{aligned} \tag{C.2}$$

and

$$\det S_{21} = bc - ad = 1. \tag{C.3}$$

Knowing the transition matrix of the system, we always can compute cardinal elements of the optical system, which are shown in Fig. 76, as following:

$$\ell_H = n_1(1-b)/a; \tag{C.4}$$

$$\ell_H' = n_2'(c-1)/a; \tag{C.5}$$

$$c - a\ell_F'/n_2' = 0; \tag{C.6}$$

$$\ell_F' = n_2' c/a; \tag{C.7}$$

$$f' = \ell_F' - \ell_H' = n_2'/a; \tag{C.8}$$

$$\ell_F = -n_1 b/a; \tag{C.9}$$

$$f = \ell_F - \ell_H = -n_1/a. \tag{C.10}$$

TABLE XIII. Condesor lens system parameters.

Parameter	**Value**
	mm
ℓ_H	15.454102
ℓ'_H	-15.454102
ℓ_F	-20.599604
ℓ'_F	20.599604
F'	36.053706
F	-36.053706

The lens equation can be given in Newton's form (Fig. 75):

$$zz' = ff', \tag{C.11}$$

or in Gauss's form:

$$\frac{f'}{s'} + \frac{f}{s} = 1 \tag{C.12}$$

The result of the calculation is summarized in Table XIII.

```
# include <iostream.h>
# include <math.h>
# include <iomanip.h>
double d=10.0; // distance between lenses
    /* matrix A*/
double a11=0.849347; //      b
double a12=-0.014992; //      -a
double a21=10.048963; //      -d
```

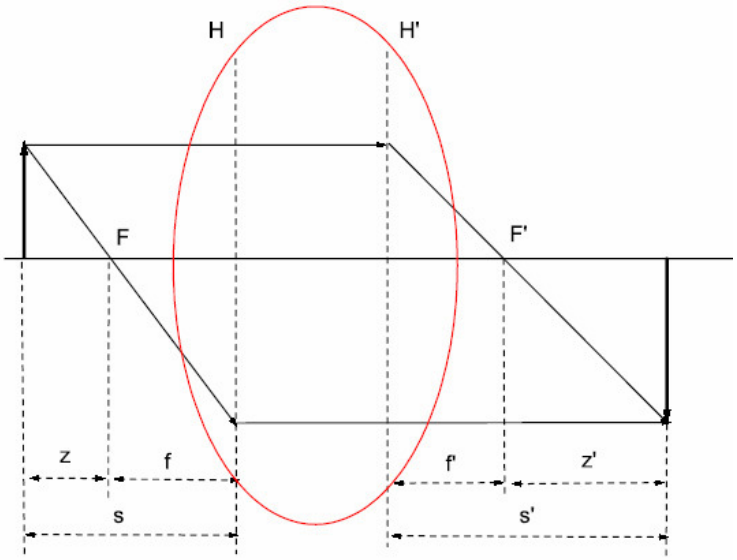

FIG. 75. Object and image of a thick lens.

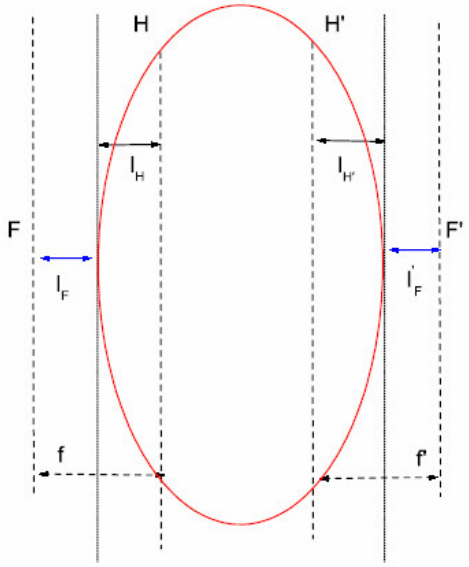

FIG. 76. Definition of the principal axes of the a lens.

```
double a22=1; //      c
      /*matrix B*/
double b11=1; //       b
double b12=-0.014992; //       -a
double b21=10.048963; //       -d
double b22=0.849347; //       c
        /*matrix T*/
double t11=1; //
double t12=0; //
double t21=d; //
double t22=1; //
    /*matrix C*/
double c11=0; //
double c12=0; //
double c21=0; //
double c22=0; //
double a,b,c,dd; // gaussian parameters
double f_prime=0; // focal distance of the lense [mm]
double n_1_prime=1.48274; //  refractive index of the lense
double n_2=1.48274;
double n_1=1;
double n_2_prime=1;
double Gaussian_determinant(void);
double l_H(void);
double l_H_prime(void);
double l_F(void);
```

```
double l_F_prime(void);
main ()
{
char ch;
for (int i=1; i<=2; i++)
{
c11=b11*a11+b12*(d*a11+a21);
c12=b11*a12+b12*(d*a12+a22);
c21=a11*b21+b22*(d*a11+a21);
c22=a12*b21+b22*(d*a12+a22);
b=c11;
a=-c12;
dd=-c21;
c=c22;
cout<< setprecision(6)<< setiosflags(ios::fixed | ios::showpoint)
    <<"det"<<setw(20)<<Gaussian_determinant()<<endl;
cout<< setprecision(6)<< setiosflags(ios::fixed | ios::showpoint)
    <<"d"<<setw(20)<<d<<endl;
cout<< setprecision(6)<< setiosflags(ios::fixed | ios::showpoint)
    <<"l_H"<<setw(20)<<l_H()<<endl;
cout<< setprecision(6)<< setiosflags(ios::fixed | ios::showpoint)
    <<"l_H_prime"<<setw(20)<<l_H_prime()<<endl;
cout<< setprecision(6)<< setiosflags(ios::fixed | ios::showpoint)
    <<"l_F"<<setw(20)<<l_F()<<endl;
cout<< setprecision(6)<< setiosflags(ios::fixed | ios::showpoint)
    <<"l_F_prime"<<setw(20)<<l_F_prime()<<endl;
```

```
cout<< setprecision(6)<< setiosflags(ios::fixed | ios::showpoint)
<<"F_prime"<<setw(20)<<(l_F_prime()-l_H_prime())
<<setw(20)<<(n_2_prime/a)<<endl;
cout<< setprecision(6)<< setiosflags(ios::fixed | ios::showpoint)
    <<"F"<<setw(20)<<(l_F()-l_H())<<setw(20)<<(-n_1/a)<<endl;
}
cin>> ch;
return 0;
}
double Gaussian_determinant(void)
{return b*c-a*dd;}
double l_H(void)
{return n_1*(1-b)/a;}
double l_H_prime(void)
{return n_2_prime*(c-1)/a;}
double l_F(void)
{return -n_1*b/a;}
double l_F_prime(void)
{return  n_2_prime*c/a;}
```

APPENDIX D

ACCELERATION VOLTAGE CALCULATIONS

The acceleration voltage can be determined through the measurements of collinear and anticollinear laser frequencies [11] as following:

$$\boxed{V = -\frac{mc^2}{2q}\left(\sqrt{\frac{\nu_c}{\nu_a}} + \sqrt{\frac{\nu_a}{\nu_c}} - 2\right),} \tag{D.1}$$

where m is a mass of the ion, in our case of single charged ion $m = m_0 - m_e$, with m_0 mass of the atom, m_e mass of the electron, $q = e$ charge of electron, c speed of light, ν_c collinear and ν_a anticollinear laser frequencies respectively. The propagation of error can be found as following [72]:

$$f(x_1, x_2) = A\left(\sqrt{\frac{x_1}{x_2}} + \sqrt{\frac{x_2}{x_1}} - 2\right); \tag{D.2}$$

$$\frac{\partial f(x_1, x_2)}{\partial x_1} = A\left(\frac{1}{\sqrt{x_2}} \cdot \frac{1}{2\sqrt{x_1}} + \sqrt{x_2} \cdot (-\frac{1}{2}) \cdot x_1^{-3/2}\right) = \tag{D.3}$$

$$= \frac{A}{2}\left(\frac{1}{\sqrt{x_1 x_2}} - \frac{\sqrt{x_2}}{\sqrt{x_1^3}}\right); \tag{D.4}$$

$$\frac{\partial f(x_1, x_2)}{\partial x_2} = A\left(-\frac{\sqrt{x_1}}{\sqrt{x_2^3}} + \frac{1}{\sqrt{x_1 x_2}}\right); \tag{D.5}$$

$$\boxed{\delta V = \sqrt{\left(\frac{\partial f(x_1, x_2)}{\partial x_1}\delta x_1\right)^2 + \left(\frac{\partial f(x_1, x_2)}{\partial x_2}\delta x_2\right)^2}.} \tag{D.6}$$

Applying formula D.6 to our collinear and anticollinear data fitted with Voigt model, we obtained the acceleration voltage for each run. The results are complied in Table XIV.

TABLE XIV. Determination of the different acceleration voltages used. The acceleration is the sum of high voltage applied to the ion source and the postacceleration voltage.

File number	**Acceleration voltage**	**Uncertainty**
	V	V
21	20198.077	0.028
15	20198.879	0.047
16	20198.345	0.030
37	20216.377	0.038
38	20216.010	0.028
45	20215.839	0.027

VITA

Vladimir Lioubimov was born in Chelyabinsk, Russia. He received the degree of Engineer-Physicist with Honor (Red Diploma) from Moscow State Engineering and Physics Institute, Moscow, Russia. He received his M.S. degree in physics from Texas A&M University in 2002 and his Ph.D. degree in physics from Texas A&M University in 2008. For his address and other current information please contact Prof. Hans A. Schuessler, Department of Physics, Texas A&M University, College Station, TX 77843-4242.

The typist for this dissertation was Vladimir Lioubimov.